DEVELOPMENT OF DYNAMIC SUBSTRATES FOR STUDIES OF CELL ADHESION AND MIGRATION

Eun-ju Lee

A dissertation submitted to the faculty of the University of North Carolina at Chapel Hill in partial fulfillment of the requirements for the degree of Doctor of Philosophy in the Department of Chemistry.

Chapel Hill
2009

Approved by

Muhammad Yousaf

Linda Spremulli

Mark Wightman

Joseph DeSimone

Matthew Redinbo

ABSTRACT

Eun-ju Lee

Development of Dynamic Substrates for Studies of Cell Adhesion and Migration

(Under the direction of Muhammad Yousaf)

A class of model substrates that modulate the dynamic environment for a variety of cell adhesion and migration experiments was developed. The substrate is based on an electrochemically switchable self-assembled monolayer that presents redox active hydroquinone groups. In the presence of the cells, the surface can be activated to undergo chemoselective reaction between quinone monolayers and oxyamine-tethered ligands resulting in ligand immobilization on the surface. The dynamic substrates were used to probe in real-time how the interplay between the population of cells, the initial pattern geometry, ligand density, ligand affinity and integrin composition affects cell migration and growth. The study also showed cell migration was affected by initial events which dictated subsequent motility that superseded the composition of the underlying surface chemistry. Whole genome microarray analysis indicates that several classes of genes ranging from signal transduction to cytoskeletal reorganization are differentially regulated depending on the nature of the surface conditions.

A combined photochemical and electrochemical approach generated model substrates presenting molecularly defined gradients of ligands for studying cell migration and

polarization. Deprotection of a photo-labile group by ultraviolet light revealed redox active molecules in patterns and gradients; consequently so were the coupled ligand molecules. We show quantitatively the subtle interplay between ligand slope, density and affinity that causes a cell to modulate its adhesion and migration position and behavior during directed movement. The methodology for immobilizing ligand and patterning gradient was also used in producing co-culture model substrate and nanoarrays for adhesion study.

ACKNOWLEDGEMENT

I would like to thank my advisor Muhammad Yousaf for guiding me through the Ph.D. course. His support and encouragement let me explore diverse areas of science. I also would like to thank my committee members.

I am grateful to my group members both past and present. I will never forget the earliest time in our group with Dr. Eugene Chan and Wei Luo. I can find their devotion and efforts in initiating the actual research in every corner in the lab and I appreciate the challenging but rewarding time with them. All members have greatly contributed to the shape of our group and I am very thankful.

I have been very lucky to share many moments with my friends in Chapel Hill. I cherish the sharing of our science and thoughts with Ralph and all other members of the literature study groups. Junghoon and Jiwhan always showed me what true friendship is. Mizumi and Sungjin always took good care of me as if they are my “sempai”. I was very fortunate to meet Candida and she has inspired me in so many ways and let me mature as a person. I always feel loved by such good people and they made my life in Chapel Hill even more memorable.

My family in Korea has been the strength of my everyday life and it became even stronger in difficult times. The love and support of my parents really made me be here today and I truly appreciate them showing me how to live a life and how to give love. My sisters and brothers believe in their youngest sister all the time and I just thank and love them very much.

My best friend and partner of life, Michael Heaven, has been the person who I relied on for everything. His existence is so close and it never changes no matter how far we are. He has also been my personal mentor in scientific research and it helped me tremendously throughout my study. I would like to thank his family in Australia as well for making me feel loved all the time.

TABLE OF CONTENTS

List of Tables

List of Figures

CHAPTER 1

Chemical Design and Development of a Model Substrate

Introduction

Self-assembled Monolayers (SAMs)

Self-assembled monolayers (SAMs) are ordered monomolecular films formed by spontaneous organization of molecules (surfactant) on a solid surface [1-7]. The surface on which a SAM forms and the physical object supporting that surface often are referred to as the "substrate". Types of substrates range from planar surfaces (glass or silicon slabs supporting thin films of metal, metal foils, single crystals) to highly curved nanostructures (colloids, nanocrystals, nanorods). The principal driving force for formation of these assemblies is specific interactions between the surfactant head group and the substrate surface. Depending on the structure of the surfactant, SAMs can be disordered (liquid-like) or well-packed, resembling the organization of crystals. The degree of order in monolayers is a product of many factors and includes geometric considerations, electrostatic and dipole-dipole interactions within the monolayers, affinity of the head group of the surfactant to the surface. Monolayers of fatty acids, organosulfur adsorbates on metal, alkyl monolayers on silicon, long-chain organic acids on oxides of metals are all classes of SAMs. The most studied SAMs to date are monolayers of alkanethiolates on gold.

SAMs have been used for controlling physical properties of interfaces, such as wetting, adhesion, lubrication and corrosion, as well as understanding fundamental aspects of interfacial phenomena [1, 2, 8, 9]. SAMs are also widely utilized to generate two-dimensional micro- and nano-structures by immobilizing biomolecules (e.g. nucleic acids, peptides and carbohydrates) and cells in a spatially controlled manner [2, 10-19].

SAMs - Alkanethiolates on Gold

The wide use of gold as a substrate for studying SAMs is due to several advantageous characteristics: 1. gold is exceptionally easy to pattern by a combination of lithographic tools and chemical etchants; 2. gold is a reasonably inert metal thus it does not react with atmospheric oxygen or most chemicals; 3. gold binds thiols with a high affinity and does not undergo any unusual reactions with them; 4. thin films of gold are common substrates used for a number of existing spectroscopies and analytical techniques, and; 5. gold is compatible with cells that can adhere and function on gold surfaces without evidence of toxicity [1-3, 16]. SAMs formed from thiols on gold are stable for periods of days to weeks when in contact with the complex liquid media required for cell studies. The ordering of alkanethiols is driven by the strong affinity between sulfur and gold, the lateral van der Waals interactions between the tethered alkyl chains, and the dipole interactions between polar end groups.

Chemisorption of alkanethiols on gold forms stable SAMs and the interfacial structure can be controlled and tailored using routine organic synthesis [1, 4-6, 20]. The structure of these monolayers is illustrated in Figure 1-1A. The assembly chemistries involve significant contributions from the interplay between the metal-sulfur bonding and stabilizing lateral interactions of the organic groups. The structural model of the SAMs of thiols on the gold

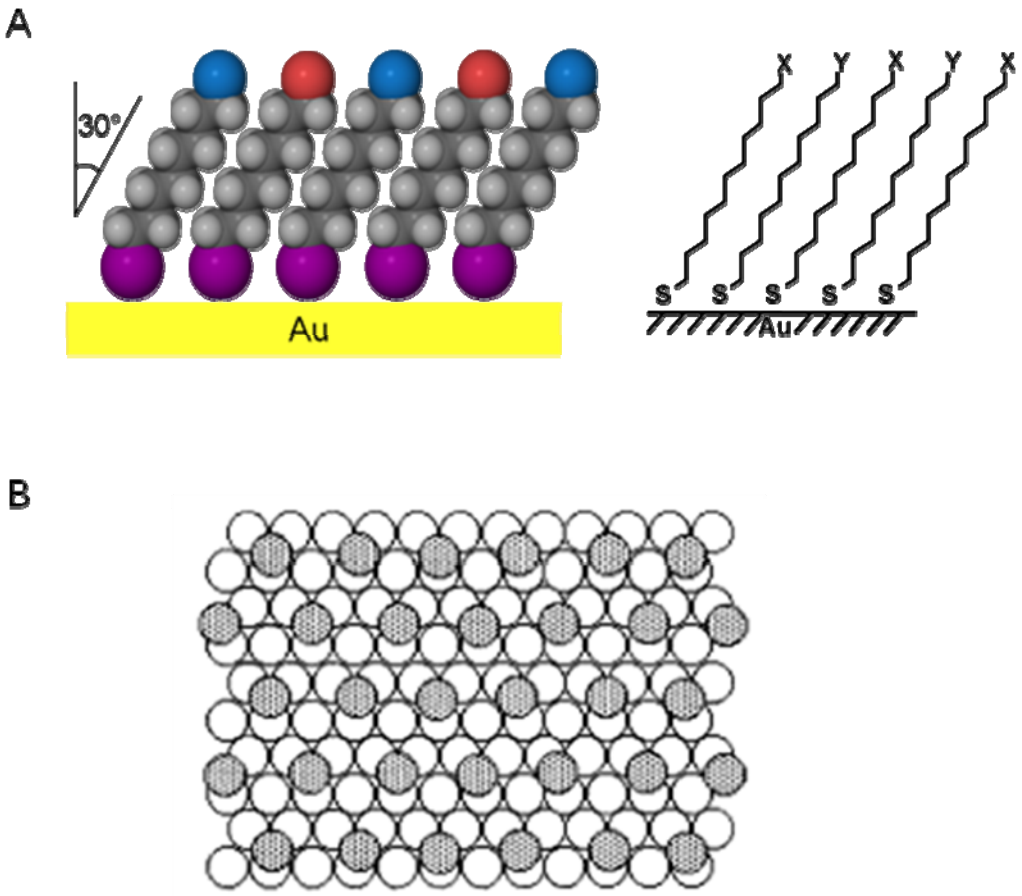

Figure 1-1. Representation of self-assembled monolayer (SAM) of alkanethiolates on the surface of gold. A. (Left) A space-filling model of alkanethiolates chemisorbed to a gold surface. The alkyl chains are close-packed and tilted approximately 30° from the normal to the surface. (Right) Schematic drawing of SAM. The properties of the SAM are determined by the terminal functional group of the precursor alkanethiol. B. Hexagonal coverage scheme for alkanethiolates on Au (111). The open circles are gold atoms and the shaded circles are sulfur atoms. The alkanethiolates coordinate to the hollow three-fold sites of the gold (111) surfaces. The gold atoms are arranged in a hexagonal relationship.

lattice is shown in Figure 1-1B. The arrangement shown is a ($\sqrt{3}$ x $\sqrt{3}$) R 30° structure where the sulfur atoms (dark gray circles) are positioned in the three-fold hollows of the gold lattice (white circles). The geometric arrangement of the sulfur moieties on the surface and the nearest-neighbor distances between the metal atoms at the surface are factors that determine the upper limit on the density of molecules on the surface. For the organic layer, the molecules adopt conformations that allow high degrees of van der Waals interactions with the neighboring molecules to minimize the free energy. These arrangements yield a secondary level of organization in the monolayer that is important in determining macroscopic materials properties, such as wetting, of the SAMs. The electron diffraction studies indicated that the symmetry of sulfur atoms in a monolayer is hexagonal with a spacing between sulfur atoms of 4.97 Å, and calculated area per molecule of 21.4 $Å^2$ [21].

From the kinetic studies, the adsorption of alkanethiol onto gold (111) surfaces was found to strongly depend on alkanethiol concentration [1, 2]. At 1 mM solution of alkanethiol, the monolayer is formed within a few minutes while it takes over 100 minutes at 1 μM concentration [22]. Chemisorption of alkanethiols as well as of di-*n*-alkyl disulfides on clean gold gives indistinguishable monolayers [20, 23].

The strong chemical bonding that is exhibited is best described by Au^+ and RS^-. A simple oxidative addition of the S-S bond to the gold surface is possibly the mechanism in the formation of SAMs from disulfides:

$$RS\text{-}SR + Au(0)_n \rightarrow RS^-Au^+ \cdot Au(0)_{n-1}$$

There is evidence supporting this disulfide bond cleavage mechanism and the subsequent formation of a gold thiolate species. The rates of formation of SAMs from dialkyl disulfides or alkanethiols are indistinguishable, but the rate of replacement of molecules from SAMs by thiols was much faster than by disulfides.

In the alkanethiol case, the reaction may be considered formally as an oxidative addition of the S-H bond to the gold surface, followed by a reductive elimination of the hydrogen:

$$RSH + Au(0)_n \rightarrow RS^{-}Au^{+}\cdot Au(0)_{n-1} + \tfrac{1}{2}\, H_2$$

The combination of hydrogen atoms at the metal surface to yield H_2 molecules may be an important exothermic step in the overall chemisorption energetics. It has been shown that the adsorbing species is the thiolate (RS^{-}) by XPS [6, 24, 25], Fourier transform infrared spectroscopy (FTIR) [25, 26], Fourier transform mass spectrometry [27], electrochemistry [28], and Raman spectroscopy [29]. On the basis of the bond energies of RS-H, H_2 and RS-Au (87, 104 and 40 kcal/mol, respectively), the net energy for adsorption of alkanethiolates on gold would be *ca.* -5 kcal/mol (exothermic) [1]. Nuzzo and co-workers used grazing-angle FTIR to show that the alkyl chains are trans-extended, close-packed and tilted approximately 30° from the normal to the surface [20].

Virtually any functional group can be introduced in the monolayers as a terminal group and consequently determines the properties of the SAMs. This ability to precisely control surface composition makes them an invaluable tool for studying interfacial reactions. Co-adsorption of two or more substituted alkanethiolates leads to formation of a mixed

monolayer, thus enhancing control over surface composition and properties [4, 30]. The densities of mixed SAMs can also be controlled by adjusting the ratio of alkanethiols. For SAMs formed from alkanethiols on gold, the typical surface density of molecules when maximum coverage is obtained is ~4.5 × 10^{14} molecules/cm^2 [2]. Most spectroscopic and experimental evidence suggests that the average properties of SAMs formed from n-alkanethiols (e.g. wettability, mass coverage) do not change significantly when exposed to ~1 mM solutions of alkanethiols for more than 12-18 hours.

Stimuli-responsive SAM Surfaces for Bio-application

Simple small functional groups (-OH, -COOH) are often adequate for studies of properties relevant to materials science such as wettability, friction, adhesion and corrosion resistance. If we consider that these applications are based on the "static" property of SAMs, the introduction of a dynamic property onto the surface is challenging but of great interest. By a method which induces surface reactions only when needed we can generate stimuli-responsive surfaces in which the physical, chemical and biological properties of surfaces are tuned [12, 31-35]. The surfaces that can be changed or tuned in an accurate and predictable manner by using an external stimulus have numerous applications in science and technology ranging from environmental cleanup to data storage.

Methods for modifying SAMs after their formation are critical for the development of surfaces that present the large, complex ligands and molecules needed for biology and biochemistry. Modification of the exposed surface of a SAM after formation would be advantageous for linking biological ligands that may be in short supply to surfaces because the amount of ligand required for immobilization is very small (nanomoles). Also,

incorporation of ligands into SAMs that are not compatible with synthetic methods can be achieved. Good candidate methods to create a switchable surfaces *via* simple modifications of SAMs are photochemically induced and electrochemically induced reactions [8]. Photochemical reactions can be combined with photolithography in which photolabile protecting groups are site-selectively removed upon exposure to light for microfabrication [36]. This kind of surface reaction will be discussed further in the Chapter 3.

Electrochemically induced surface reactions involve an electron transfer between a surface (e.g. gold and silicon) and a reaction site. Dynamic control of surface properties could be achieved by application of electrical potentials and reversible oxidation-reduction reactions. Langer and co-workers reported SAM surfaces which undergo dynamic changes in interfacial properties in response to an electrical potential [34]. The wettability was altered by the conformational transitions of the single-layered molecules between a hydrophilic and hydrophobic state. The stimuli-responsive changes in wettability are of interest for the development of micro- and nanofluidic devices, self-cleaning and anti-fog surfaces and sensor devices [12, 33, 37]. Biosensors, which transduce a bio-recognition event into measurable electronic or opto-electronic signals, have a crucial role in a wide range of applications, including clinical diagnosis, environmental monitoring, forensic analysis and anti-terrorism [14, 38]. Kwak and co-workers invented an enzyme-amplified immunosensor using redox mediation of a ferrocene-dendrimer which was immobilized to the electrode surface of carboxylic acids SAMs [39].

The development of substrates that dynamically regulate biological functions in response to applied stimuli can mimic the dynamic properties of biological systems. Surfaces that can modulate biomolecular activity, protein immobilization, and cell adhesion and

migration at the liquid-solid interface can be useful in diverse biological and medical applications [15, 17, 40-42]. Mrksich and Yousaf generated hydroquinone-presenting SAMs and the electrochemically oxidized quinone was used for immobilizing various functional molecules onto the surface through Diels-Alder reactions [43-45]. Although this strategy provides a rapid and selective immobilization of biomolecules, the syntheses of cyclopentadiene tethered molecules for Diels-Alder reactions are challenging. In particular, the use of cyclopentadiene for common solid-phase peptide synthesis is not feasible because the cyclopentadiene readily decomposes under cleavage conditions. Alternatively, the Michael addition provides a straightforward route by using sulfhydryl groups to conjugate biomolecules onto quinone surfaces. However the resulting quinone-thiol conjugate has a redox-active signal similar to that of the quinone starting material thus the product cannot be distinguished from the quinone by electrochemistry and the surface density of immobilized ligands cannot be determined [46, 47].

A novel coupling chemistry for the quinone molecules with oxyamine-functional group has been developed by Chan and Yousaf [48-50]. The approach allows for the immobilization of ligands with precise control of density onto an electroactive SAM of alkanethiols on gold. Based on this strategy we have designed and developed a stimuli-responsive SAM on which the surface property is dynamically changing. In this chapter the chemical method and the surface characterization for the novel dynamic surface will be discussed. The use of this surface in cell biology will be further discussed in chapters 2, 3 and 4.

Results and Discussion

*Synthesis of Hydroquinone Alkanethiol (**1d**)*

The hydroquinone-terminated alkanethiol (**1d**) was synthesized as shown in Figure 1-2. The *p*-dimethoxybenzene is deprotonated by the strong base *t*-butyllithium which reacts with undecenylbromide to provide 11-(2, 5-Dimethoxyphenyl)-1-undecene (**1a**). Subsequent photoaddition of **1a** in the presence of thiolacetic acid converted the alkene to a terminal thioacetate (**1b**). Addition of BBr_3 converted the methoxy groups on the aromatic ring to hydroxyl groups (**1c**). Acid hydrolysis of **1c** resulted in the removal of the acyl group to provide the hydroquinone alkanethiol (**1d**).

Electrochemical Characterization of SAM

The SAM was prepared by immersing the gold substrate in 1 mM ethanolic solution of hydroquinone alkanethiol (**1d**) for 12 hours. The conductivity of the SAM-coated gold can be used as a tool for surface characterization. Using a SAM-coated gold as the working electrode, the monolayer functionalized with redox-active groups responds to the electrochemical potential applied and the cyclic voltammetry provides information of the SAM surface. The electrochemical measurement was performed in 1 M $HClO_4$ using Ag/AgCl as reference electrode at a scan rate of 50 mV/s. The interconversion between hydroquinone and quinone is a reversible redox process in which two electrons and two protons are involved (Figure 1-3A). The hydroquinone alkanethiol had an oxidation potential of 580 mV and the quinone had a reduction potential of 44 mV versus Ag/AgCl reference

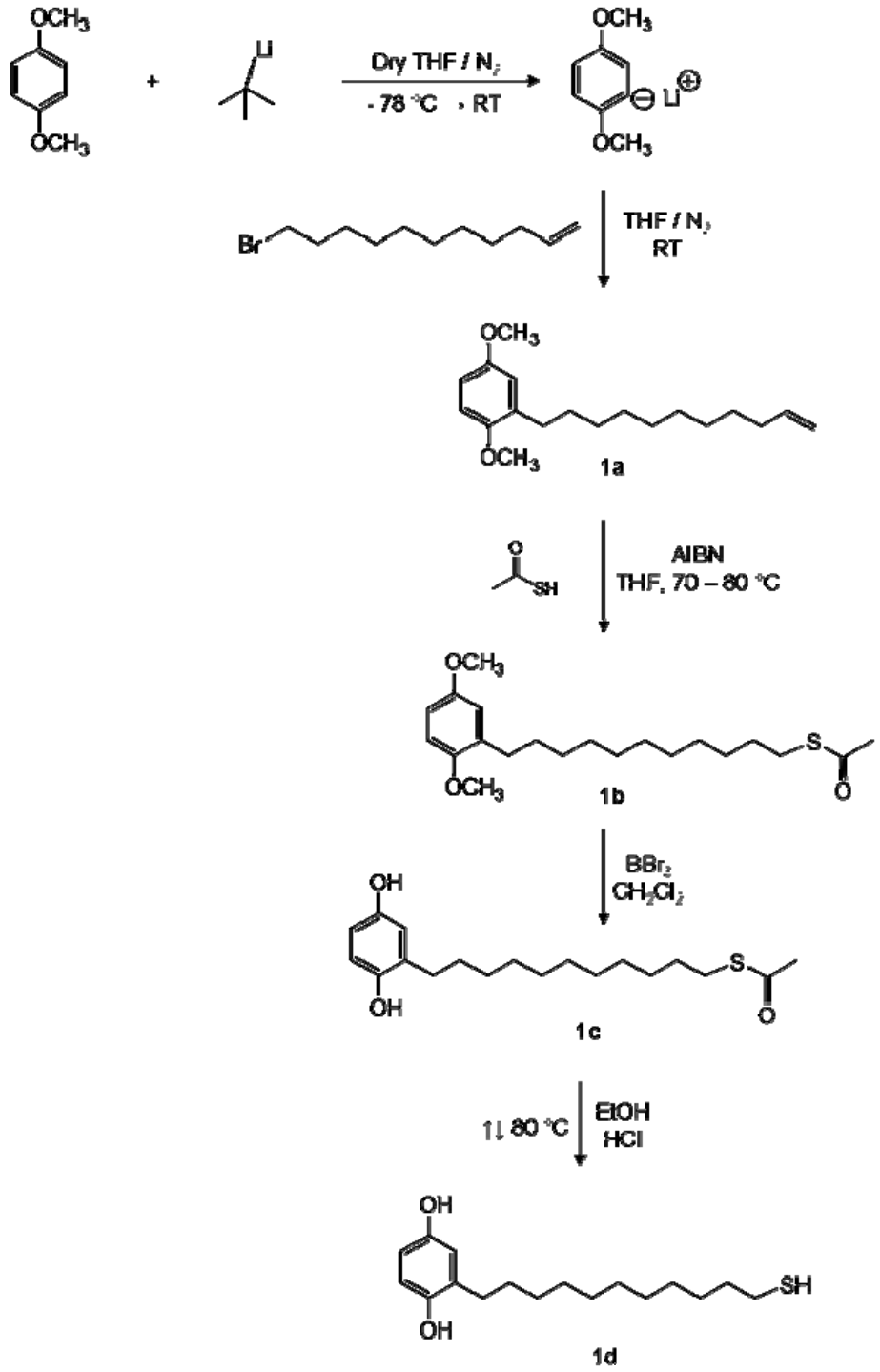

Figure 1-2. Synthetic route to hydroquinone alkanethiol (**1d**).

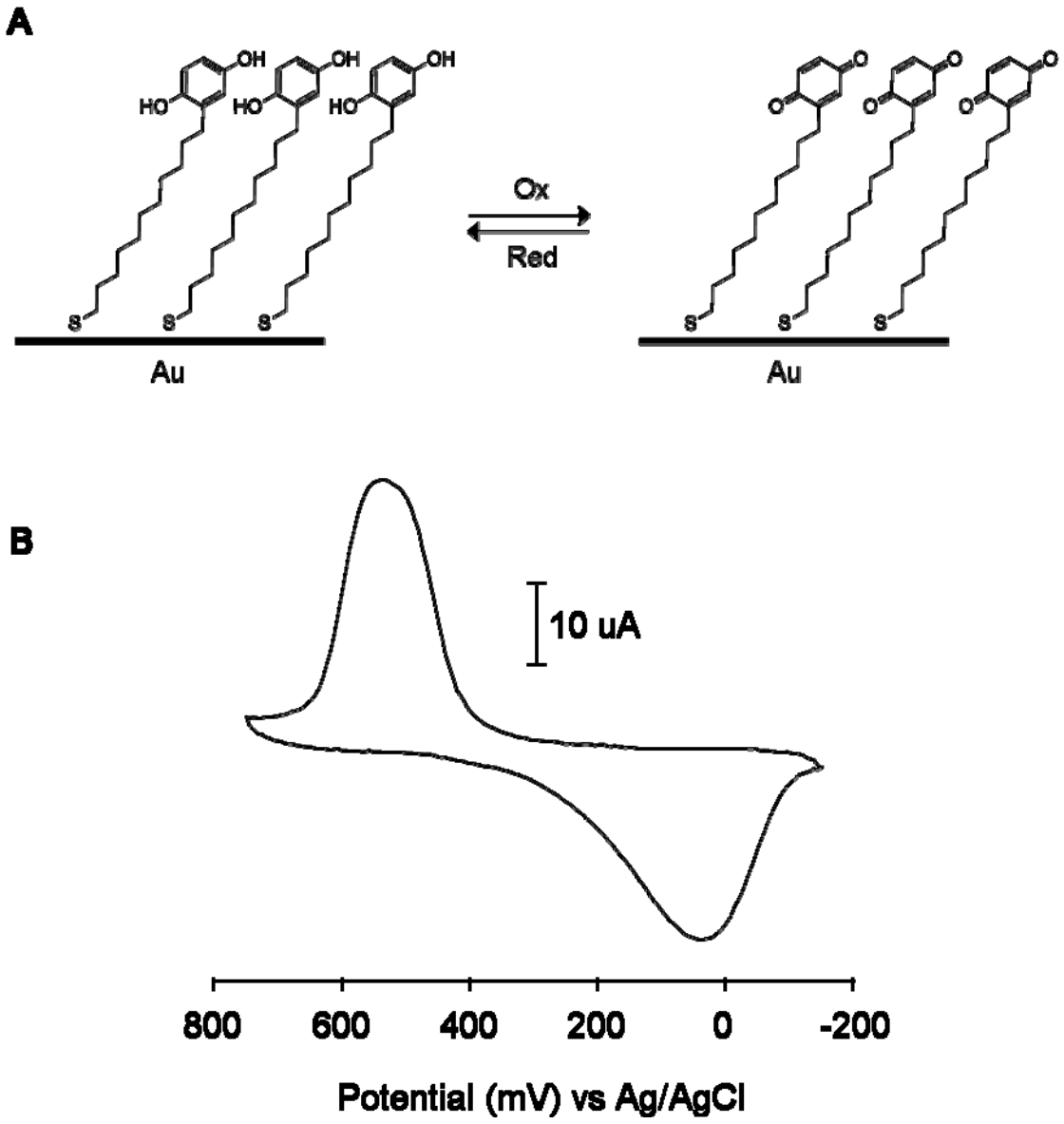

Figure 1-3. Characterization of redox active monolayers. A. The monolayer presenting hydroquinone alkanethiols undergo reversible two electron two proton redox process. B. Cyclic voltammetry of hydroquinone/quinone redox process.

electrode (Figure 1-3B). This redox process is reversible and the repetitive scan gives an overlapping cyclic voltammogram over 6 hours.

The Density of Redox-active Molecules in the Mixed Monolayers

The electric current in cyclic voltammetry is directly related to the number of redox-active molecules on the gold surface. The total charge (Q) that was consumed in the redox process is related to the density of redox-active molecules (Γ) by equation 1-1, where n is the number of electrons involved in the redox couple (n = 2 for hydroquinone/quinone), F is Faraday's constant, and A is the surface area of the electrode that is in contact with the electrolyte. Electric current is the flow of electric charge and it is expressed as in equation 1-2, where t is the time. Therefore the density of redox-active molecules on the gold surface is directly reflected in the peak current in cyclic voltammetry.

$$Q = nFA\Gamma \qquad \text{(equation 1-1)}$$

$$I = Q/t \text{ (for a steady flow) or } I = dQ/dt \qquad \text{(equation 1-2)}$$

$$\Gamma \propto I$$

It would be advantageous for the ultimate use of the SAM surface in presenting biological ligand for cell study model to precisely control the ligand density on the surface substrate. To achieve this we need to determine how effectively and consistently a SAM presenting a surface of redox active molecules can be generated. As discussed in the introduction, generally the monolayer is formed within a few minutes with 1 mM solution of alkanethiol. The 1 mM solution of mixed alkanethiols for making SAMs can be used to generate various

densities of a specific alkanethiol by mixing two or more kinds of alkanethiols in a different ratio. Ideally, it should be determined whether the density of chemisorbed alkanethiol on gold surface accurately reflects the density in solution which is used for SAM formation.

Since the peak current in cyclic voltammetry is directly related to the density of hydroquinone alkanethiol on a gold surface, an experiment was designed to compare the current values from different densities of hydroquinone alkanethiol. Mixed SAMs of hydroquinone (HQ)-terminated alkanethiol and hydroxyl group (OH)-terminated alkanethiol were prepared at various ratios with total concentration of 1 mM in an ethanol solution (the ratio of HQ/OH = 100/0, 75/25, 50/50, and 25/75). Using the SAM substrates as the working electrode, cyclic voltammetry was performed. Figure 1-4A shows the cyclic voltammogram of various mixed SAM surfaces. The substrate with higher ratio of HQ over OH in the SAM solution presents a stronger signal because more electroactive molecules are chemisorbed on the gold surface.

We determined the density of HQ groups on the monolayer by integrating the area under the reductive voltammetric wave. This integrated area represents the total charge (Q) that was consumed in the redox process and gave a density (Γ_{HQ}) of 2.3×10^{-10} mol/cm^2 (1.4×10^{14} molecules/cm^2) for the 50 % quinone monolayer and 4.9×10^{-10} mol/cm^2 (2.9×10^{14} molecules/cm^2) for the 100 % quinone monolayer (equation 1-1). The current change at 580 mV where hydroquinone oxidizes and at 44 mV where quinone reduces was recorded and it was plotted versus HQ volume density in the solution that was used for making mixed SAMs. As shown in Figure 1-4B, the plot generated straight lines (R^2 value > 0.99) and this indicates that the density of HQ in the SAM solution was consistently transferred to the gold

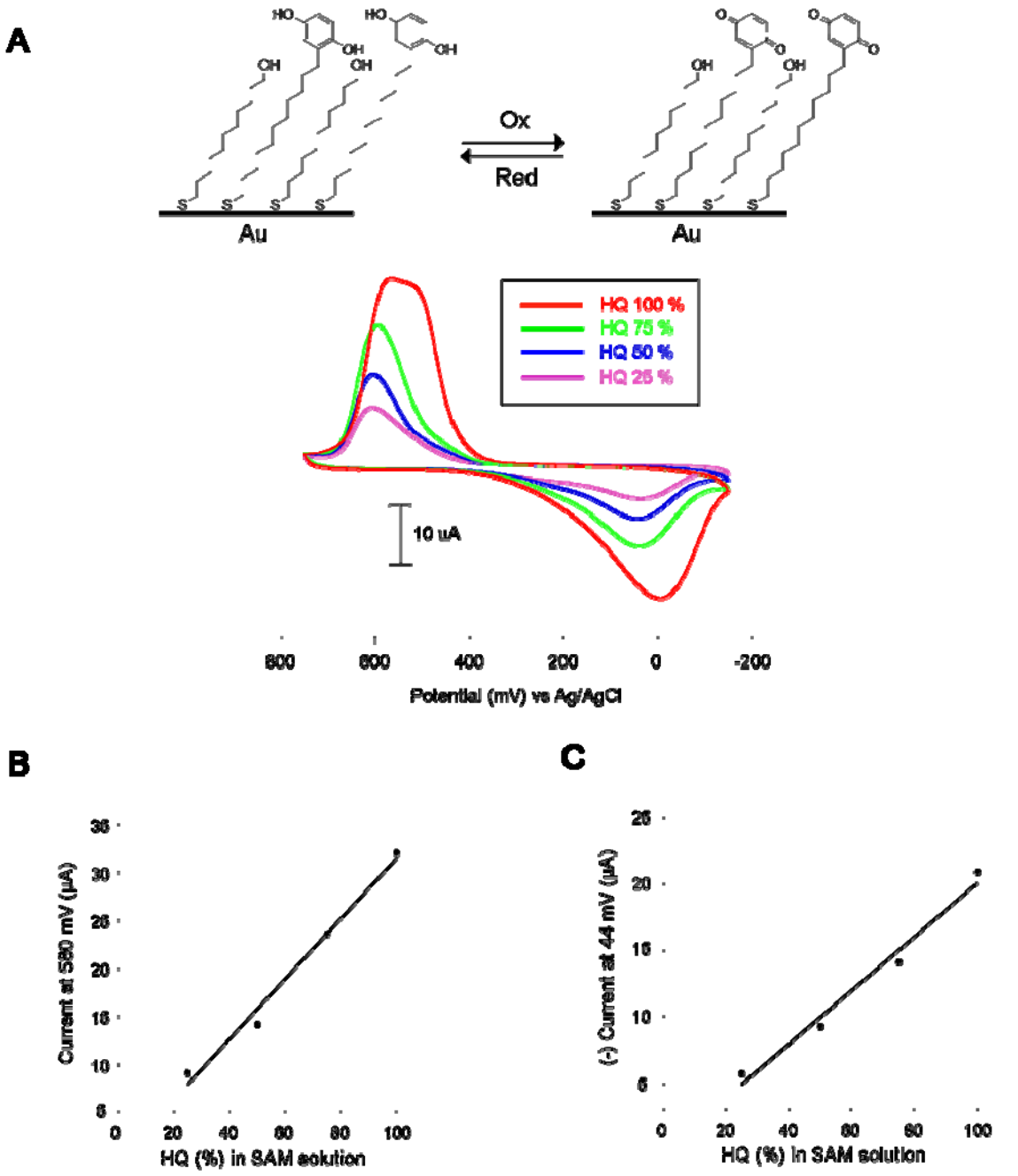

Figure 1-4. The relationship between electrochemical signals and the densities of redox active molecules on the SAMs. A. Cyclic voltammograms of mixed monolayers of hydroquinone- and hydroxyl group-terminated alkanethiols in different ratio. B and C. The changes of peak current at 580 mV (B) and 44 mV (C) from the cyclic voltammetry (A) were plotted against the density of hydroquinone alkanethiols in SAM solution. The linearity in both plots implies that the solution concentration of hydroquinone alkanethiol determines the actual surface concentration (density) of hydroquinone alkanethiol.

surface. In other words the mole fraction of HQ in solution ($\chi_{HQ\ solution}$) is equal to the mole fraction of HQ on surface ($\chi_{HQ\ surface}$). From this result we assume that the molecular density of HQ in the SAM solution is considered as the density of HQ on the gold surface.

Immobilization of Ligand onto the SAM Surface

We have developed a methodology for ligand immobilization to the SAM surface using oxime linkage in which ketone couples with an oxyamine functional group. The mixed monolayers of HQ-terminated alkanethiol (75 %) and OH-terminated alkanethiol (25 %) were prepared on gold surface. While the SAM substrate was applied with cyclic voltammetry (1 M $HClO_4$, 50 mV/s scan rate) small soluble oxyamine species, aminooxy acetic acid was added into the perchloric acid electrolyte solution at 150 mM concentration with stirring. The oxidized quinone on the SAM surface reacts with the oxyamine resulting in oxime adducts on the hydroquinone ring (Figure 1-5A). This coupling reaction is chemoselective and there is no side reaction. Figure 1-5B shows the cyclic voltammograms recorded during the interfacial reaction. The cyclic voltammogram (red line) shows the first scan of hydroquinone/quinone. Addition of soluble aminooxy acetic acid resulted in the loss of peak currents for the quinone monolayer. However the oxime product has its own reversible conversion between oxidized form and reduced form. The increase in peak currents corresponding to the oxidation (480 mV) and reduction (350 mV) of the oxime product was observed over time. Independently, aminooxy acetic acid-tethered quinone alkanethiol was synthesized and the monolayer's cyclic voltammograms showed identical peak currents as the immobilization product. This confirms that the new redox-active peaks in Figure 1-5B originated from the reaction of aminooxy acetic acid and quinone monolayer.

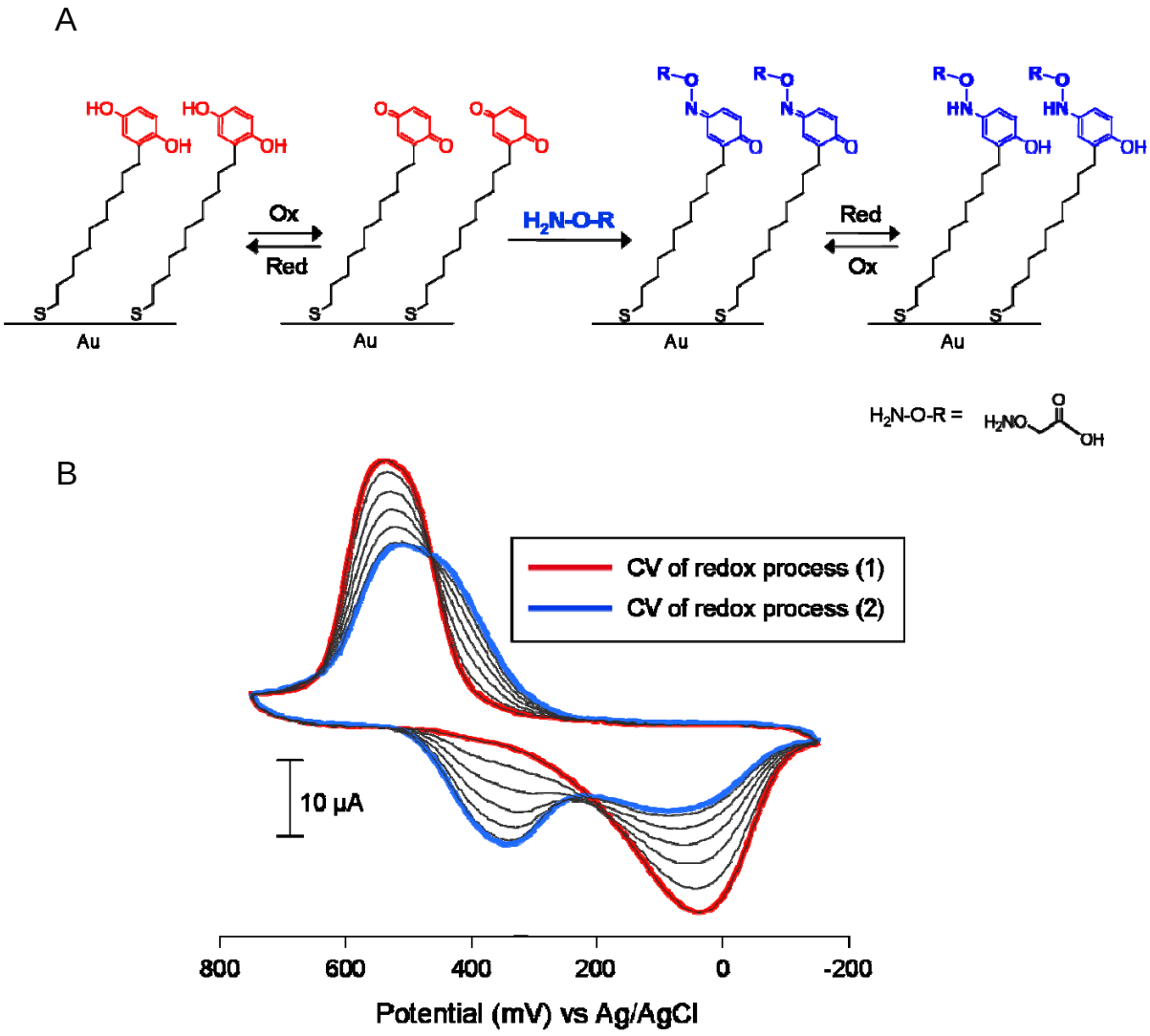

Figure 1-5. Ligand immobilization onto the SAM surface by oxime formation. A. Redox-active hydroquinone monolayer undergoes electrochemical oxidation to the quinone. The resulting quinone then reacts chemoselectively with aminooxy acetic acid to give the corresponding oxime. B. Cyclic voltammograms recorded in 10-min intervals at a scan rate of 50 mV/s showed the extent of the interfacial reaction between soluble aminooxy acetic acid (150 mM) and quinone monolayer. The peaks at 580 mV and 44 mV correspond to the redox coupling of the quinone, whereas the peaks at 480 mV and 350 mV correspond to the redox peaks of the product oxime.

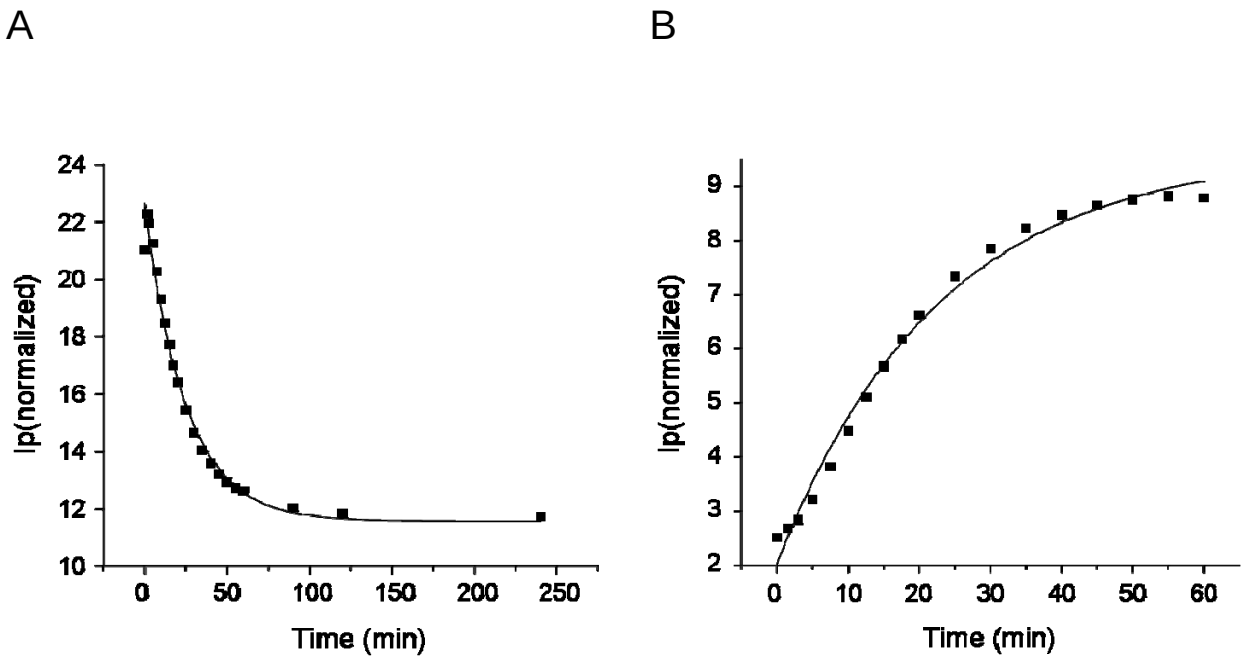

Figure 1-6. Characterization of ligand immobilization reaction on the SAM surface. The change of peak current at 30 mV and 330 mV from the cyclic voltamograms of Figure1-5B were plotted against time. They give the rates of the decrease of quinone monolayer (A) and the formation of oxime on the surface (B).

As the potentials for oxidation and reduction of oxime are distinguished from those of hydroquinone/quinone, the extent of the interfacial reaction can be monitored *in situ* by cyclic voltammetry.

Since the peak current changes in the cyclic voltammetry are the consequences of quinone consumption and oxime formation, they provide kinetic information of the interfacial reaction. The plot in Figure 1-6 shows the peak current changes versus time for the cyclic voltammograms shown in Figure 1-5B. The decrease is at 30 mV and the increase is at 330 mV in the peak currents. The rate for the loss in peak currents of the quinone monolayer (30 mV) would follow pseudo first-order kinetics because the aminooxy acetic acid was in large excess relative to the immobilized quinone. The data was fitted to an exponential decay (equation 1-3) to obtain a pseudo first-order rate constant (k') of 0.040 min^{-1}, where I_t is the peak current at time t, I_0 is the initial peak current and I_f is the residual nonfaradaic current.

$$I_t = I_f + (I_0 - I_f)\, e^{-k't} \qquad \text{(equation 1-3)}$$

The increase of the peak current at 330 mV for the formation of oxime gave the pseudo first-order rate constant of 0.044 min^{-1}. The excellent fit of the experimental data to this equation ($R^2 > 0.98$) indicates that quinone groups are sufficiently isolated on the monolayer that the reactivity is independent of the extent of the reaction.

Synthesis of Tetra(ethylene glycol) alkanethiol

Proteins and cells tend to adhere to glass or hydrophobic surfaces and it is a significant challenge to create an inert surface which is resistant to non-specific adsorption of proteins or

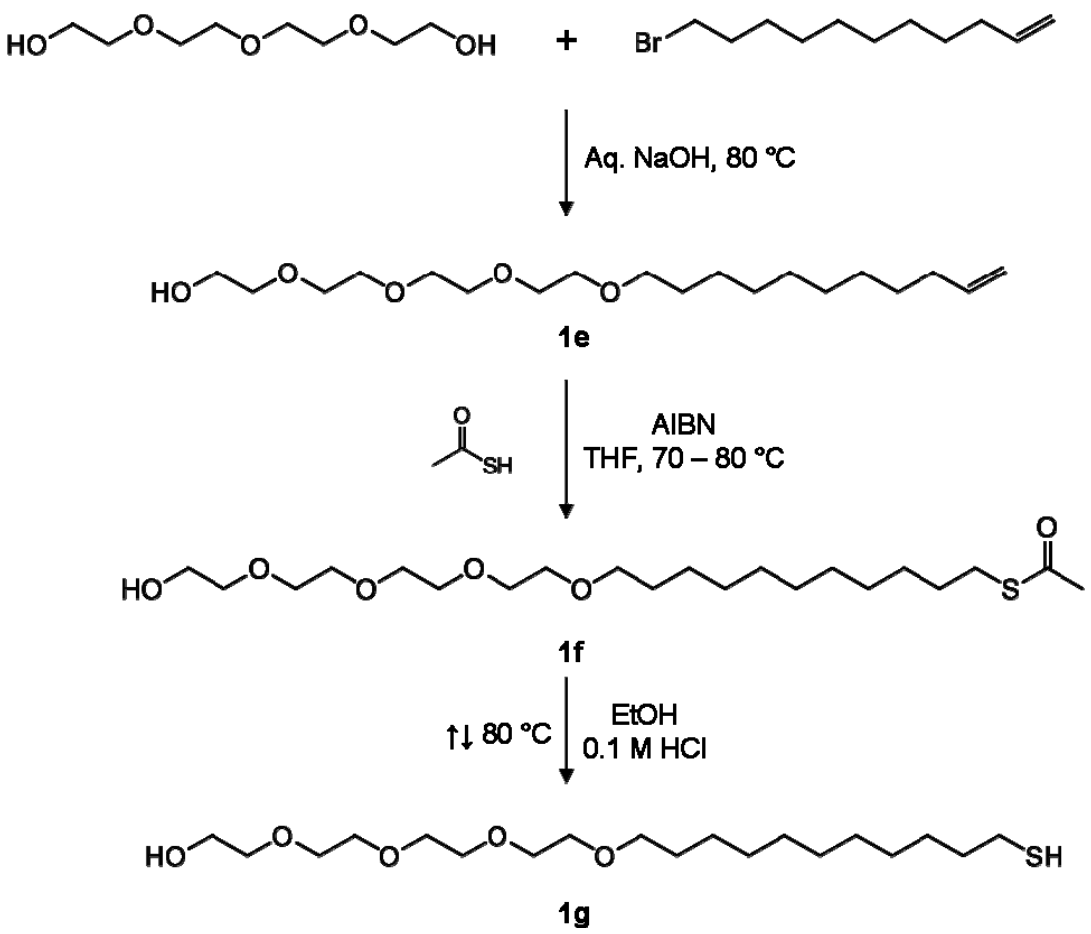

Figure 1-7. Synthetic route of tetra(ethylene glycol) alkanethiol (**1g**).

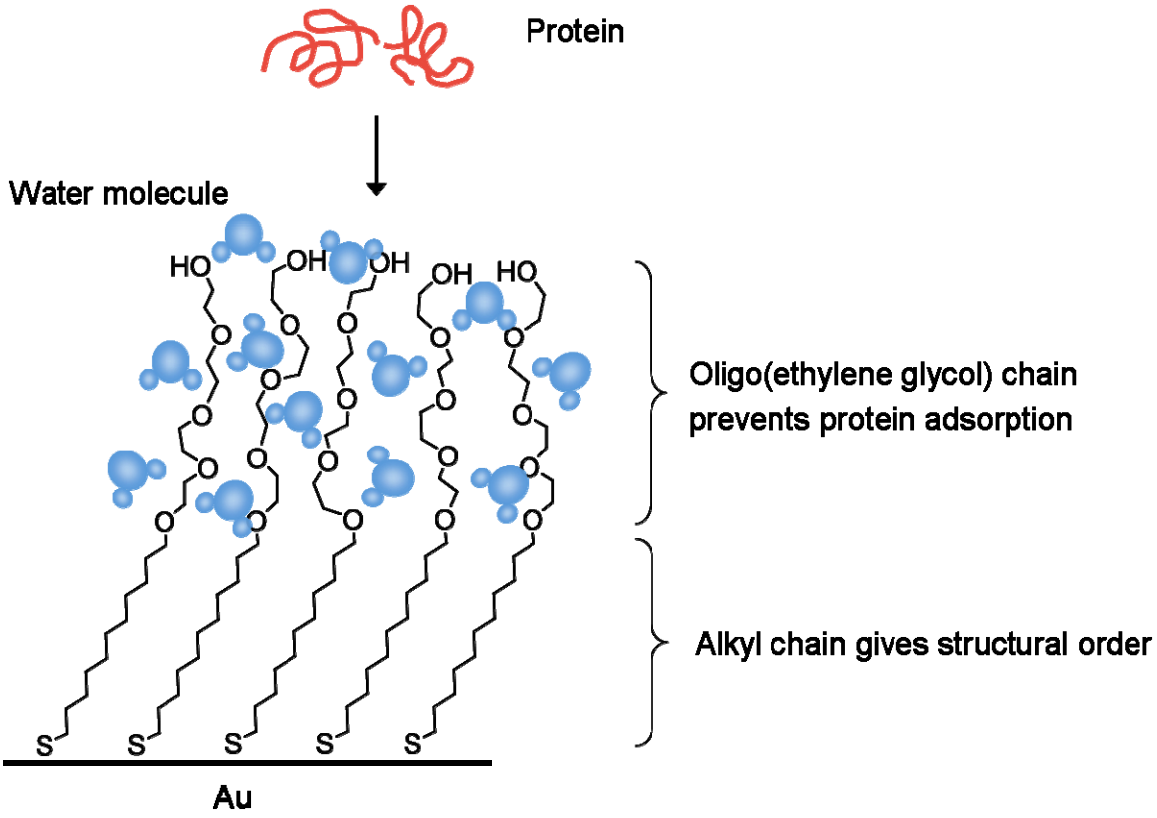

Figure 1-8. Structure of inert SAMs.The oligo(ethylene glycol) groups prevent the adsorption of protein and the alkyl chains provide structural order. The adsorption of protein is energetically unfavorable as the process requires loss of hydration energy and degree of freedom for the oligo(ethylene glycol) layer.

cells in order to study biospecific interactions on the surface. Oligo(ethylene glycol) groups are well known to reduce non-specific protein adsorption and have desired degrees of hydrophilicity and adsorptivity toward biological molecules [16, 51-53]. As depicted in Figure 1-7, an alkanethiol functionalized with tetra(ethylene glycol) group was synthesized (**1g**). The C_{11} alkyl chain contributes to the structural order of the SAM on the gold surface and the tetra(ethylene glycol) chain prevents protein adsorption onto the monolayer (Figure 1-8). The resistance of oligo(ethylene glycol) groups (EG) to the adsorption of proteins is generally considered a steric repulsion effect, where the EG prevents the protein from reaching the substrate surface to adsorb [53]. Protein resistance is only observed for the RT stable hydrated phase of EG. When the protein reaches the interphase by diffusion and compresses the EG layer, removal of water molecules from solvated EG chains and lessening conformational freedom of EG chains bring loss in both enthalpy and entropy. Thus the protein cannot be adsorbed onto the monolayer. The SAM substrate produced with 100 % tetra(ethylene glycol)-alkanethiol is completely inert and it was observed that no cells or protein attached to the substrate even after a week of incubation under cell culture conditions.

Synthesis of Hydroquinone-tetra(ethylene glycol) alkanethiol

To make mixed SAM with tetra(ethylene glycol)-terminated alkanethiol for a protein adsorption-resistant surface, hydroquinone alkanethiol conjugated with tetra(ethylene glycol) groups was synthesized (Figure 1-9). Acid catalyzed addition of dihydropyran (DHP) to hydroquinone provided the protected di-tetrahydropyran-hydroquinone (**1h**). Deprotonation of **1h** with *t*-butyllithium followed by addition of dibromobutane provided the di-

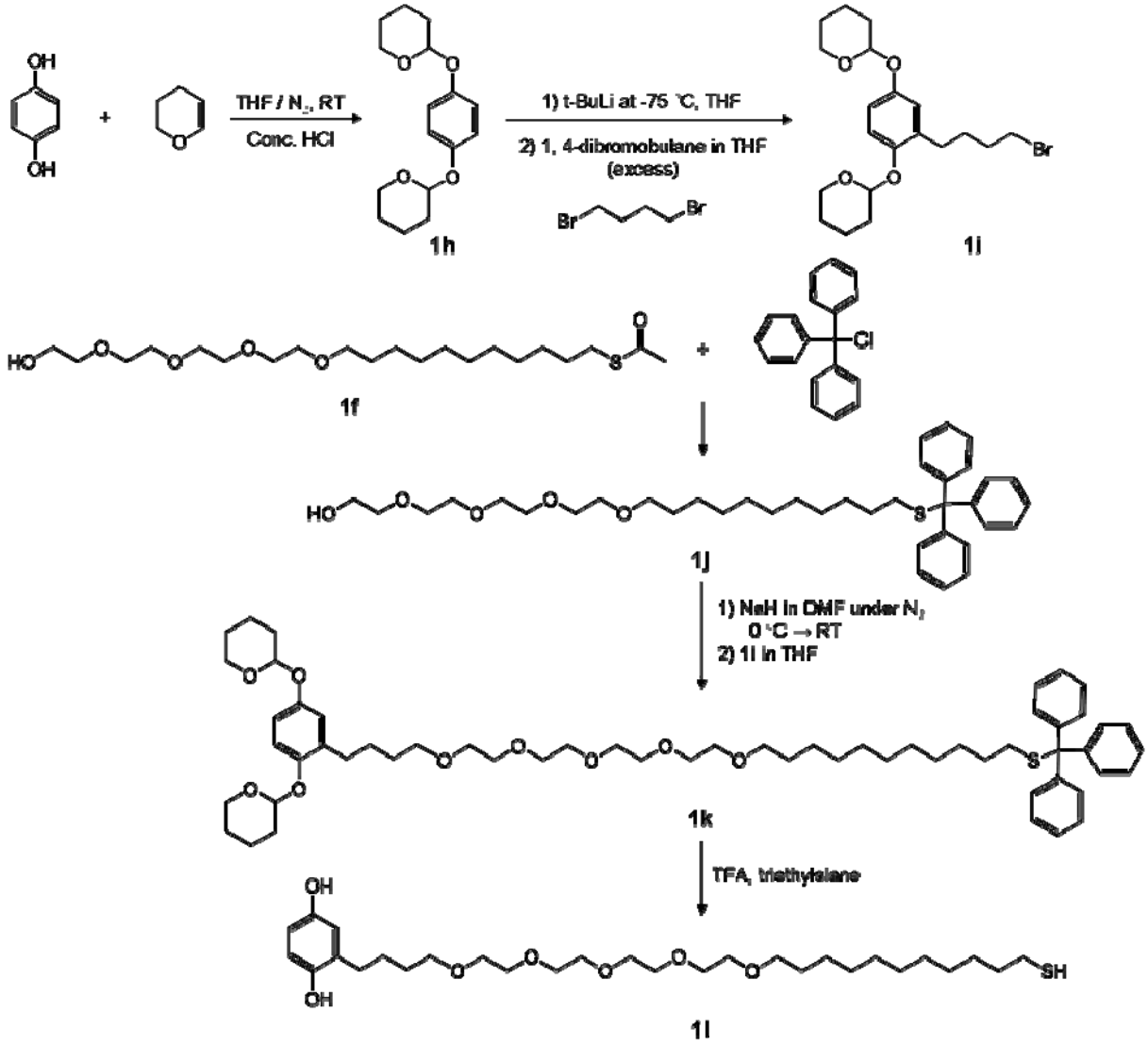

Figure 1-9. Synthetic route to hydroquinone-tetra(ethylene glycol) alkanethiol (**1l**). SAMs that present this molecule mixed with oligo(ethylene glycol)groups resist the non-specific adsorprtion of protein.

tetrahydropyran-hydroquinone-butylbromide (**1i**). Addition of sodium hydride to deprotonate tetra(ethylene glycol)alkanethiol-trityl (**1j**) followed by addition of the bromide (**1i**) afforded the conjugate (**1k**). The conjugate was deprotected with trifluoroacetic acid (TFA) to provide the hydroquinone-tetra(ethylene glycol)alkanethiol (**1l**).

Immobilization of Biological Ligand on the SAM Surface

The tripeptide RGD sequence is found within the central binding domain of several adhesive proteins present in extracellular matrix [54-57]. To mimic the adhesive proteins a short peptide that included the RGD sequence was synthesized with the N-terminal modified to have an oxyamine functional group.

A mixed SAM with tetra(ethylene glycol)alkanethiol and hydroquinone-tetra(ethylene glycol)alkanethiol was prepared (50:50 ratio on surface) and the electrochemical potential was applied to the substrate in 1 M perchloric acid. Oxyamine-tethered RGD was added in perchloric acid with stirring (in 20 mM concentration). Figure 1-10 shows the cyclic voltammogram of before and after the reaction with oxyamine-RGD. Hydroquinone oxidizes at 540 mV and the quinone reduces at 320 mV. After the oxime formation, characterization of the monolayer by cyclic voltammetry shows diagnostic peaks that correspond to the oxidation (620 mV) and reduction (480 mV) of the oxime conjugate. Integration of the area under the oxime reductive peak gave a density consistent with the complete conversion of the quinone monolayers to the RGD oxime conjugate. The monolayers on gold are stable within the range of applied electrochemical potential with repeated redox scanning for several hours producing indistinguishable cyclic voltammograms. The ability of cyclic voltammetry to

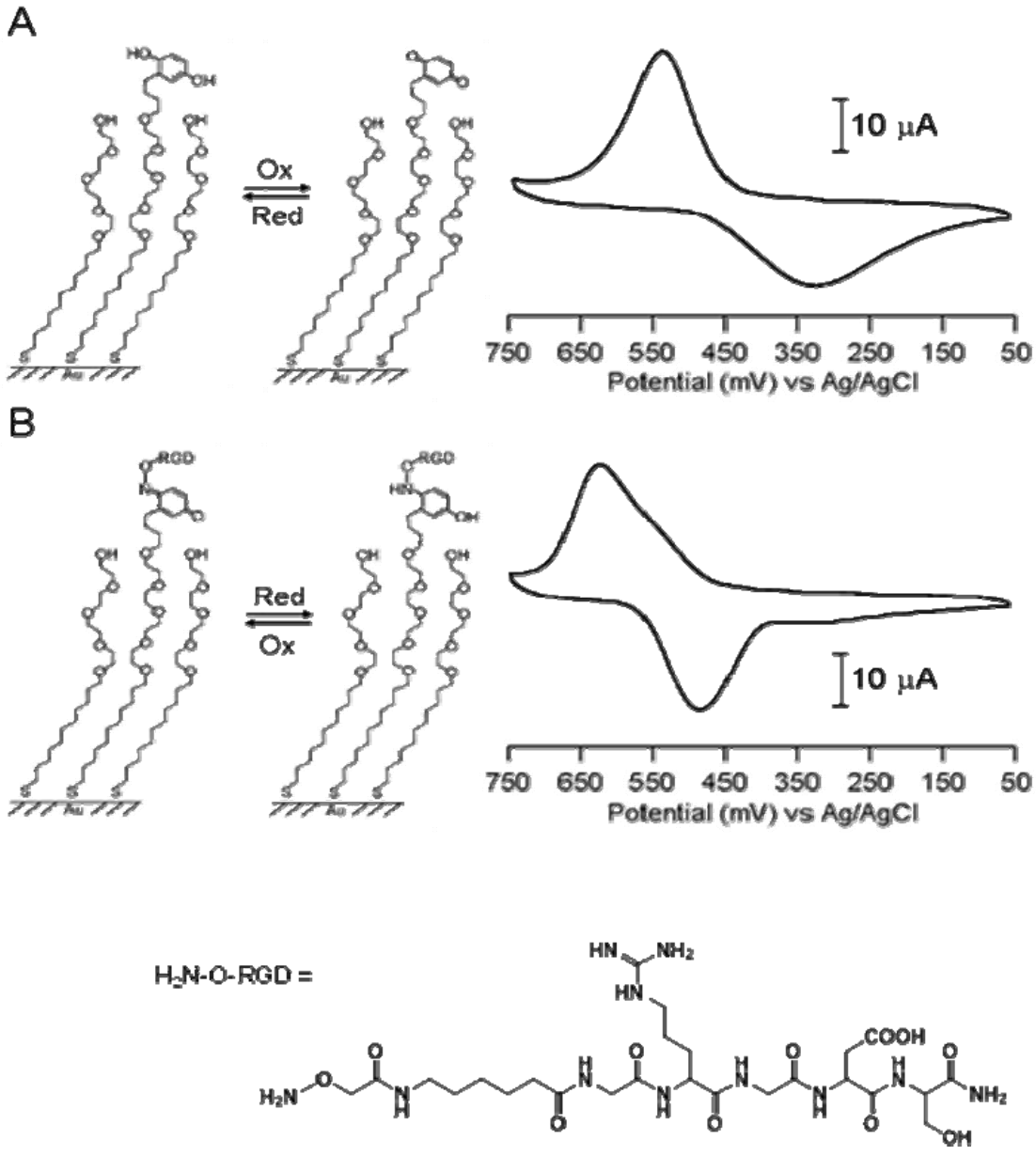

Figure 1-10. Cyclic voltammogram characterization of the electroactive monolayers. Mixed monolayer of alkanethiolates presenting hydroquinone (50 %) and tetra(ethylene glycol) (50 %) groups on gold was used as working electrode. Electrochemistry was performed at a scan rate of 50 mV/s in 1 M $HClO_4$. A. The hydroquinone monolayer is reversibly oxidized to the quinone at 540 mV and reduced back at 320 mV. B. The oxime conjugate with RGD peptide has characteristic peaks at 620 mV (oxidation) and 480 mV (reduction). The cyclic voltammograms were used to determine the extent and yield of the interfacial reaction.

distinguish the oxime product from the initial hydroquinone-quinone redox couple enables the quantification of the amount of ligand molecules installed on the surface.

Conclusion

The SAMs of hydroquinone alkanethiols were used for the immobilization of oxyamine group-functionalized ligands. The electrochemistry based on the differing signal between hydroquinone/quinone and the oxime product enabled characterization of the density of the immobilized ligand on the substrate surface. To apply this electroactive substrate in cell biology, a SAM with resistance to the non-specific protein adsorption was prepared and a biological ligand (RGD peptide) was successfully immobilized onto the substrate surface.

Materials and Methods

All the solvents for the synthetic procedures were HPLC grade. THF was distilled from sodium benzophenone under nitrogen before use. Absolute ethanol was purchased from Aaper Alcohol & Chemical Company. Flash chromatography was carried out using silica gel (230 – 400 mesh). All amino acids and resin were purchased from Anaspec, Inc. (La Jolla, CA). All other chemical reagents were purchased from Sigma Aldrich and Acros and used as received.

*11-(2, 5-Dimethoxyphenyl)-1-undecene (**1a**)*

Under an atmosphere of nitrogen 2.0 g of *p*-dimethoxybenzene (14.5 mmol) was dissolved in 20 mL of dry THF. The solution was cooled to -78 °C using dry ice/acetone bath, and *t*-butyllithium solution in pentane (1.7 M, 10.23 mL, 17.4 mmol) was added over a

period of 30 minutes. The resulting yellow solution was stirred at RT for 1 hour and a solution of undecenylbromide (1.88 mL, 8.66 mmol) in THF (10 mL) was added. The colorless reaction mixture was stirred for 12 hours at RT under atmosphere of nitrogen. The reaction mixture was concentrated by rotary evaporation and diluted with ethyl acetate. The solution was washed with saturated NH_4Cl solution, water, and brine and dried over Na_2SO_4. The organic layer was concentrated to a pale yellow oil and purified by column chromatography with hexane/ethyl acetate (96/4) to give 2.3 g of product as colorless oil (91.5 % yield). ^{1}H NMR (400 MHz, $CDCl_3$) δ 1.26 (br s, 12 H), 1.52 (br s, 2 H), 2.01 (q, 2 H), 2.55 (t, 2 H, J = 7.7 Hz), 3.75 (s, 3 H), 3.76 (s, 3 H), 4.89-5.0 (m, 2 H), 5.79 (m, 1 H), 6.64-6.75 (m, 3 H).

*11-(2, 5-Dimethoxyphenyl)-1-(thioacetyl)undecane (**1b**)*

Solution of **1a** (2.3 g, 7.92 mmol) in dry THF (50 mL) was refluxed under an atmosphere of nitrogen followed by the addition of AIBN (2, 2'-azobisisobutyronitrile, 40-50 mg). Into the reaction flask thiolacetic acid (1.132 mL, 15.838 mmol) was added dropwise and the reaction was stirred for 12 hours with refluxing. The reaction mixture was concentrated and purified by column chromatography with hexane/ethyl acetate (8/2) to afford 2.4 g of product (82.7 % yield). ^{1}H NMR (400 MHz, $CDCl_3$) δ 1.24 (br s, 14 H), 1.54 (m, 4 H), 2.30 (s, 3 H), 2.54 (t, 2 H, J = 7.7 Hz), 2.84 (t, 2 H, J = 7.3 Hz), 3.74 (s, 3 H), 3.75 (s, 3 H), 6.64-6.87 (m, 3 H).

*11-(2, 5-Dihydroxylphenyl)-1-(thioacetyl)undecane (**1c**)*

A solution of **1b** (2.4 g, 6.55 mmol) in anhydrous methylene chloride (50 mL) was cooled to -78 °C using a dry ice/acetone bath. Under an atmosphere of nitrogen, boron

tribromide (6.19 mL, 65.5 mmol) was added and the mixture was allowed to warm to RT and stirred for 2 hours. The reaction was cooled to -78 °C and quenched by addition of diethyl ether and water. The organic layer was washed with water and brine and dried over Na_2SO_4. The removal of the solvent gave yellow solid and was used for the next reaction without further purification. ^{1}H NMR (400 MHz, $CDCl_3$) δ 1.24 (br s, 14 H), 1.54 (m, 4 H), 2.31 (s, 3 H), 2.52 (t, 2 H, J = 7.7 Hz), 2.84 (t, 2 H, J = 7.4 Hz), 6.43-6.70 (m, 3 H).

*11-(2, 5-Dihydroxylphenyl)-1-mercaptoundecane (**1d,** Hydroquinone alkanethiol)*

The crude product **1c** (assuming 6.55 mmol) was dissolved in MeOH (50 mL) and concentrated HCl (12 M, 5 mL) was added. The mixture was heated to reflux for 12 hours. The removal of the solvent resulted in a white solid and was dissolved in a small volume of ethyl acetate. The reaction product residue was precipitated by adding into hexane. The hexane was removed after centrifuge at 5000 rpm for 15 min. The residue was further purified by column chromatography with hexane/ethyl acetate (75/25) to give 0.7 g of product as white powder (36 % yield). ^{1}H NMR (400 MHz, $CDCl_3$) δ 1.26 (br s, 14 H), 1.56 (m, 4 H), 2.47-2.54 (m, 4 H), 6.51-6.63 (m, 3 H).

*Undec-1-en-11-yltetra(ethylene glycol) (**1e**)*

In an oil bath at 80 °C, tetra(ethylene glycol) (7.77 g, 40 mmol) was slowly added with 6.43 mmol of saturated aqueous NaOH (0.26 g) and stirred for 30 minutes, and 1.0 g of 11-bromo-1-undecene (4.29 mmol) was then added. After 24 hours the reaction mixture was extracted with hexane. The removal of hexane by rotary evaporation at the reduced pressure resulted in a yellow oil. Purification by column chromatography on silica gel with ethyl acetate gave 1.10 g of the product (74 % yield). ^{1}H NMR (400 MHz, $CDCl_3$) δ 1.25 (br s, 12

H), 1.55 (qui, 2 H), 2.02 (q, 2 H), 3.42 (t, 2 H), 3.56-3.70 (m, 16 H), 4.89-4.99 (m, 2 H), 5.73-5.84 (m, 1 H).

*1-(Thiolacetyl)undec-11-yltetra(ethylene glycol) (**1f**)*

Solution of **1e** (1.10 g, 3.18 mmol) in dry THF (15 mL) was refluxed under an atmosphere of nitrogen followed by the addition of AIBN (2, 2'-azobisisobutyronitrile, 5-7 mg). Two equivalents of thiolacetic acid (0.45 mL, 6.36 mmol) were added dropwise and the reaction mixture was stirred for 12 hours under reflux conditions. Concentration of the reaction mixture by rotary evaporation at reduced pressure followed by purification by column chromatography with ethyl acetate gave the thioacetate (1.0 g) in 74.5 % yield. ^{1}H NMR (400 MHz, $CDCl_3$) δ 1.24 (br s, 14 H), 1.53 (m, 4 H), 2.30 (s, 3 H), 2.84 (t, 2 H, J = 7.4 Hz), 3.42 (t, 2 H, J = 6.8 Hz), 3.56-3.72 (m, 16 H).

*1-Mercaptoundec-11-yltetra(ethylene glycol) (**1g**)*

A solution of **1f** (1.0 g, 2.37 mmol) in 0.1 M HCl in EtOH (20 mL) was refluxed for 12 hours. The solvent was removed by rotary evaporation and the resulting yellow oil was dissolved in ethyl acetate. To neutralize 1 M $NaHCO_3$ was added and the organic layer was separated by using a separatory funnel. After washing with water and brine solution the reaction mixture was concentrated and purified by column chromatography with ethyl acetate to give the thiol (0.8 g) in 88.8 % yield. ^{1}H NMR (400 MHz, $CDCl_3$) δ 1.24 (br s, 14 H), 1.55 (m, 4 H), 2.50 (q, 2 H, J = 7.4 Hz), 3.42 (t, 2 H, J = 6.8 Hz), 3.56-3.71 (m, 16 H).

*Di-tetrahydropyran-hydroquinone (**1h**)*

To a solution of hydroquinone (3.4 g, 30.0 mmol) in THF (20 mL) was added 3, 4-dihydro-2H-pyran (10.39 g, 123 mmol) and 0.5 mL of concentrated HCl. The reaction

mixture was stirred for 10 hours at RT. The clear solution was concentrated by rotary evaporation and the resulted white solid was dissolved in methylene chloride. The mixture was washed with 1 M $NaHCO_3$ and brine, and dried over Na_2SO_4. Concentration of the solution by rotary evaporation resulted in white solid and was purified by recrystallization in methylene chloride (7.2 g, 86.2 % yield). ^{1}H NMR (400 MHz, $CDCl_3$) δ 1.59-1.66 (m, 6 H), 1.80-1.84 (m, 4 H), 1.94-1.97 (m, 2 H), 3.47-3.55 (m, 2 H), 3.88-3.94 (m, 2 H), 5.28 (t, 2 H, J = 3.2 Hz), 6.95 (s, 4 H).

*Di-tetrahydropyran-hydroquinone-butylbromide (**1i**)*

To a solution of **1h** (1.9 g, 6.9 mmol) in dry THF (20 mL) at -75 °C, *t*-butyllithium solution in pentane (1.7 M, 4.5 mL, 7.7 mmol) was added dropwise over 20 minutes under an atmosphere of nitrogen. This mixture was stirred for 30 minutes and then brought slowly (over 2 hours) to 0 °C and stirred for an additional 30 minutes to quench any excess *t*-butyllithium. To this solution excess 1, 4-dibromobutane (2.4 mL, 20.7 mmol) in THF was added dropwise over 20 minutes. A white precipitate was immediately formed but after stirring for 12 hours the solution became clear yellow in color. The reaction mixture was then diluted with 40 mL of methylene chloride and washed with NH_4Cl (25 mL) and brine (25 mL), dried over Na_2SO_4 and concentrated to a yellow oil. Silica gel chromatography using gradient elution (hexane/ethyl acetate from 20/1 to 10/1) afforded the product (2.13 g, 5.15 mmol, 74.7 %) as a clear oil. ^{1}H NMR (400 MHz, $CDCl_3$) δ 1.62-2.02 (m, 16 H), 2.66 (t, 2 H, J = 7.5 Hz), 3.44 (t, 2 H, J = 7.8 Hz), 3.58-3.62 (m, 2 H), 3.88-3.98 (m, 2 H), 5.28-5.32 (m, 2 H), 6.84-6.87 (m, 2 H), 7.02-7.05 (m, 1 H).

*Tetra(ethylene glycol)undecanethiol-trityl (**1j**)*

To a solution of 1-(thiolacetyl)undec-11-yltetra(ethylene glycol)) (**1f**) (2.0 g, 4.73 mmol) in absolute EtOH (40 mL) was added concentrated HCl (1.5 mL). The reaction mixture was refluxed for 16 hours and cooled to RT. The pH of the solution was adjusted to 7 with 5 % methanolic NH_4OH. The solution was extracted with methylene chloride and the resulted crude oil was added with dry THF (40 mL) and triphenylmethyl chloride (2.0 g, 7.17 mmol). The reaction mixture was stirred under nitrogen at RT for 18 hours and then concentrated. The purification by column chromatography with hexane/ethyl acetate (1/1) gave the product (1.4 g, 47.5 % yield). ^{1}H NMR (400 MHz, $CDCl_3$) δ 1.14-1.26 (m, 16 H), 1.55 (m, 2 H), 2.10 (t, 2 H, J = 7.3 Hz), 2.74 (s, 1 H), 3.42 (t, 2 H, J = 6.8 Hz), 3.56-3.71 (m, 16 H), 7.16-7.19 (m, 3 H), 7.23-7.27 (m, 6 H), 7.37-7.40 (m, 6 H).

*Di-tetrahydropyran-hydroquinone-tetra(ethylene glycol)alkane-trityl (**1k**)*

To a solution of **1j** (4.2 g, 6.7 mmol) in DMF (10 mL) at 0 °C was added NaH (480 mg, 20 mmol) slowly. This reaction mixture was stirred at 0 °C for 1 hour and then stirred at RT for 2 hours. During this time bubbles were observed in the reaction mixture. To this solution **1i** dissolved in 5 mL THF (5.45 g, 13.2 mmol) was added dropwise. The reaction mixture was stirred for another 5 hours at RT then diluted with 40 mL of ethyl acetate. This reaction mixture was then washed with NH_4Cl and brine, and dried over Na_2SO_4. The resulting yellow oil was purified by column chromatography with hexane/ethyl acetate (1/1) to give the product as a clear oil (3.3 g, 51.6 %). ^{1}H NMR (400 MHz, $CDCl_3$) δ 1.19-1.4 (m, 20 H), 1.59-1.68 (m, 8 H), 1.83-1.87 (m, 4 H), 1.96-2.01 (m, 2 H), 2.15 (t, 2 H, J = 6.8 Hz), 2.65 (t, 2 H, J = 7.0 Hz), 3.44-3.51 (m, 4 H), 3.58-3.67 (m, 18 H), 3.92-3.95 (m, 2 H), 5.30-5.20 (m,

2 H), 6.84-6.88 (m, 2 H), 7.02-7.04 (m, 1 H), 7.18-7.22 (m, 3 H), 7.26-7.30 (m, 6 H), 7.42-7.45 (m, 6 H).

*Hydroquinone-tetra(ethylene glycol) alkanethiol (**1l**)*

To a solution of trityl (**1k**) (971 mg, 1.25 mmol) in 10 mL of methylene chloride was added triethylsilane (0.2 mL, 2.5 mmol) and trifluoroacetic acid (0.1 mL, 5% solution in CH_2Cl_2). This reaction mixture was stirred at RT for 8 hours and then concentrated to a yellow oil. Silica gel chromatography with hexane/ethyl acetate (1/1) afforded the product as a clear oil (0.52 g, 76.3 %). ^{1}H NMR (400 MHz, $CDCl_3$) δ 1.26-1.35 (m, 18 H), 1.58-1.63 (m, 4 H), 2.53-2.55 (m, 2 H), 2.63 (t, 2 H, J = 6.8 Hz), 3.48 (t, 2 H, J = 7.5 Hz), 3.57 (t, 2 H, J = 6.7 Hz), 3.60-3.68 (m, 16 H), 6.55-6.58 (m, 1 H), 6.64-6.69 (m, 2 H).

Preparation of Monolayers

All gold substrates were prepared by electron-beam deposition of titanium (3 nm) and then gold (12 nm) on glass cover slips (7.5 cm × 2.5 cm). All gold coated glass substrates were cut into 1 cm^2 pieces and washed with absolute ethanol. The substrates were immersed in an ethanolic solution containing the alkanethiols (1 mM) for 12 hours, and then cleaned with ethanol prior to each experiment.

Electrochemical Measurements

All electrochemical experiments were performed using a BAS 100B/W Electrochemical Analyzer (Bioanalytical Systems, Inc., West Lafayette, IN). Electrochemistry on SAMs was performed in 1 M $HClO_4$, using a platinum wire as the counter electrode, Ag/AgCl as reference, and the gold SAM substrate as the working electrode. All cyclic voltammograms were recorded at a scan rate of 50 mV/s.

Solid-Phase Peptide Synthesis - Linear RGD

All peptides were synthesized by automated solid phase peptide synthesis using a CS136XT Peptide Synthesizer (CS Bio Co., Menlo Park, CA).

Fmoc (9-fluorenylmethoxycarbonyl)-protected amino acids were used on Fmoc-Ser(tBu)-Rink Amide-MBHA resin. Synthesized peptide was cleaved from the resin by agitating in a solution of trifluoroacetic acid (TFA):water:triisopropylsilane (95:2.5:2.5) for 3 hours. TFA was evaporated and the cleaved peptide was precipitated in cold diethyl ether. The water-soluble peptide was extracted with water and lyophilized. Mass spectral data confirmed the peptide product. MS (ESI) (m/z): $[M+H^+]$ calculated for linear RGD-oxyamine ($C_{25}H_{45}N_{11}O_{11}$), 676.69; found, 676.5. $[M+H^+]$ calculated for control scrambled peptide, GRD-oxyamine ($C_{25}H_{45}N_{11}O_{11}$), 676.69; found, 676.4. $[M+H^+]$ calculated for control soluble peptide RGD ($C_{17}H_{31}N_9O_8$), 490.48; found, 490.3.

REFERENCES

1. Ulman, A., *Formation and structure of self-assembled monolayers.* Chem. Rev., 1996. **96**: p. 1533-1554.

2. Love, J.C., et al., *Self-assembled monolayers of thiolates on metals as a form of nanotechnology.* Chem. Rev., 2005. **105**: p. 1103-1169.

3. Badia, A., R.B. Lennox, and L. Reven, *A dynamic view of self-assembled monolayers.* Acc. Chem. Res., 2000. **33**: p. 475-481.

4. Chechik, V., R.M. Crooks, and C.J.M. Stirling, *Reactions and reactivity in self-assembled monolayers.* Adv. Mater., 2000. **12**: p. 1161-1171.

5. Allara, D.L. and R.G. Nuzzo, *Spontaneously organized molecular assemblies. 1. Formation, dynamics, and physical properties of n-alkanoic acids adsorbed from solution on an oxidized aluminum surface.* Langmuir, 1985. **1**: p. 45-52.

6. Porter, M.D., et al., *Spontaneously organized molecular assemblies. 4. structural characterization of n-alkyl thiol monolayers on gold by optical ellipsometry, infrared spectroscopy, and electrochemistry.* J. Am. Chem. Soc., 1987. **109**: p. 3559-3568.

7. Tao, Y.T., *Structural comparison of self-assembled monolayers of n-alkanoic acids on the surfaces of silver, copper, and aluminum.* J. Am. Chem. Soc., 1993. **115**: p. 4350-4358.

8. Choi, I.S. and Y.S. Chi, *Surface reactions on demand: electrochemical control of SAM-based reactions.* Angew. Chem. Int. Ed., 2006. **45**: p. 4894-4897.

9. Dubois, L.H. and R.G. Nuzzo, *Synthesis, structure, and properties of model organic surfaces.* Annu. Rev. Phys. Chem., 1992. **43**: p. 437-463.

10. Horn, T., et al., *Incorporation of chemoselective functionalities into peptides via solid-phase submonomer synthesis.* Bioconjugate Chem., 2004. **15**: p. 428-435.

11. Mrksich, M., *A surface chemistry approach to studying cell adhesion.* Chem. Soc. Rev., 2000. **29**: p. 267-273.

12. Gras, S.L., et al., *Intelligent control of surface hydrophobicity.* ChemPhysChem, 2007. **8**: p. 2036-2050.

13. Mrksich, M., *What can surface chemistry do for cell biology?* Curr. Opin. Chem. Biol., 2002. **6**: p. 794-797.

14. Shin, S.K., et al., *Nanoscale controlled self-assembled monolayers and quantum dots.* Curr. Opin. Chem. Biol., 2006. **10**: p. 423-429.

15. Yousaf, M.N. and M. Mrksich, *Dynamic substrates: modulating the behaviors of attached cells.* In new technologies for life sciences: a trends guide, 2002: p. 28-35.

16. Prime, K.L. and G.M. Whitesides, *Self-assembled organic monolayers: model systems for studying adsorption of proteins at surfaces.* Science, 1991. **252**(5009): p. 1164-1167.

17. Yeo, W.-S., M.N. Yousaf, and M. Mrksich, *Dynamic interfaces between cells and surfaces: electroactive substrates that sequentially release and attach cells.* J. Am. Chem. Soc., 2003. **125**: p. 14994-14995.

18. Fan, C., K.W. Plaxco, and A.J. Heeger, *Electrochemical interrogation of conformational changes as a reagentless method for the sequence-specific detection of DNA.* Proc. Natl. Acad. Sci. U.S.A., 2003. **100**: p. 9134-9137.

19. Houseman, B.T., E.S. Gawalt, and M. Mrksich, *Maleimide-functionalized self-assembled monolayers for the preparation of peptide and carbohydrate biochips.* Langmuir, 2003. **19**: p. 1522-1531.

20. Nuzzo, R.G., F.A. Fusco, and D.L. Allara, *Spontaneously organized molecular assemblies. 3. Preparation and properties of solution adsorbed monolayers of organic disulfides on gold surfaces.* J. Am. Chem. Soc., 1987. **109**: p. 2358-2368.

21. Strong, L. and G.M. Whitesides, *Structures of self-assembled monolayer films of organosulfur compounds adsorbed on gold single crystals: electron diffraction studies.* Langmuir, 1988. **4**: p. 546-558.

22. Bain, C.D., et al., *Formation of monolayer films by the spontaneous assembly of organic thiols from solution onto gold.* J. Am. Chem. Soc., 1989. **111**: p. 321-335.

23. Biebuyck, H.A., C.D. Bain, and G.M. Whitesides, *Comparison of organic monolayers on polycrystalline gold spontaneously assembled from solutions containing dialkyl disulfides or aklanethiols.* Langmuir, 1994. **10**: p. 1825-1831.

24. Walczak, M.M., et al., *Structure and interfacial properties of spontaneously adsorbed n-alkanethiolate monolayers on evaporated silver surfaces.* J. Am. Chem. Soc., 1991. **113**: p. 2370-2378.

25. Nuzzo, R.G., L.H. Dubois, and D.L. Allara, *Fundamental studies of microscopic wetting on organic surfaces. 1. Formation and structural characterization of a self-consistent series of polyfunctional organic monolayers.* J. Am. Chem. Soc., 1990. **112**: p. 558-569.

26. Nuzzo, R.G., B.R. Zegarski, and L.H. Dubois, *Fundamental studies of the chemisorption of organosulfur compounds on gold (111). Implications for molecular self-assembly on gold surfaces.* J. Am. Chem. Soc., 1987. **109**: p. 733-740.

27. Li, Y., et al., *Characterization of thiol self-assembled films by laser desorption Fourier transform mass spectrometry.* J. Am. Chem. Soc., 1992. **114**: p. 2428-2432.

28. Widrig, C.A., C. Chung, and M.D. Porter, *The electrochemical desorption of n-alkanethiol monolayers from polycrystalline Au and Ag electrodes.* J. Electroanal. Chem., 1991. **310**(335-359).

29. Bryant, M.A. and J.E. Pemberton, *Surface Raman scattering of self-assembled monolayers formed from 1-alkanethiols: behavior of films at gold and comparison to films at silver.* J. Am. Chem. Soc., 1991. **113**: p. 8284-8293.

30. Bain, C.D. and G.M. Whitesides, *Formation of two-component surfaces by the spontaneous assembly of monolayers on gold from solutions containing mixtures of organic thiols.* J. Am. Chem. Soc., 1988. **110**: p. 6560-6561.

31. Mendes, P.M., *Stimuli-responsive surfaces for bio-applications.* Chem. Soc. Rev., 2008. **37**: p. 2512-2529.

32. Zhou, F. and W.T.S. Huck, *Surface grafted polymer brushes as ideal building blocks for "smart" surfaces.* Phys. Chem. Chem. Phys., 2006. **8**: p. 3815-3823.

33. Alexander, C. and K.M. Shakesheff, *Responsive polymers at the biology/materials science interface.* Adv. Mater., 2006. **18**: p. 3321-3328.

34. Lahann, J., et al., *A reversibly switching surface.* Science, 2003. **299**: p. 371-374.

35. Liu, Y., et al., *Controlled switchable surface.* Chem. Eur. J., 2005. **11**: p. 2622-2631.

36. Chan, E.W.L. and M. Yousaf, *A photo-electroactive surface strategy for immobilizing ligands in patterns and gradients for studies of cell polarization.* Mol. BioSyst., 2008. **4**: p. 746-753.

37. Howarter, J.A. and J.P. Youngblood, *Self-cleaning and anti-fog surfaces via stimuli-responsive polymer brushes.* Adv. Mater., 2007. **19**: p. 3838-3843.

38. Xiao, Y., et al., *A reagentless signal-on architecture for electronic, aptamer-based sensors via target-induced strand displacement.* J. Am. Chem. Soc., 2005. **127**: p. 17990-17991.

39. Kwon, S.J., et al., *An electrochemical immunosensor using ferrocenyl-tethered dendrimer.* Analyst, 2006. **131**: p. 402-406.

40. Yousaf, M.N., B.T. Houseman, and M. Mrksich, *Turning on cell migration with electroactive substrates.* Angew. Chem. Int. Ed., 2001. **40**: p. 1093-1096.

41. Hayashi, G., et al., *Photoregulation of a peptide-RNA interaction on a gold surface.* J. Am. Chem. Soc., 2007. **129**: p. 8678-8679.

42. Liu, Y., et al., *Controlled protein assembly on a switchable surface.* Chem. Commun., 2004: p. 1194-1195.

43. Yousaf, M.N., E.W.L. Chan, and M. Mrksich, *The kinetic order of an interfacial Diels-Alder reaction depends on the environment of the immobilized dienophile.* Angew. Chem. Int. Ed., 2000. **39**: p. 1943-1946.

44. Yousaf, M.N. and M. Mrksich, *Diels-Alder reaction for the selective immobilization of protein to electroactive self-assembled monolayers.* J. Am. Chem. Soc., 1999. **121**: p. 4286-4287.

45. Kwon, Y. and M. Mrksich, *Dependence of the rate of an interfacial Diels-Alder reaction on the steric environment of the immobilized dienophile: an example of enthalpy-entropy compensation.* J. Am. Chem. Soc., 2002. **124**: p. 806-812.

46. Curreli, M., et al., *Selective functionalization of In2O3 nanowire mat devices for biosensing applications.* J. Am. Chem. Soc., 2005. **127**: p. 6922-6923.

47. Brown, E.R., K.T. Finley, and R.L. Reeves, *Steric effects of vicinal substituents on redox equilibriums in quinoid compounds.* J. Org. Chem., 1971. **36**: p. 2849-2853.

48. Chan, E.W.L. and M.N. Yousaf, *Immobilization of ligands with precise control of density to electroactive surfaces.* J. Am. Chem. Soc., 2006. **128**: p. 15542-15546.

49. Chan, E.W.L. and M.N. Yousaf, *Site-selective immobilization of ligands with control of density on electroactive microelectrode arrays.* ChemPhysChem, 2007. **8**: p. 1469-1472.

50. Chan, E.W.L. and M.N. Yousaf, *Surface chemistry control to silence gene expression in Drosophila Schneider 2 cells through RNA interference.* Angew. Chem. Int. Ed., 2007. **46**: p. 3881-3884.

51. Prime, K.L. and G.M. Whitesides, *Adsorption of proteins onto surfaces containing end-attached oligo(ethylene oxide): a model system using self-assembled monolayers.* J. Am. Chem. Soc., 1993. **115**: p. 10714-10721.

52. Pale-Grosdemange, C., et al., *Formation of self-assembled monolayers by chemisorption of derivatives of oligo(ethylene glycol) of structure HS(CH2)11(OCH2CH2)mOH on gold.* J. Am. Chem. Soc., 1991. **113**: p. 12-20.

53. Harder, P., et al., *Molecular conformation in oligo(ethylene glycol)-terminated self-assembled monolayers on gold and silver surfaces determines their ability to resist protein adsorption.* J. Phys. Chem. B, 1998. **102**: p. 426-436.

54. Giancotti, F.G. and E. Ruoslahti, *Integrin signaling.* Science, 1999. **285**: p. 1028-1032.

55. Huttenlocher, A., R.R. Sandborg, and A.F. Horwitz, *Adhesion in cell migration.* Curr. Opin. Cell Biol., 1995. **7**: p. 697-706.

56. Maheshwari, G., et al., *Cell adhesion and motility depend on nanoscale RGD clustering.* J. Cell Sci., 2000. **113**(10): p. 1677-1686.

57. Ruoslahti, E. and M.D. Pierschbacher, *New perspectives in cell adhesion: RGD and integrins.* Science, 1987. **238**(4826): p. 491-497.

CHAPTER 2

Application of Model Substrate in Cell Biology

Introduction

Cell Adhesion, Extracellular Matrix, and Integrins

Cells do not live in static surroundings, they exist in highly evolving dynamic environments [1]. Cells adapt and communicate to their environment by numerous methods ranging from differentiation, gene expression, growth and apoptosis [2-8]. Numerous cellular responses that have essential roles in the regulation of cellular behavior and fate are triggered by cell interactions with the extracellular matrix (ECM) and with neighboring cells [9, 10]. As the ECM provides the physical microenvironment in which cells live, it provides a substrate for cell anchorage, serves as a tissue scaffold, and guides cell migration. The ECM is also responsible for transmitting environmental signals to cells, which influence essentially all aspects of a cell's life, including its proliferation, differentiation and death.

Adhesions with the ECM are formed by essentially all types of adherent cell, but their morphology, size and subcellular distribution can be quite different. Nonetheless many of these adhesions are commonly mediated by integrins which are heterodimeric receptors composed of at least one β and one α subunit. From among the cellular repertoire of 18 α subunits and 8 β subunits, at least 24 distinct heterodimers can be formed, each binding to distinct ECM ligands [11-13]. The extracellular ligands that anchor these adhesions include

fibronectin, vitronectin and various collagens. Integrin-mediated adhesion activates signals that regulate a number of cellular processes including cell migration, proliferation, and differentiation [14]. Based on information provided by electron microscopy and X-ray crystallography, integrins are thought to possess affinity regulation mechanisms *via* structural change (Figure 2-1) [15, 16].

The adhesions can be characterized into subgroups such as focal adhesion (also termed focal contact), fibrillar adhesion, focal complex and podosome (Table 2-1) [4]. Focal adhesions are flat, elongated structures that are several square microns in area, and are often located near the periphery of cells [17]. They mediate strong adhesion to the substrate, and they anchor bundles of actin microfilaments through a plaque that consists of many different proteins which include vinculin, talin, paxilliln and tyrosine-phosphorylated proteins (Figure 2-2). Development of focal adhesions is stimulated by the small GTPase RhoA. In more central locations of many cell types are the fibrillar adhesions, which are elongated or dot-like structures that are associated with ECM fibrils [18]. Focal complexes are small dot-like adhesions which are present mainly at the edges of the lamellipodium [19, 20]. These adhesions are often associated with cell migration or serve as precursors of focal adhesions. Their formation is induced by the Rho-family GTPase Rac. Podosomes are small (~0.5 μm diameter) cylindrical structures containing typical focal contact proteins that are found in various malignant cells and in some normal cells [21].

More than 50 different molecules are found either stably or transiently in focal adhesions. The key mechanism for regulation of the adhesion assembly is achieved by integrins [13]. The most common integrins found in focal adhesions and other ECM

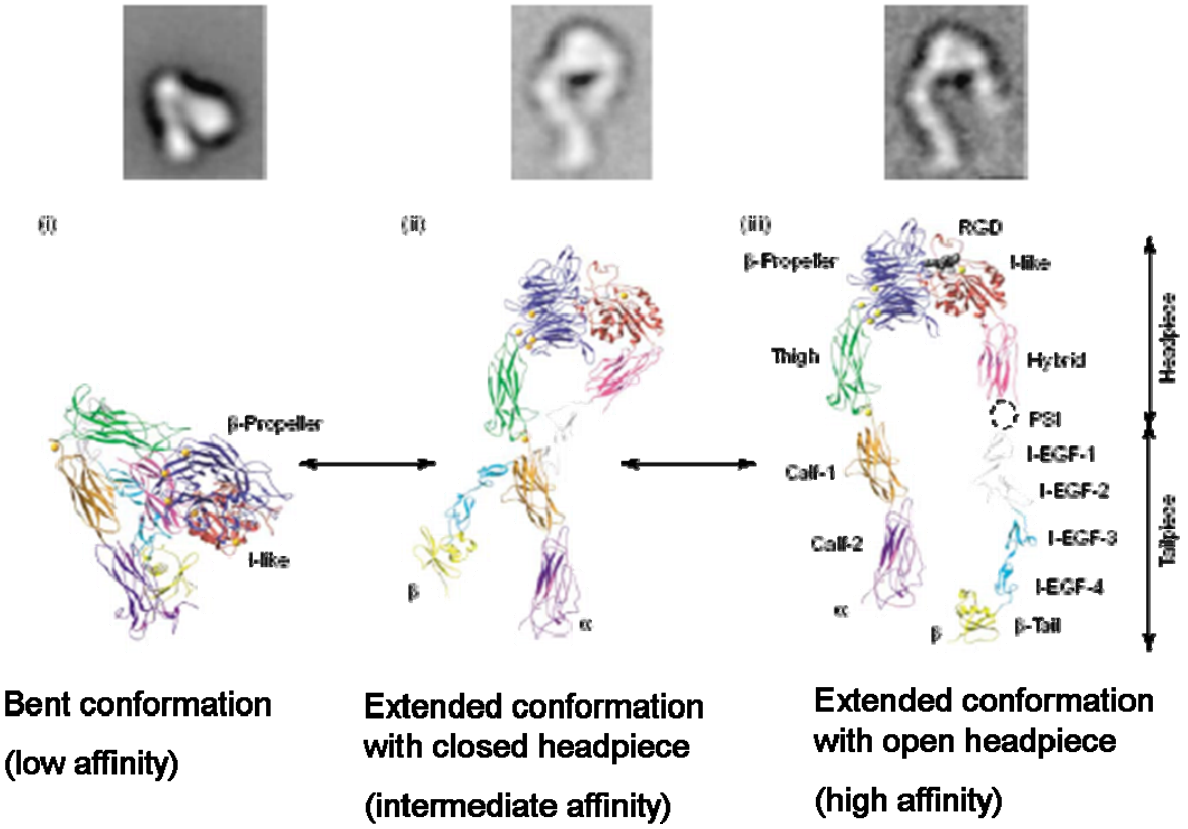

Figure 2-1. Global and local integrin conformational changes associated with affinity regulation. Switchblade model for global integrin conformation regulation defined by electron microscopy (upper panel) and ribbon diagrams based on the bent crystal structure (lower panel) is shown. (i) Bent conformation (low affinity) (ii) Extended conformation with closed headpiece (predicted to be of intermediate affinity) (iii) Extended conformation with open headpiece (high affinity). This figure was taken and modified from reference 15.

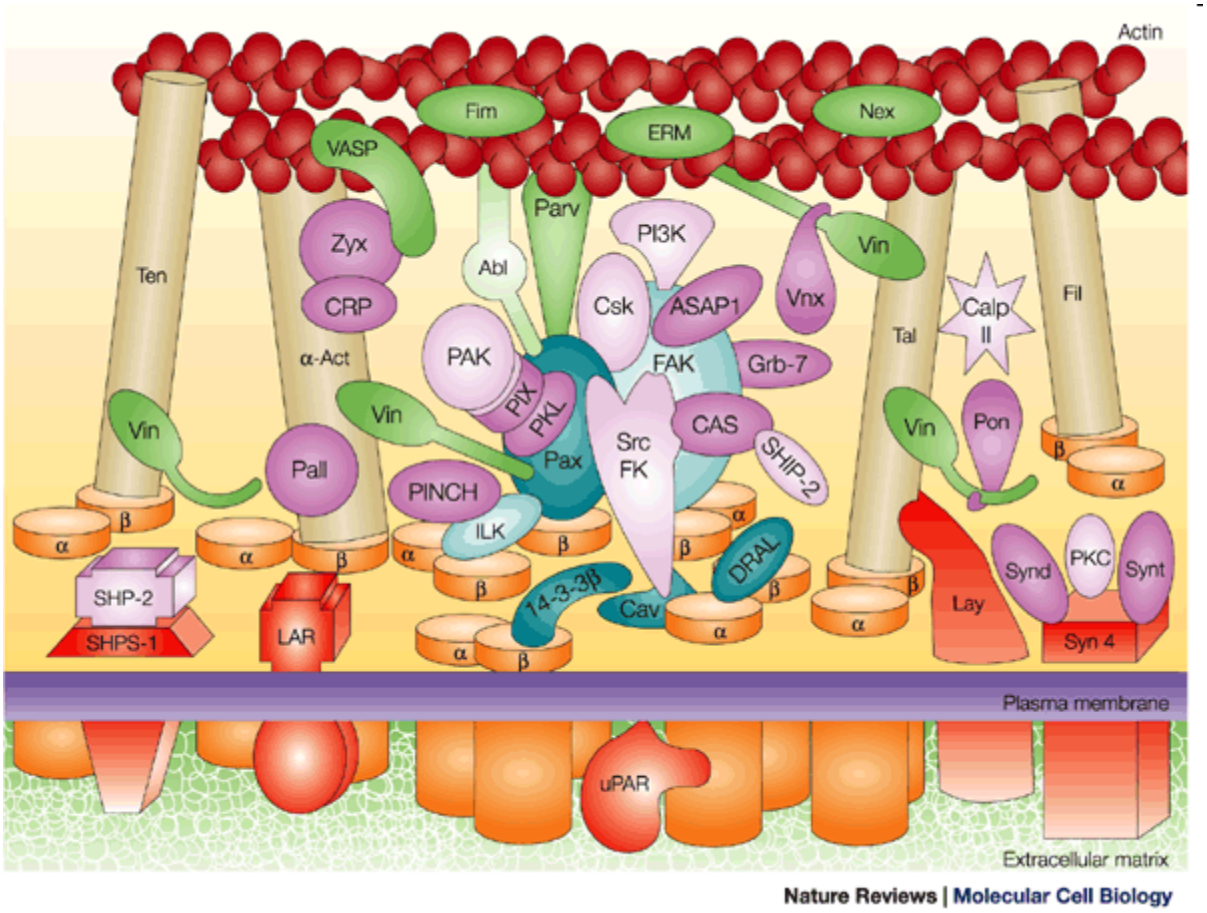

Figure 2-2. Schematic diagram showing the complexity of the cell-ECM adhesion interaction. This figure was taken from reference 4.

adhesions are $\alpha_5\beta_1$ (the classical fibronectin receptor) and $\alpha_v\beta_3$ (vitronectin receptor) [4]. Unlike classical growth factor receptors, integrins bind ligands in a mechanosensory fashion that requires the assembly of a focal adhesion complex associated with the actin cytoskeleton. Assembly of a mature signaling complex requires integrin ligands to provide mechanical resistance, which opposes the contractile force of the associated actin cytoskeleton and promotes continued ligation events as new integrins are recruited into the growing focal complex. The actual mechanism by which integrins are internalized by the cell and returned to the front for making new attachments is mostly unknown, although it is widely assumed that some are taken up by clathrin-coated pits and returned to the cell surface *via* the endocytic cycle [22, 23]. However, it is clear that different integrins on the surfaces of cells in suspension do circulate into and out of cells at quite different rates.

The ECM provides a structural scaffold and informational cues [24]. The composition of the ECM can change as a function of the "remodeling" processes that occur during thrombosis and wound healing, differentiation, and a wide variety of pathological processes. Notably, local remodeling of the ECM can occur quickly during these processes, as the induction of new ECM proteins is dynamically influenced by cues from the local microenvironment. Selection of the appropriate matrix for experiments using cultured cells is crucial, as it can profoundly affect the cellular response. Not only is the molecular composition of the ECM important, but also its topography and mechanical properties. These features of the ECM are determined both by the cells that produce it and by the cells that grow on or inside the matrix. Cultured cells can selectively remodel or degrade ECM proteins on substrates and integrin dynamics seem to have an important role in this process. Pankov *et al.* demonstrated that the specific translocation of $\alpha_5\beta_1$ integrin from focal

adhesions to fibrillar adhesions drives the formation of the fibronectin matrix [25]. This and many other examples show the importance of cell-surface interactions, particularly integrin-mediated adhesion, in organizing the ECM [26-29].

Cell Migration

Cell migration is essential to many biological processes such as embryogenesis, cell differentiation, wound healing, and immune response [6, 7, 30]. For example, during gastrulation, large groups of cells migrate collectively as sheets to form the resulting embryo. Subsequently cells migrate from various epithelial layers to target locations, where they then differentiate to form the specialized cells that form different tissues and organs. Migration of fibroblasts and vascular endothelial cells repair tissues from a wound. With the inflammatory response, leukocytes from the circulation migrate into the surrounding tissue to destroy invading microorganisms and infected cells and to clear debris. Cell migration also plays important roles in pathological events like tumor cell invasion, metastasis and tumor-induced angiogenesis [31]. In metastasis, tumor cells migrate from the initial tumor site into the circulatory system and onto a new site. The understanding of the fundamental mechanisms and key regulatory molecules underlying cell migration could lead to effective therapeutics for treating disease, cellular transplantation and the preparation of artificial tissues.

In order for cells to migrate and organize tissues successfully, they must not only sense chemical signals in their microenvironment, but also physical cues. How such cellular mechanosensors detect forces, sense the physical properties of substrates and convert them into signals is still unknown. Over previous decades, an enormous research effort has helped with understanding cell migration, including the establishment of polar structures, the

regulation of the dynamic processes of actin and microtubule polymerization, and the regulation of spatial and temporal signal transduction [4-7].

Cells migrate directionally in response to a variety of cues, including gradients of chemokines, growth factors or ECM molecules. Cell migration is an integrated process that requires the continuous, coordinated formation and disassembly of adhesions in spatially distinct locations in the cell [6, 7, 31-33] . In general, cell migration can be considered as a cyclic process. When there is a cue for migration, cells polarize and extend protrusions in the direction of migration. These protrusions can be large and broad lamellipodia or spike-like filopodia. Those are usually driven by actin polymerization and stabilized by adhering to the ECM or adjacent cells *via* transmembrane receptors linked to the actin cytoskeleton. These adhesions serve as traction sites for migration as the cell moves forward over them, and they are disassembled at the rear of the cell allowing it to detach. The details of a cell's migratory behavior can differ greatly depending on its environment and cell type.

Rho family small guanosine triphosphate (GTP)-binding proteins (GTPases) are central regulators of actin organization and they control the formation of lamellipodia and filopodia. The proteins Rac, Cdc42 and RhoG are especially required for protrusion [19, 20, 24, 34, 35]. For migration, a cell must be polarized, which means that the molecular processes at the front and the back of a moving cell are different. Establishing and maintaining cell polarity in response to extracellular stimuli appear to be mediated by a set of interlinked positive feedback loops involving Rho family GTPases, phosphoinositide 3-kinases (PI3Ks), integrins, microtubules, and vesicular transport (Figure 2-3).

Integrins are a major family of migration-promoting receptors. They support adhesion to the ECM or other cells and link with actin filaments on the inside of the cell. Integrins

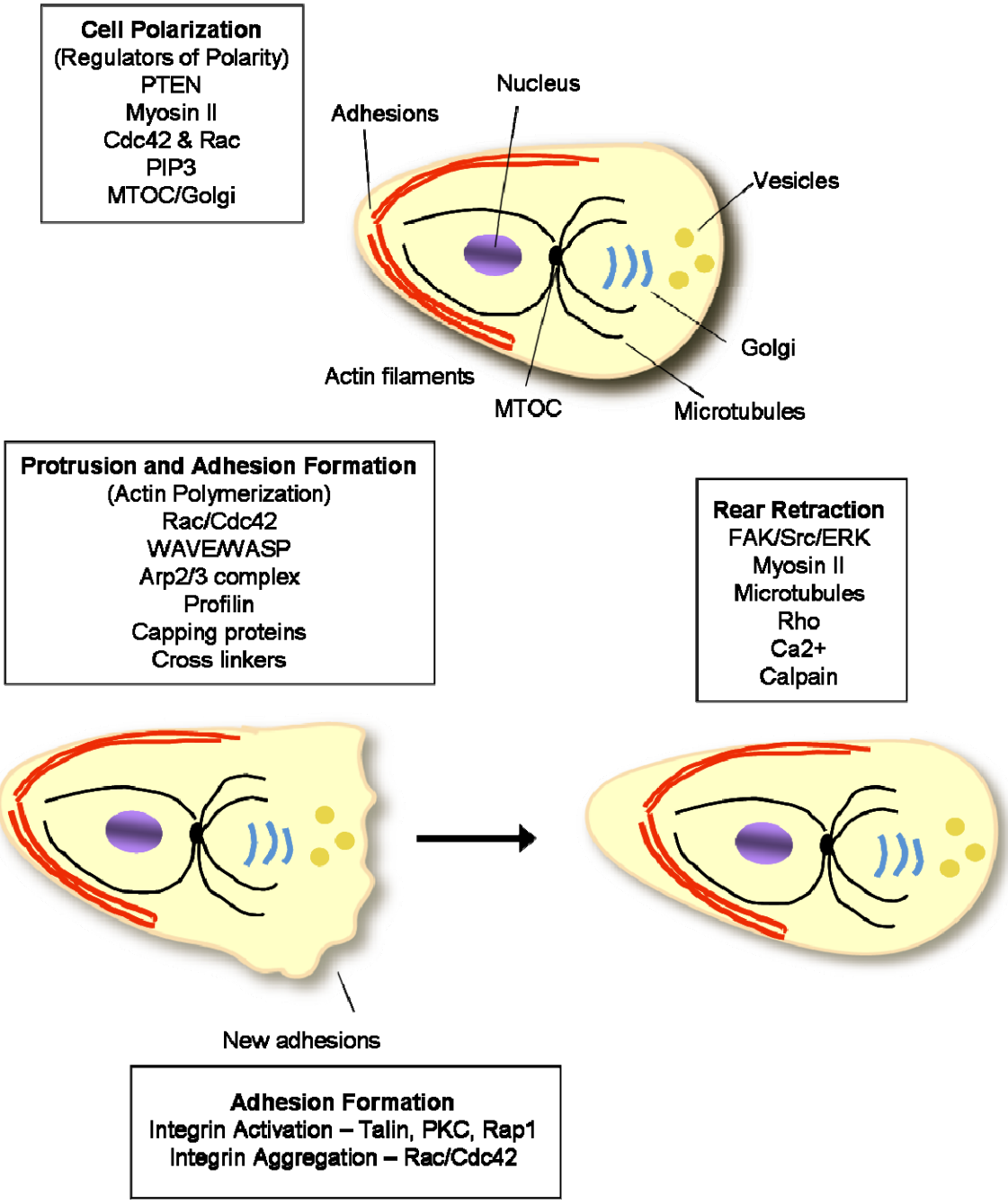

Figure 2-3. Steps in cell migration and the components for regulation of polarity. This figure is adapted and modified from the reference 7.

activate migration-related signaling molecules and also mediate inside-out signaling, that is, activation to a high-affinity state by cytoplasmic signals [4]. The binding of ligands to the extracellular portion of integrins leads to conformational changes in the receptors by changing interactions between the α- and β-chain cytoplasmic domains and to integrin clustering [36]. This combination of occupancy and clustering initiates intracellular signals such as protein tyrosine phosphorylation, activation of small GTPases, and changes in phospholipid biosynthesis that regulate the formation and strengthening of adhesion sites, the organization and dynamics of the cytoskeleton, and cell polarity during migration. Although integrins themselves do not have any catalytic activity, signals are transmitted through direct and indirect interactions with many partners of integrins.

The migration is initiated with a cascade of events, including the activation of G proteins or tyrosine kinases, the stimulation of guanine nucleotide exchange factors (GEFs) for Cdc42, and the activation of lipid kinases and the subsequent recruitment of activated Rac. The local activation of Rac and/or Cdc42, in concert with other regulators such as WASP/WAVE family proteins and the Arp2/3 complex, stimulates the formation of a branching actin filament network at the leading edge, which in turn induces a protrusion in the direction of migration. Localized activation of Cdc42 and Rac decreases Rho activity and enhances PI3K activity and the production of $PI(3,4)P_2/PIP_3$ at the leading edge [37, 38]. Cdc42 influences polarity by restricting where lamellipodia form and localizing the microtubule-organizing center (MTOC) and Golgi apparatus in front of the nucleus, oriented toward the leading edge. Integrins and other adhesion molecules are activated by PI3Ks, PKCs, and/or Rap *via* talin, and they stabilize the protrusion *via* structural connections to the actin filaments [39]. They also signal to Rac, which promotes recruitment of additional

integrins and the formation of adhesions. New adhesions at the leading edge in turn reinforce high Rac, Cdc42 and PI3K activity. The activity of Rho is low at the leading edge and higher at the rear and sides. Adhesions transmit propulsive forces and serve as traction points over which the cell moves. The migration cycle is completed as adhesions disassemble and the rear retracts. The disassembly of adhesions is controlled by pathways that include FAK, ERK, Src, and the protease calpain, as well as microtubule dynamics [40]. Retraction at the rear requires Rho kinase and is a myosin-dependent process.

Although our understanding of cell migration in the molecular basis has progressed there are still many unresolved issues regarding how cells establish and maintain their polarity, how cells migrate *in vivo*, how cells recognize their targets, and how the spatially distant component processes are integrated temporally and spatially across the cell [41]. To answer those questions, developing novel models that can present, quantify and perturb localized signals will be necessary.

Fibronectin Mimics - RGD and PHSRN

Fibronectin (FN) is a dimeric glycoprotein composed of disulfide-linked subunits with a molecular weight of 220–250 kDa each [42]. Being present at high concentrations (~300 μg/mL) in plasma, FN interacts with collagen, heparin, fibrin as well as integrin family and has been shown to be involved in cell adhesion, cell morphology, thrombosis, cell migration and embryonic differentiation [11, 43].

Since the peptide sequence Arg-Gly-Asp (RGD) was discovered in FN as a minimal adhesion sequence by Pierschbacher and Ruoslahti in 1984 [44], the tripeptide sequence has been universally used in many studies regarding to cell adhesion and migration [45, 46].

Numerous materials have been RGD-functionalized to promote cell adhesion [47-50] and soluble, small RGD-based peptides which block integrin signaling are studied for therapeutic purposes as inhibitors of tumor growth, angiogenesis and metastasis and as platelet-inhibitory drugs [51-54]. The RGD sequence is also commonly shared by many adhesive proteins in the ECM and in the blood including vitronectin, osteopontin, collagens, thrombospondin, fibrinogen, and the von Willebrand factor [45].

The RGD motif is located in the 10th type III repeating unit of FN (FNIII10) and many cell types binds to the specific central cell binding domain of FN spanning from the 8th to the 10th type III domain. However, other data indicate that an additional synergistic subregion, the FNIII9 domain, is required for full adhesive activity for the $\alpha_5\beta_1$ and $\alpha_{IIb}\beta_3$ mediated cell adhesion [55, 56]. The peptide sequence Pro-His-Ser-Arg-Asn (PHSRN) was identified as a minimum synergistic sequence enhancing cell adhesion and spreading. However PHSRN alone cannot support cell adhesion [57, 58]. RGD and PHSRN are separated by 30 - 40 Å and placed on the same surface of FN by a small rotation of a flexible linkage connecting the 9th and 10th type III domain [59].

Cell cultures on different types of surfaces (e.g. glass, polymer film, SAM and tissue culture plate) which were adsorbed with FN suggest that many biological phenotypes such as focal adhesion assembly, cell adhesion, cell differentiation, gene expression, migration and apoptosis can be affected by the chemical functional groups or hydrophobicity of the surface [60-65]. There is evidence that the different surface properties lead changes in integrin specificities toward FN and thus changes in the biological activities of cells [60, 66]. Although it is unclear what conformational change FN undergoes, Garcia *et al.* suggested that changes in the orientation and the distance of the linkage between the 9th and 10th type III

domain of the FN central cell binding domain might be an important factor to determine such integrin specificities against FN on different surfaces [66]. Some recent studies have noticed the structural basis of FN domains and created model molecules with RGD and PHSRN sequences to clarify their roles in cell adhesion [67-71].

Design Rationale for Model Substrate

In order to elucidate the spatial and temporal mechanisms of these complex processes on a molecular basis, model substrates that can dynamically modulate the interaction between cell and material at the molecular level would be extremely useful [72, 73]. Herein, we develop a novel surface chemistry technology to generate a class of molecularly well-defined dynamic substrates that permit the precise modulation of the environment that an adherent cell senses in space and time. We demonstrate this methodology by electrically switching on adhesive ligands that induce the migration and growth of cells, which were initially confined on the defined patterns. We determine how the interplay of several parameters including the population of cells, pattern geometry, ligand density, ligand affinity and integrin composition influence cell behavior on these dynamic surfaces. We also found that cells retain an imprint of their initial condition, which influences the subsequent migratory behavior as if cells have a memory of the earlier environment. Genome-wide microarray analysis revealed that several genes in signal transduction, cytoskeletal reorganization and proliferation are differentially regulated at the transcription level depending on the dynamic surface microenvironment.

To prepare surfaces for the dynamic study of complex cell behavior we designed model substrates based on the following considerations: 1. the surface must be able to present

ligands in a well-defined environment and must be amenable to chemoselective reactions that immobilize ligands or transformations that reveal ligands to adherent cells during the course of cell migration or cell adhesion. This important feature requires an orthogonal chemical reaction to immobilize ligands to a surface in the presence of cells and complex protein mixtures with no side reactions. The immobilization reaction should be fast, kinetically well-behaved, and unreactive toward other biopolymers (DNA, RNA, proteins, lipids etc.) at physiological conditions; 2. the yield of immobilization reaction and therefore density of immobilized ligands on the surface must be precisely determined. This requires that the model substrates are compatible with sensitive and quantitative *in situ* surface analytical techniques; 3. the surface should have the ability to pattern different population of cells in defined geometries ranging from a single cell to hundreds of cells; 4. a non-invasive method that can activate the surface by immobilizing or unveiling ligands in the presence of attached cells is required; 5. the surface must be inert to non-specific protein adsorption, i.e. the only interaction between cell and material is a ligand-receptor mediated interaction; 6. the model substrate should be compatible with high throughput microarray technologies and several surface and microscopy techniques that are routinely used to characterize cell behavior, and ;7. The surface should possess the ability to perform massively parallel experiments simultaneously.

Our approach for the dynamic substrate is based on an electrically switchable self-assembled monolayer (SAM) that presents redox active hydroquinone groups (Figure 2-4A). The substrate is essentially a working electrode that can oxidize and reduce the surface-bound molecules upon an applied potential. A mild electrochemical pulse readily converts the hydroquinone monolayer to the corresponding reactive quinone. The reversible redox

coupling between the hydroquinone and the quinone is stable and can be characterized by cyclic voltammetry [74, 75]. We have previously demonstrated that the resulting quinone monolayer can react rapidly and selectively with soluble oxyamine groups to form a chemically stable oxime conjugate on the surface [76]. By synthetically tethering ligands to the oxyamine, this methodology can potentially immobilize a variety of ligands such as peptides, carbohydrates, and other biomolecules to the surface. Furthermore, because the oxime conjugate undergoes redox coupling at different potentials from the quinone, the product possesses diagnostic waves that can be characterized electrochemically by cyclic voltammetry [76-78]. This feature permits the quantitative determination of yield and therefore density of ligand immobilized on the surface *in situ*. Most importantly, the highly selective coupling between the quinone and oxyamine prevents cross reaction with other biomolecules including DNA, proteins, carbohydrates, and lipids. This coupling strategy therefore is ideal for bioconjugation in the presence of complex protein mixtures and in the presence of adhered cells in serum-containing media.

Table 2-1. Characteristic features of different types of cell-matrix adhesions (adapted from reference 4)

Property/structure	Focal complexes	Focal adhesions	Fibrillar adhesions
Location	Edge of lamellipodium	Cell periphery	Central region of cells
Morphology	Dot-like	Elongated, oval	Fibrillar or beaded
Size (long axis)	1 μm	2 – 5 μm	Variable (1 – 10 μm)
Typical constituents	Paxillin Vinculin Tyrosine-phosphorylated proteins	α_v integrin Paxillin Vinculin α-actinin Talin Focal adhesion kinase Tyrosine-phosphorylated proteins	α_5 integrin Tensin
Induced by	Rac	Rho	Rho (?)

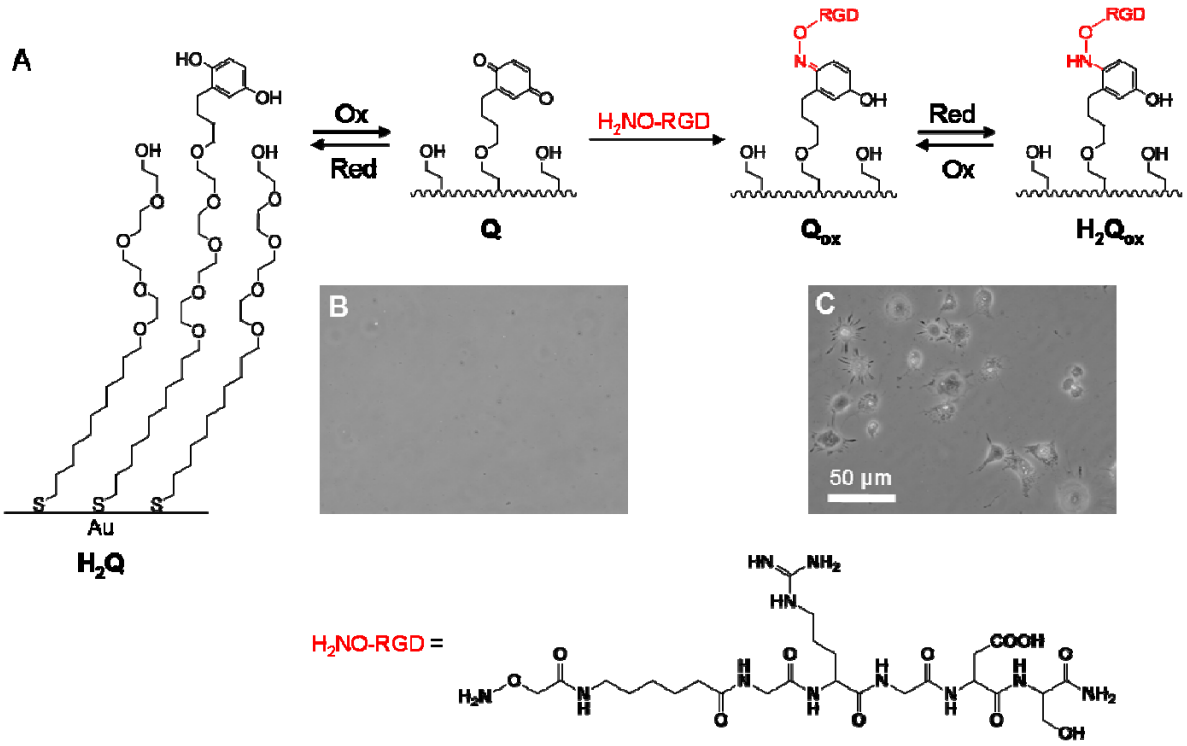

Figure 2-4. A chemical strategy for immobilization of ligand (RGD) for cell adhesion. A. A surface presenting redox active hydroquinone groups (H_2Q) is oxidized to the corresponding quinone (Q) by applying an electrochemical potential to the underlying gold. Reaction of the quinone monolayer with soluble RGD-oxyamine at physiological conditions generated the peptide oxime conjugate on the surface. The oxime conjugate Q_{ox} is also electroactive and can undergo a reversible redox process resulting in the H_2Q_{ox}. The chemical structure of RGD-oxyamine is shown below. B. The quinone monolayer, Q, is inert to the non-specific attachment of cells. C. Addition of 3T3-Swiss albino fibroblasts to the RGD immobilized oxime surfaces resulted in cell attachment and proliferation.

Results and Discussion

Ligand Immobilization for Cell Attachment

To determine whether the electroactive surface can support biospecific cell attachment *via* the oxyamine ligand immobilization strategy, we prepared mixed monolayer surfaces presenting 1 % hydroquinone and 99 % tetra(ethylene glycol) groups. The high density of background ethylene glycol groups within the monolayer has been shown to reduce non-specific protein adsorption [79]. This feature ensures that the cell-surface interaction is mediated only by the cell surface receptors and ligands on the surface. Electrochemical oxidation of the monolayer (750 mV for 10 seconds) converts the hydroquinone groups to the reactive quinones (Figure 2-4A). Addition of 3T3-Swiss albino fibroblasts to the resulting quinone monolayer showed no cell attachment to the surface (Figure 2-4B). This result demonstrates that the surface resists non-specific cell attachment and that electrochemical oxidation does not compromise the integrity of the monolayer. To facilitate cell adhesion an oxyamine-tethered RGD peptide (structures in Figure 2-4) was synthesized and conjugated to the quinone monolayer (20 mM in PBS, 4 hours). Addition of fibroblasts resulted in attachment and proliferation on the RGD-immobilized surface (Figure 2-4C). To show the attachment was specific we added soluble RGD peptide (final concentration of 1 mM, 1 hour) as a competitive inhibitor of the surface-bound RGD and the adherent fibroblasts detached from the surface (data not shown). Furthermore, as a control experiment a scrambled peptide (GRD-oxyamine) was immobilized to the quinone monolayer and no attachment of cells to the surface was observed (data not shown). These results confirm that cell attachment to the monolayer surface was mediated only by the immobilized RGD ligands.

Dynamic Surfaces for Biospecific Cell Migration

The method for ligand immobilization onto the SAM surface *via* oxime formation was applied to generate dynamic model substrates for studies of cell migration. We used microcontact printing to first pattern hexadecanethiolate monolayers on the surface. Microcontact printing is a method for patterning SAMs on surfaces (Figure 2-5). SAMs form in the regions of contact between a topographically patterned elastomeric stamp, which is wetted with chemical ink consisting of n-alkanethiols, and the bare surface of gold. Then the remaining bare gold regions were backfilled with a mixed monolayer of 1 % hydroquinone and 99 % tetra(ethylene glycol) groups (Figure 2-6A). The hydrophobic patterns were then adsorbed with fibronectin (0.1 mg/mL in PBS, 2 hours) to enhance cell attachment. Addition of fibroblasts to the surface resulted in cell attachment only to the microcontact printed regions. Observation by live-cell microscopy showed that while most cells are quiescent within the patterns, the cells near the edge of the patterns are highly dynamic. The patterned cells constantly sample the surface microenvironment outside the pattern *via* filopodia and lamellipodia protrusions and membrane ruffling. Electrochemical activation converted the hydroquinone monolayer to the quinone, followed by immobilization of linear RGD-oxyamine (20 mM in serum-free medium, 2 hours) to install the peptide ligands to the monolayer. The short electrochemical pulse applied (750 mV, 5 seconds) to oxidize the hydroquinone groups and the addition of the soluble oxyamine-functionalized RGD peptide does not affect cell viability. The surface microenvironment surrounding the cell patterns is switched from being inert to adhesive with surface-immobilized RGD ligands. As a result, cells confined within the confluent patterned region initiated migration in response to the changes in the surface microenvironment.

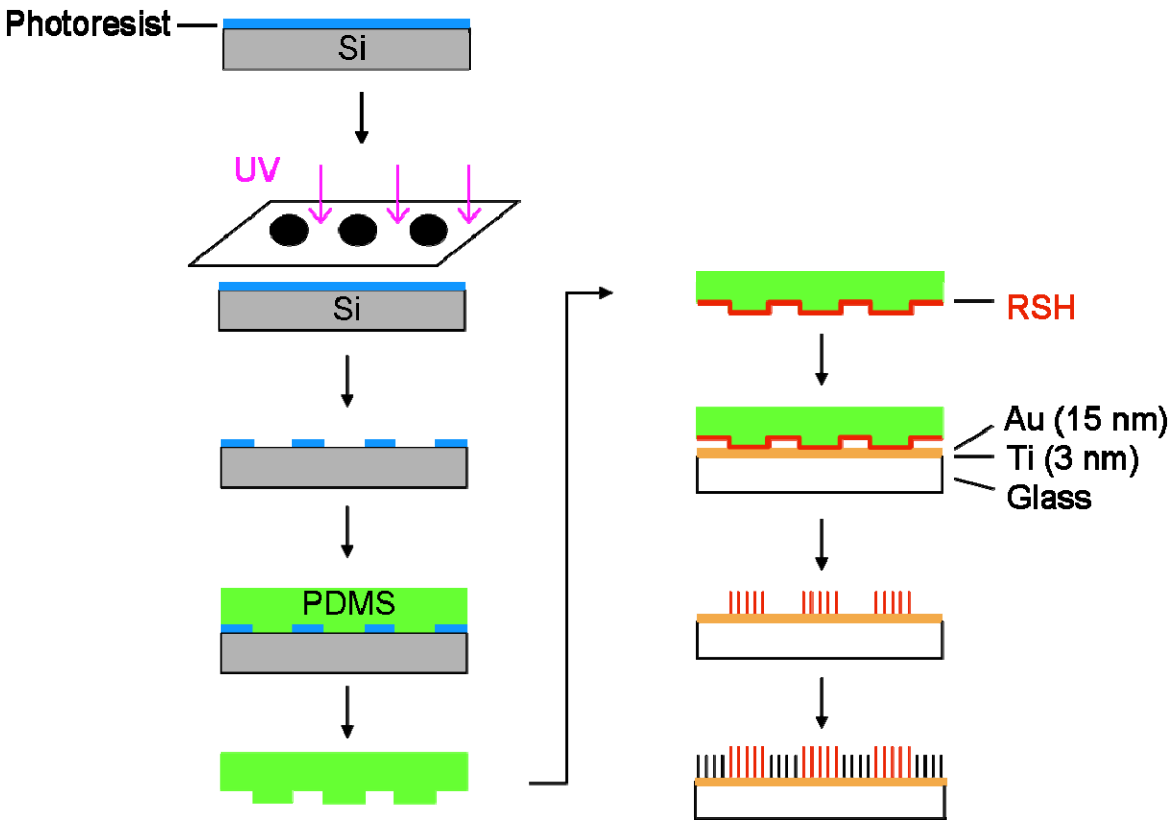

Figure 2-5. Microcontact printing. Microcontact printing is a soft lithography method for patterning SAMs on surfaces. Patterned photoresist serves as a master to generate an elastomeric stamp (PDMS). Alkanethiol-wetted stamp transferred the thiol to the bare gold by physical contact and SAMs are formed in the regions of contact.

Figure 2-6B shows representative fluorescent images for ligand-mediated migration of patterned cells over time on three different sizes of circular pattern (160 μm, 110 μm, and 60 μm in diameter). After 2-3 hours of linear RGD immobilization, cells begin to protrude and move beyond the edge of the pattern, and after 10 hours the cells have moved a significant distance away from the initial circular patterns. Despite the different sizes of the initial patterns, all the cells continued to migrate and after 30 hours of RGD immobilization it was difficult to define the original pattern. As a control, the exact same substrates without the RGD immobilizing reaction were prepared. There was no migration and the cells stayed confined within the circular patterns even after 48 hours in the incubator (Figure 2-6C). As a further control to show the migration was due to the biospecific interaction between integrin receptors on the cell and the newly immobilized RGD ligands, soluble RGD was added into the cell medium (final concentration of 0.7 mM for 1 hour) and the cells detached from the RGD presenting regions but not from the hydrophobic fibronectin islands (data not shown). When a scrambled peptide (GRD-oxyamine) was immobilized under the same conditions (this peptide is not a ligand for integrin receptors) the cells were observed over 48 hours not to migrate from the patterns (Figure 2-6D). Therefore the dynamic presentation of ligands on the surface in the presence of the cells functioned as a molecular switch to turn on cell migration.

Unlike many conventional migration assays including wound healing assays [80, 81], Boyden chamber [82], and other methods [83-86] where cells migrate on ill-defined substrates, our dynamic substrate approach is mediated by the underlying surface chemistry where the ligand presentation, density, activity, and composition is defined at the molecular level. These features allow for the proper control and interpretation of cell behavior on

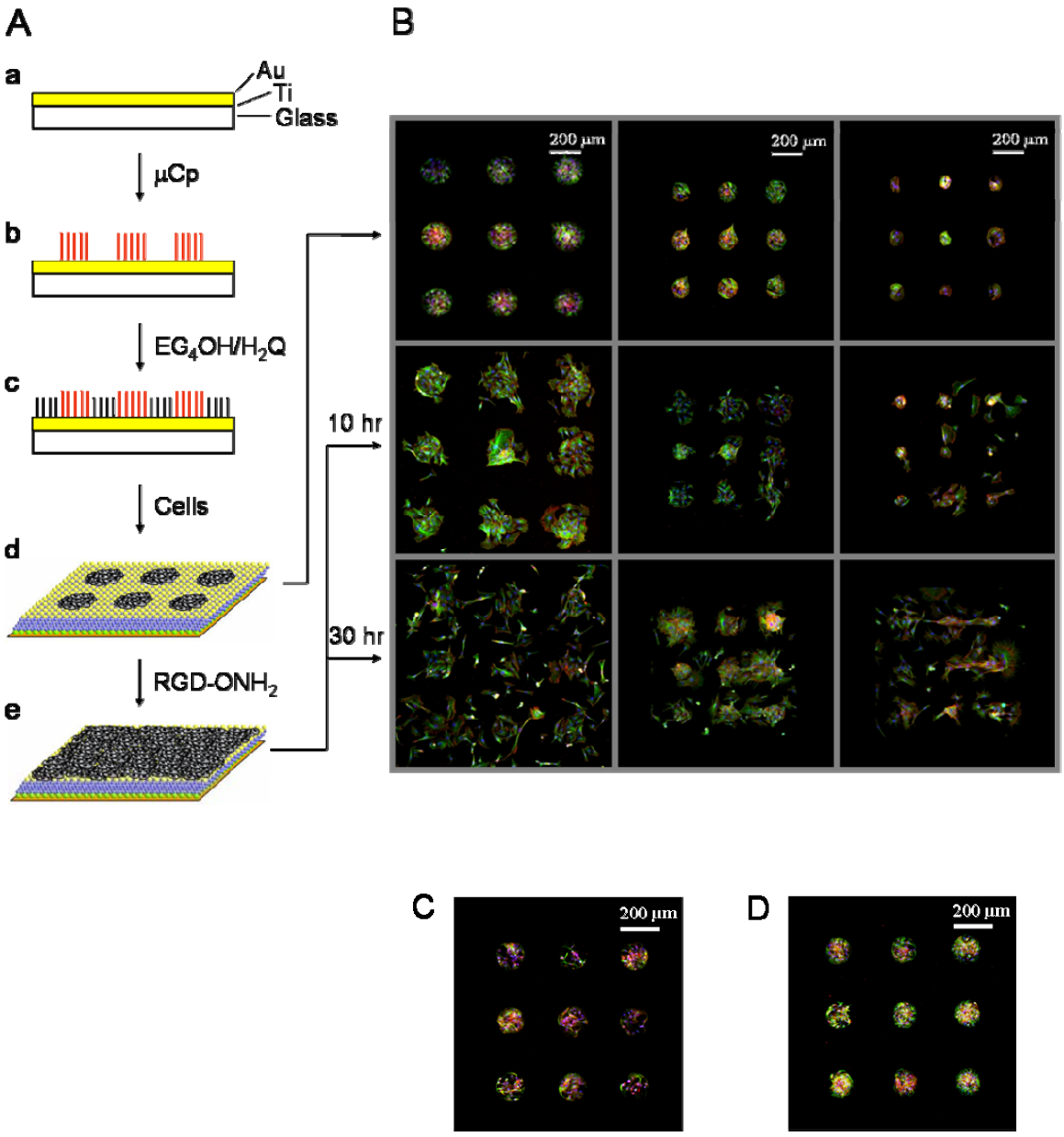
A
B
a
Au
Ti
Glass
μCp
b
EG4OH/H2Q
c
Cells
d
RGD-ONH2
e
10 hr
30 hr
200 μm
C
D

Figure 2-6. Example of a dynamic substrate for spatial and temporal control of cell migration and growth. A. (a) Surfaces compatible with cell imaging were prepared by evaporating titanium and then gold onto glass coverslips. (b) Microcontact printing was used to pattern hydrophobic islands of hexadecanethiol. (c) The remaining bare gold regions were filled with a mixed monolayer of tetra(ethylene glycol) (EG_4OH) and hydroquinone (H_2Q) terminated alkanethiol. (d) The patterned hydrophobic area was adsorbed by fibronectin and fibroblasts attached, proliferated and remained confined to the patterned regions. (e) Application of oxidative potential to the monolayer and subsequent addition of oxyamine-RGD (20 mM, 2 hours) resulted in the rapid immobilization of peptide and hence the migration and proliferation of cells off of the circular islands. B. Representative figures from fluorescence microscopy over the period of time with three different sizes of circular patterns. The diameters of the pattern are 160 μm, 110 μm, and 60 μm, respectively. In all three sizes of the patterns, upon ligand presentation cells gradually migrated out and broke down the patterns completely within 30 hours after RGD immobilization. C and D. The cells on substrates with no RGD (C) or scrambled peptide (GRD) immobilization (D) do not migrate. Color: green, tubulin; red, actin filaments; blue, nuclei.

tailored biospecific ligand-receptor mediated surfaces. Furthermore, because these substrates modulate the surface property in the presence of attached cell culture, it is possible to monitor cell behavior in response to various changes in the surface microenvironment in real-time.

The Role of Cell Population and Pattern Shape on Cell Migration and Growth

Using the dynamic substrates it was determined how the number of cells and initial pattern shape affect motility and growth. We used a nuclear labeling index (NLI) assay, which measures the amount of DNA synthesis occurring within adhered cells undergoing growth, to compare the role of pattern size and geometry on cell migration and cell growth. Dynamic substrates were prepared as described above and upon activation of the surface by immobilizing linear RGD, cells were allowed to migrate from the patterns for 20 hours and then 5-bromo-2'-deoxyuridine (BrdU, a thymidine analog that incorporates into newly synthesized DNA) was added in the cell culture medium (10 μM) for one hour to allow pulse-labeling of DNA. The cells were then fixed and the BrdU-labeled nuclei were detected *via* anti-bromodeoxyuridine and a Cy2-conjugated secondary antibody. Whole cell nuclei were also stained with DAPI and the results were visualized with fluorescence microscopy. To interpret the migration distance as a function of initial pattern geometry and size of the patterns, we defined areas by drawing circles or lines proportionally to the initial pattern radius or width to keep track of the cells according to the distance migrated (Figure 2-7 top and middle panel). The total number of nuclei and BrdU-labeled nuclei were counted in each area. The percentage of the newly synthesized nuclei (DNA) was calculated to give a NLI (ratio of BrdU-labeled nuclei to total nuclei). The bar graphs in Figure 2-7 show the NLI

according to the migration distance. For the analysis, it was assumed that cells initiated migration from the boundary edge of the pattern and the cells found within the interior of the patterned area had no migration upon surface activation. In the bar graphs of Figure 2-7A-C, the first sets of data (distance 0 μm) represent the NLI of the cells within the initial pattern. These cells are considered as having no migration, and therefore their NLI is set as the basal level of new DNA synthesis in non-migratory, contact inhibited quiescent cells. The bar colors of the data set for each distance traversed corresponds to the regional zones of the same color in the pattern diagram above. Figure 2-7A and 2-7B compare the role of cell population in cell migration and growth by analyzing the NLI for small and large size of circular patterns that restrict the initial population of the cells. We also compare the effect of pattern geometry (circle versus straight line) on cell migration and growth (Figure 2-7C).

The comparison of NLI in relation to migration distance is a measurement to visualize the relative balance between migration and growth activity. We found that regardless of pattern size or shape the cells that migrated farther from the initial pattern had higher rate of new DNA synthesis (higher NLI). The cells that migrated the farthest were found to be the cells initially located at the edge of the pattern. Upon surface activation, these cells have greater access to free space that supports adhesion and migration and therefore are able to *turn on* their cell growth program before the cells originally located near the crowded center of the pattern do. These results may be also influenced by cell-cell interactions during cell movement. To control the cell number and therefore population of cells we generated different sizes of patterns to determine how the initial cell population influences subsequent cell migration and growth after surface activation. Interestingly, it was observed that cells within the small and large circular patterns had similar basal levels of DNA synthesizing

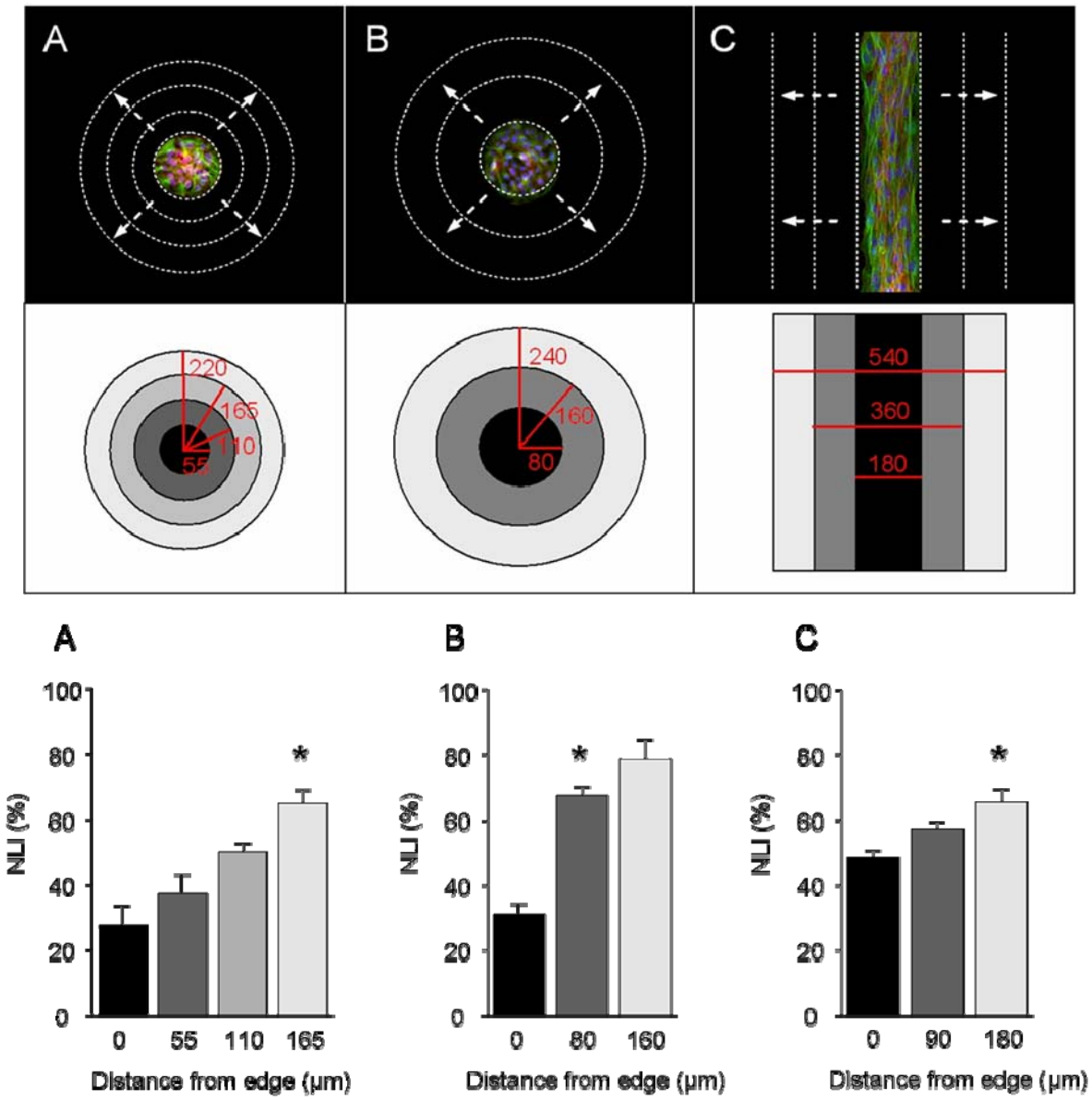

Figure 2-7. Example of cell migration and growth dependence on geometry and population of cells. The migrating cells on the dynamic substrates were treated with BrdU to identify proliferating cells. The NLI implies that actively migrating cells have higher growth rate. See the discussion for details. Data are collected from 6 to 8 separate substrate chips each in (A), (B) and (C). Data are mean ± SEM.

activity (27.5 % and 31.2 %, respectively) (Figure 2-7A and 2-7B). After surface activation, the cells which migrated approximately 165 μm (off small) and 80 μm (off large) circular patterns at the time point of 20 hours had similar levels of NLI (see the *-noted bar graphs with NLI of approximately 65 %). These results show that for the same time period and growth rate (i.e. same NLI) cells from the small pattern (less cell population) migrated farther than cells from the larger population pattern. This result implies that there may be less cell-cell interactions in the smaller population patterns after surface activation and therefore the cells may migrate with less constraint where the dominating factor for migration is the number of cell-ligand interactions rather than the number of cell-cell interactions.

For the cells initially confined within line patterns, we also observed that the farther the cells migrate the higher the growth rates (Figure 2-7C). We found that the basal level of DNA synthesis within the line patterns was much higher (48.4 %) than for the circular patterns. Interestingly, the comparison between circular and line patterns (Figure 2-7A and 2-6C) showed a different trend for migration and growth. Within 20 hours, cells with approximately NLI 65 % were found to migrate a distance of 180 μm from the large population line patterns which is similar to the distance cells travelled from the small population circular patterns. Although the cells migrate approximately the same distance and have similar NLI after 20 hours the cells on the line patterns took longer to initiate migration. For example, many cells on circular patterns have already migrated a significant distance within 10 hours after RGD immobilization on the surface while most cells on line patterns are not observed to migrate. This indicates the degree of curvature of the pattern where cells are originally confined can have a dramatic impact on the ability of cells to initiate migration and growth. On the straight line pattern the cells are densely packed parallel to the edge of

the pattern and upon surface activation the cells at the edge must move out perpendicular to their alignment. This may require a massive rearrangement of the cell cytoskeleton and therefore it takes much longer to initiate migration compared to the cells on small circular patterns that are not restricted by geometry. However, after moving beyond the line patterns the cells are able to migrate with limited cell-cell interactions compared to the circular patterns where several cells are joined during migration. Therefore the comparable migration distance with the similar level of NLI in Figure 2-7A and 7C (*-noted bar graphs) appears to be influenced more significantly by the initial geometry. Overall the NLI measurements show that the actively migrating cells generally have a higher growth rate and there is a delicate interplay of cell-cell interactions, cell-substrate interactions and initial geometry in dictating subsequent migration and proliferation.

The Role of Integrin Composition on Cell Migration

The role of integrin composition on cell migration and growth on the dynamic surfaces was studied. We compared the rate of migration and growth for several Chinese Hamster Ovary (CHO) cell lines where the cytoplasmic α5 subunit of the $\alpha_5\beta_1$ integrin, a fibronectin receptor, has been either deleted or truncated. Three mutant CHO cell lines were examined: B2a27 expresses a full-length of human α5 subunit with 27 amino acids in the cytoplasmic domain; B2a10 expresses an α5 with a 17 amino acid cytoplasmic truncation; and B2 expresses only the β1 subunit where the α5 is knocked down. In previous research Bauer *et al*. used these cell lines to examine the role of α5 cytoplasmic domain in cell adhesion, cell motility and cytoskeletal organization [87]. On fibronectin-coated surface they found B2a27

and B2a10 displayed similar adhesion, motility and actin organization to wild type CHO cells while the untransfected B2 cells showed no migration and no actin reorganization.

To test whether these mutant cells behave in a similar manner on our molecularly defined surface, the same experimental procedure as in Figure 2-7B was performed with the three CHO cell lines. We found that both B2a27 and B2a10 cells patterned on 160 μm diameter circles migrated and proliferated to a similar extent as the 3T3-Swiss albino fibroblasts did upon activation on 1 % linear RGD-immobilized surface (Figure 2-8). In contrast, although untransfected B2 cells adhered to the initial pattern, they did not migrate when the surface was activated with linear RGD ligands. Thus, the truncated α5 cytoplasmic domain is not essential for cell motility but the extracellular domain and the cytoplasmic domain adjacent to the membrane may have important functions in cell migration. This cell motility and growth data is consistent with the results obtained from the fibronectin-coated surfaces [87]. Taken together, these results demonstrate dynamic surfaces are well-suited for evaluating the dependence of cell growth and migration on integrin composition and expression levels.

On Non-Dynamic Surfaces Cell Migration Rate Depends on Ligand Affinity and Density

To understand the role of ligand density and affinity in directing cell migration a series of studies was performed where cell migration rates were monitored on surfaces presenting different densities and affinities of RGD ligands. Integrin receptors are known to have higher affinity to cyclic RGD than linear RGD (IC_{50}[cyclic RGD] / IC_{50}[linear RGD] ≈ 10^{-3}) [88, 89]. To modulate the ligand affinity on the surface, oxyamine-functionalized linear RGD and cyclic RGD was used. For these studies SAMs were prepared as mixed monolayers

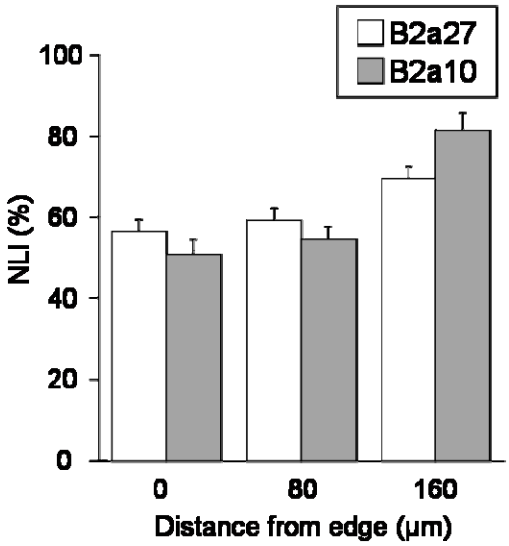

Figure 2-8. Growth versus migrating distance for integrin α subunit mutants of CHO cells on dynamic surfaces. Data are mean ± SEM and more than 6 separate substrate chips for each cell line were used for the analysis.

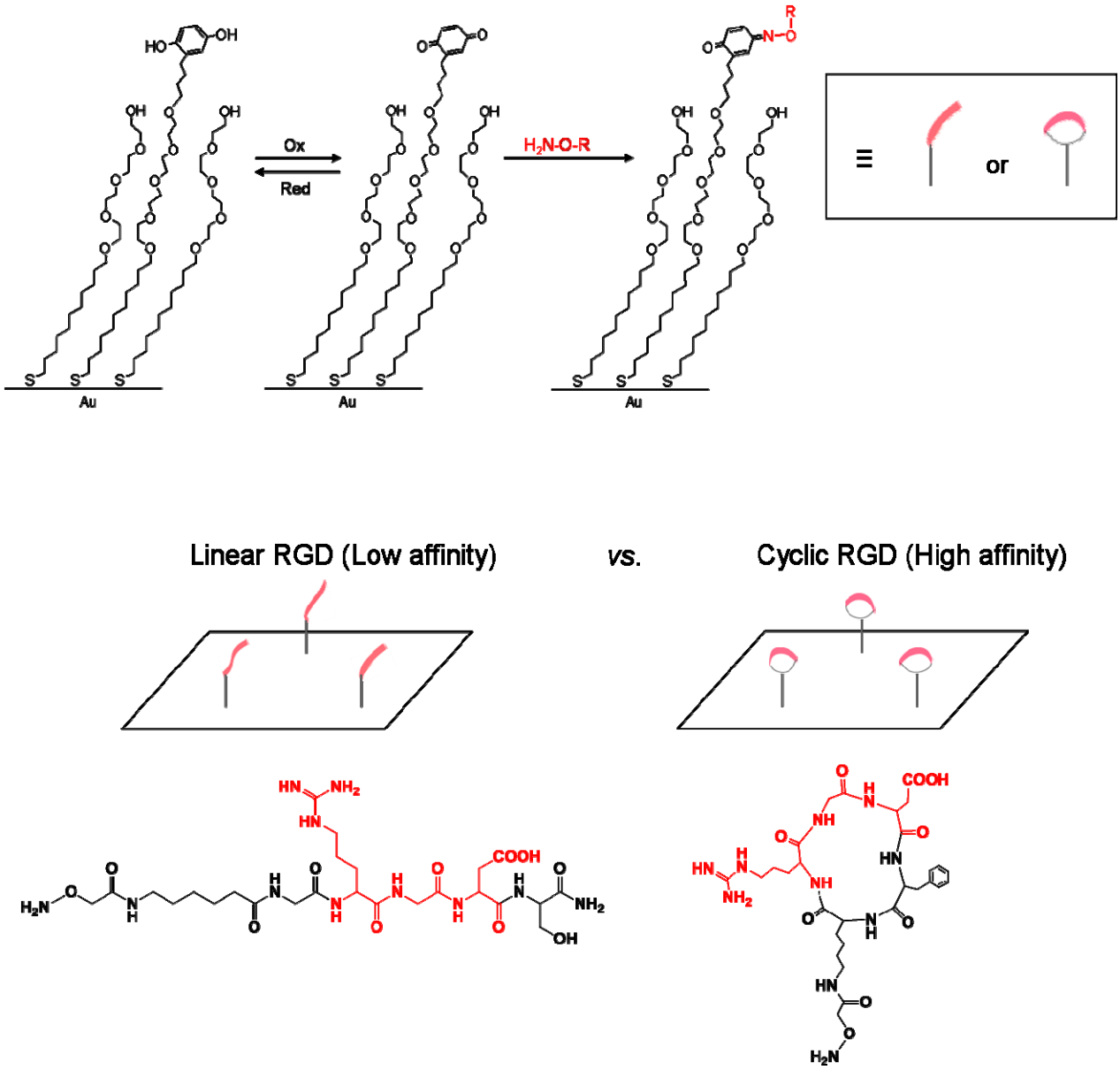

Figure 2-9. Non-dynamic SAM surface presenting linear and cyclic RGD. Mixed SAM presenting hydroquinone and tetra(ethylene glycol) groups was prepared on gold. Upon electrochemical oxidation to quinone, linear or cyclic RGD was immobilized as an oxime adduct. Linear RGD presenting surface has low affinity to integrins while cyclic RGD surface has higher affinity. The structures of linear and cyclic RGD are shown with the "RGD" sequence in red.

presenting hydroquinone (from 1 % to 10 %) and tetra(ethylene glycol) (99 % to 90 %) groups on gold.

Upon electrochemical oxidation to quinone, linear RGD or cyclic RGD was immobilized. The Figure 2-9 shows the scheme of this experiment and the structures of linear and cyclic RGD. The completion of the coupling reaction was determined by cyclic voltammetry. Each substrate was rinsed with water and 3T3-Swiss albino cells were then seeded to determine migration velocity as a function of peptide density. This type of substrates is termed as a "non-dynamic surface" since there is no patterned region of cells and the entire surface is composed of peptide ligands prior to cell seeding. Time-lapse images were recorded and the movement of the cells was tracked.

Figure 2-10 shows some representative cell images from the time-lapse movie. The cells on linear RGD surface were often found in different locations from the original attachment sites while the cells on the cyclic RGD surface were not motile. Figure 2-11 compares cell velocity on the surfaces with different density and ligand affinity. For the non-dynamic high affinity cyclic RGD surfaces, the attached cells rarely migrate and there is no substantial difference in cell migration rate from 1 to 8 % ligand density. This reflects that the polyvalent adhesive interaction between integrin receptors and cyclic RGD ligands is too strong even at low densities to allow significant cell motility. However for low affinity linear RGD surfaces, we observed a biphasic behavior where cell migration velocities increased up to 5 % ligand density and then decreased from 6 % to 8 %. The biphasic cell migration rate data show that at low ligand density (1 - 5 %) cells are able to attach and release integrin receptors from the surface and migrate with increasing velocity but at higher ligand densities

(> 5 %) the adhesiveness of the surface overcomes the ability for the integrin receptors to detach and therefore the migration is not effective.

Additionally, a mixture of linear and cyclic RGD peptides (1:1 ratio) was immobilized on the surface and cell movements were recorded. Interestingly, for the mixture RGD surface the migration rates were faster at lower density and exhibited an earlier biphasic behavior than for the linear RGD surfaces. From this study a mixture RGD surface allows the greatest cell motility at 1 - 2 % ligand density and at higher densities the effect of the cyclic RGD predominates and causes motility to significantly decrease.

Why cells migrate with higher velocity on the mixture RGD surface than on the linear RGD surface at < 2 % ligand density is intriguing. It may be because cells possess the ability to modulate the combinatorial variability of the affinity states of the integrin receptors for complex ligands. Previous work has shown a biphasic migration rate on fibronectin-coated surfaces depending on the concentration of the fibronectin solution used [90]. However, these surfaces are unable to define the ligand orientation and the actual ligand density on the surface because they rely on non-specific fibronectin adsorption. Because our surface is based on molecularly well-defined ligand coupling and presentation, it is ideal to study the influence of ligand concentration and affinity on cell motility. The results presented here are significant because there have been no studies of cell motility on different affinity and mixed affinity peptide presenting surfaces.

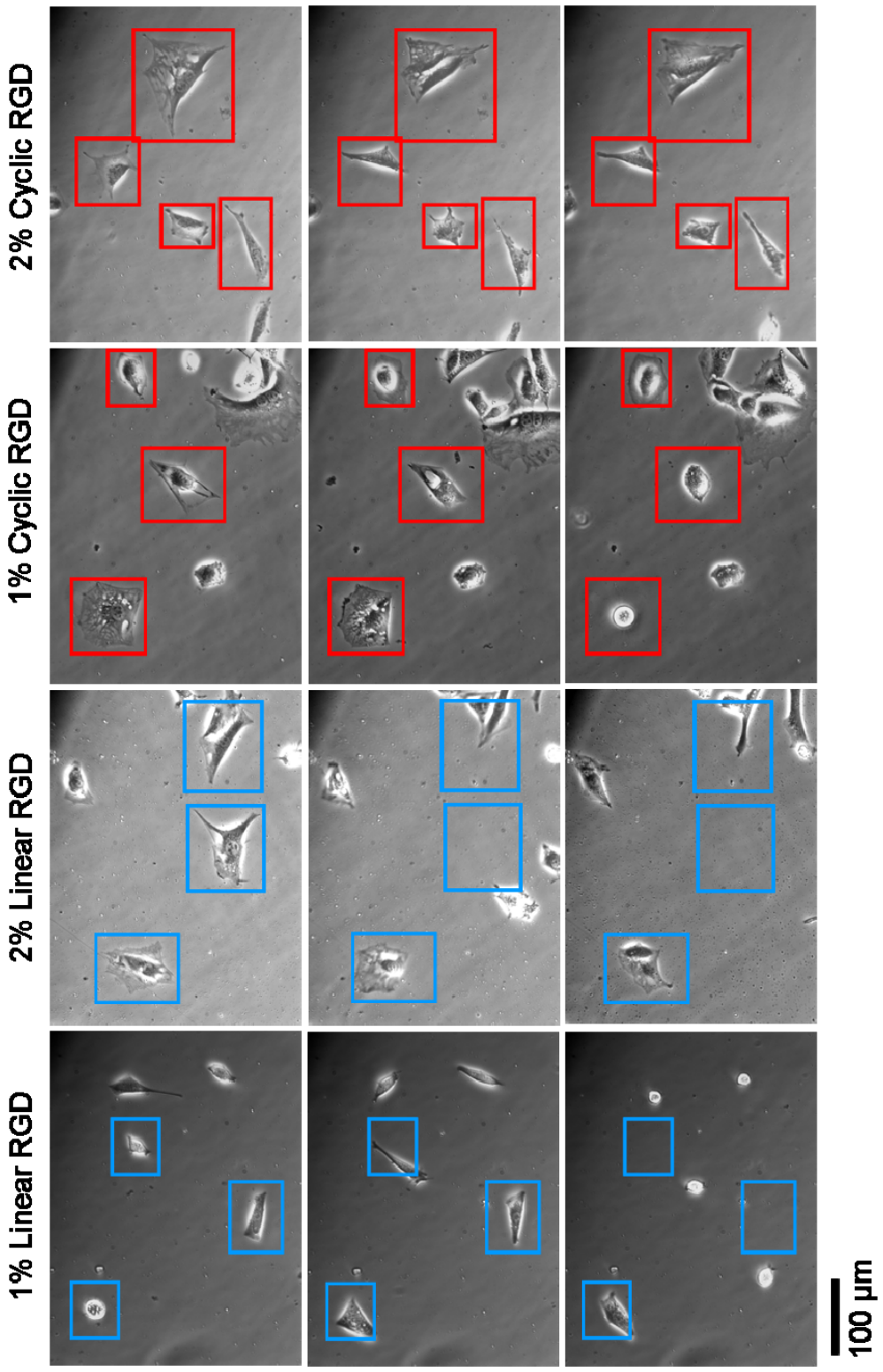
1% Linear RGD
2% Linear RGD
1% Cyclic RGD
2% Cyclic RGD
0 hr
10 hr
20 hr
100 µm

Figure 2-10. The images of cells from the non-dynamic surfaces. Cell movements on 1 % and 2 % linear/cyclic RGD surfaces over 24 hours were recorded as time-lapse movie. The images at 0, 10 and 20 hr are shown here. The blue- and red-colored boxes were drawn to designate the original location where the cell was attached at 0 hr.

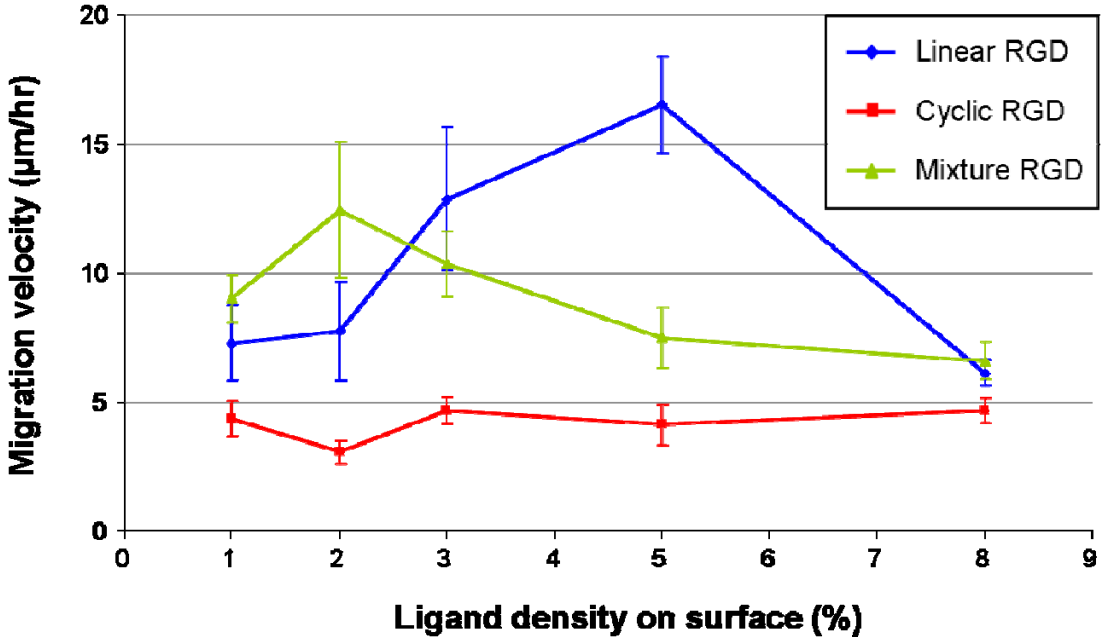

Figure 2-11. Plot of cell migration velocity versus surface density of linear, cyclic and mixture RGD peptide on non-dynamic surface**s.** For linear RGD peptide surfaces (blue line) there is a biphasic behavior where cell velocity increases as peptide density reaches from 1 % to 5 % and then decreases at higher densities of peptide. While the migration rate is low for cyclic RGD surfaces (red line), the mixture peptide surfaces render a biphasic behavior. Seven to ten individual cells from each experiment were tracked for 30 hours to give mean velocity. Data are mean ± SEM.

Determining Cell Migration Memory on Dynamic Surfaces - The Dynamic Presentation of Ligands Alters Cell Migration Rates

For metastatic cells the ability to migrate with different behavior and rates when originating from a tumor is of major interest in cancer biology. Although metastasis from a primary tumor is generally considered as a result of the complex interplay of random mutations, pre-existing genetic background and the local microenvironment, some types of tumors are metastasized by nonrandom processes [91, 92]. In this case, the microenvironment within and outside the primary tumors provide a selective path for metastasis. To explore the role of the dynamic microenvironment on cell motility, we wanted to test a novel hypothesis - whether the initial cell adhesion site and surroundings would influence subsequent migratory behavior of the cells or do cells have a migration memory that modulates their migration behavior after leaving the initial adhesion location. For this study, we employed the dynamic substrates to compare the rate of migration of cells from patterns onto regions presenting the same RGD ligand density and affinity as non-dynamic surfaces. If the initial location and environment affects cellular behavior, the dynamic and non-dynamic surfaces may induce different migratory behavior responses although the surface chemistry composition (ligand type and density) are identical. The cell migration on the dynamic surfaces was recorded by time-lapse microscopy in the same manner as Figure 2-10. In this set of experiment, the cells were first patterned on the fibronectin-adsorbed circular area and then linear or cyclic RGD was installed at 1 % and 2 % surface density. Upon exposure to the RGD ligand, the movement of the cells was recorded (Figure 2-12).

The plots in Figure 2-13 compare the total migration distances over time. For the *non-dynamic surfaces*, the migration on cyclic RGD is much slower than on linear RGD as

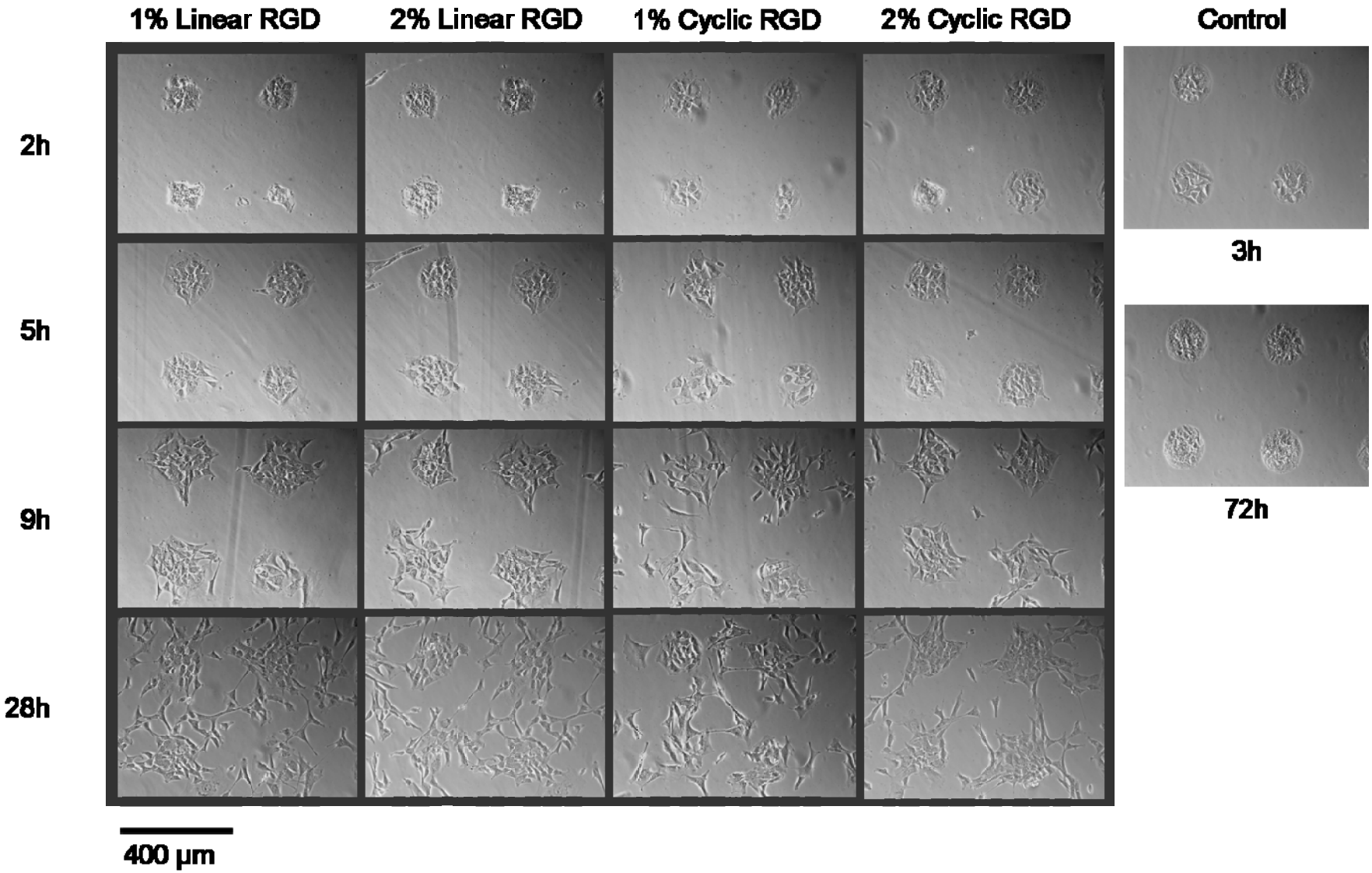
1% Linear RGD
2% Linear RGD
1% Cyclic RGD
2% Cyclic RGD
Control
2h
5h
9h
28h
3h
72h
400 µm

Figure 2-12. The images of cells from dynamic surfaces. Cells were first patterned on fibronectin-adsorbed circular area. The immobilization of linear and cyclic RGD on the surface was followed. The migration of the cells was recorded as time-lapse movie. The images at 2, 5, 9 and 28 hr after exposure to RGD are shown here. The control surface was not treated with RGD thus no cell migration was observed (right).

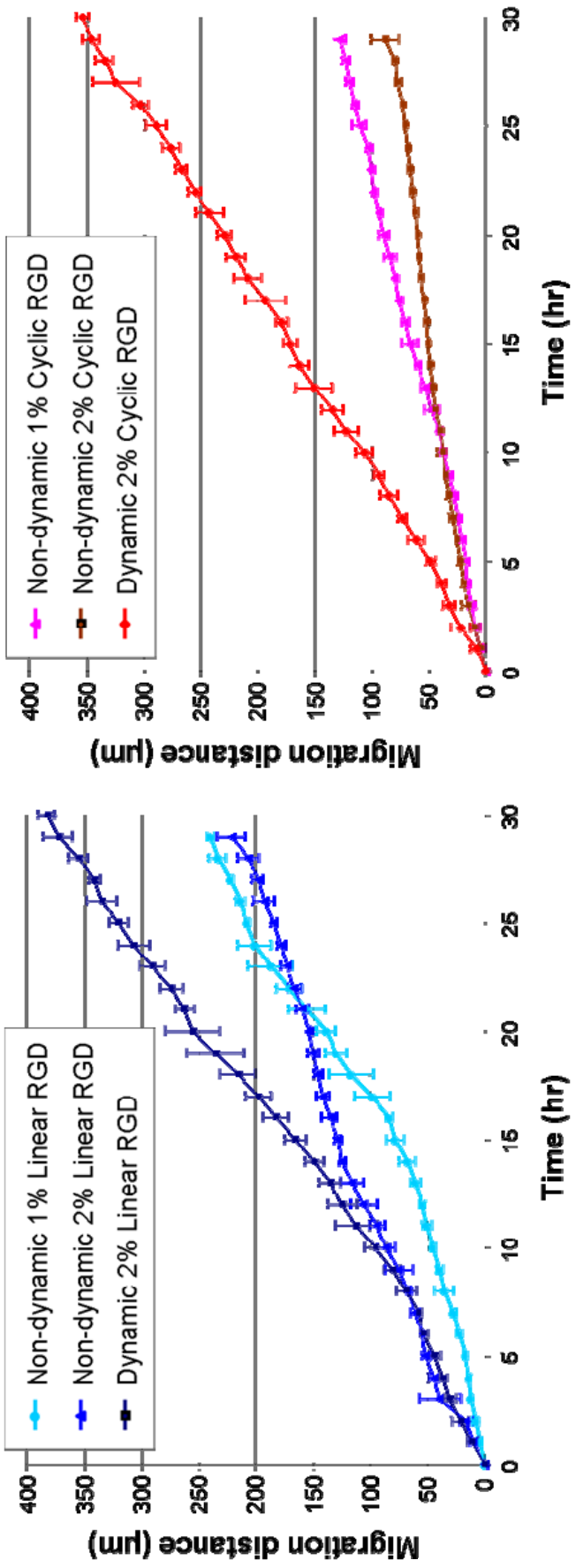
Migration distance (μm)
Time (hr)
Non-dynamic 1% Linear RGD
Non-dynamic 2% Linear RGD
Dynamic 2% Linear RGD
Migration distance (μm)
Time (hr)
Non-dynamic 1% Cyclic RGD
Non-dynamic 2% Cyclic RGD
Dynamic 2% Cyclic RGD

Figure 2-13. Comparison and evaluation of cell migration memory on dynamic and non-dynamic surfaces. The total distance cells migrated on dynamic or non-dynamic surfaces was plotted over 30 hours. The movement of cells every hour was tracked and summed up to get total distance cells migrated by that time. A. Cell migration on linear RGD surface. The average migration velocities were obtained from the slope of best fit line and they are 12.3 μm/hr (dynamic 2 %); 7.3 μm/hr (non-dynamic 1 %); 7.8 μm/hr (non-dynamic 2 %). B. Cell migration on cyclic RGD surface. The average migration velocities are 11.6 μm/hr (dynamic 2 %); 4.4 μm/hr (non-dynamic 1 %); 3.1 μm/hr (non-dynamic 2 %). Cells on the dynamic surfaces migrated much faster than cells on the non-dynamic surfaces regardless of ligand affinity. For each surface the experiment was repeated 6 times. The movement of a total of 10 to 12 cells on each surface was tracked and data are mean ± SEM.

expected due to the much higher affinity of cyclic RGD for integrin receptors. However, we observed on dynamic surfaces cells migrate much faster (from the initial patterns) regardless of ligand affinity. The average velocity of cell migration is similar for linear and cyclic dynamic surfaces (12.3 μm/hr and 11.6 μm/hr respectively). The most striking result is for the dynamic and non-dynamic cyclic RGD surfaces. The cells migrated much faster on dynamic surfaces presenting 2 % cyclic RGD when released from the initial pattern whereas on the non-dynamic 2 % cyclic RGD surface the cells migrated much more slowly. This result clearly demonstrates that cells retain a *memory* of their initial pattern or state and when released from the pattern they are able to modulate their ability to migrate that overcomes the adhesiveness of the ligands presented.

To further investigate these results we examined the focal adhesion structures within cells. Focal adhesions are large, dynamic protein complexes through which the cytoskeleton of a cell is connected to the ECM [4, 93]. The assembly and morphology of focal adhesions are critical in signal transduction during ligand mediated cell adhesion, polarization and migration. The focal adhesion structure of adhered cells on the surfaces were analyzed by visualization with an anti–paxillin antibody. Paxillin is a protein found within focal adhesions and is a well characterized marker for these structures [94]. More motile cells are known to have fewer focal adhesions and they are found at the periphery of the cell, which enhances attachment and detachment from the surface during active migration. Figure 2-14 shows focal adhesion staining of representative cells migrating on dynamic and non-dynamic linear and cyclic RGD surfaces. Interestingly, cells on the higher affinity non-dynamic cyclic RGD surfaces (bottom left micrograph) have more and larger focal adhesions and therefore cells migrate intermittingly and slowly, but on the dynamic surface presenting cyclic RGD

(lower right micrograph) the cells have focal adhesions only on the periphery and are very motile and look indistinguishable from cells on lower affinity RGD surfaces (top row). Since the cells are contact inhibited on the patterned islands we hypothesize that once they are allowed to migrate their motility program supersedes the affinity of the substrate in order for the cells to find more space to migrate and divide. We expected once the cells moved off the patterns onto high affinity cyclic RGD surfaces that the cells would immediately halt their migration due to the very high affinity of cyclic RGD to their cell surface integrin receptors. Instead, the cells migrated at a greater velocity and therefore the cells are somehow able to retain a memory of their initial pattern and are able to either down-regulate their integrin receptors or change the affinity state of the integrins to migrate. We also observed for longer periods (> 20 hours) some cells divided and the resulting daughter cells continued to be very motile and had similar focal adhesion size and number as the parent cells. This result brings the issue of persistence of cell motility memory that is carried through cell division. We are currently investigating whether the integrin receptors remain in the high active state of migration (with selective integrin antibodies) which is carried through cell division to the daughter cells. The study in the role of cell-cell communication, integrin activity (regulation) state and key gene signaling levels in the future may decipher the complex signaling that regulates this behavior. These results are the first to show that cells are able to modulate their migration behavior on a molecularly defined surface based on their initial position and may be important to understanding basic cell migration and the transition to metastasis for cancer cells from tumors.

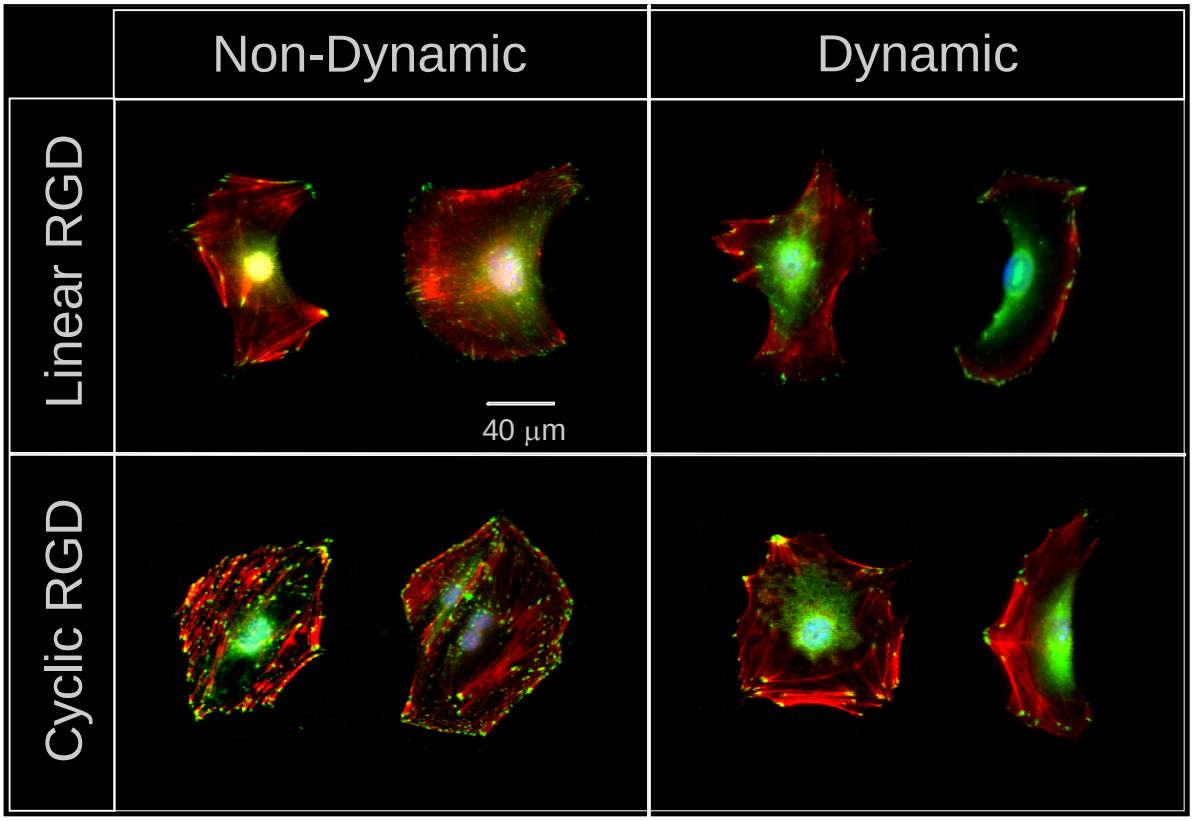

Figure 2-14. Comparison of fluorescent micrographs of fibroblasts with focal adhesion staining on dynamic and non-dynamic surfaces. Color: green, paxillin; red, actin; blue, nuclei.

Whole Genome Microarrays Reveal Differential Gene Expression on Dynamic and Non-Dynamic Surfaces

To investigate how the cells are able to modulate their migratory behavior at the genomic level on different RGD ligand affinity dynamic and non-dynamic surfaces, we incorporated whole genome microarray analysis with these molecularly tailored surfaces. We used this strategy to identify key genes that may be responsible for the cell migration memory mechanism that is employed to regulate cell behavior on different surface compositions.

A total of five different groups of samples were compared and the procedure is illustrated in Figure 2-15. For the fibronectin surfaces, the cells were seeded onto fibronectin patterns to which they adhered and became contact inhibited. The cells on this substrate were not exposed to the RGD ligand and therefore cells were not able to migrate and remained confined to the patterns (Figure 2-15A). For the dynamic surfaces, the substrates with patterned cells were activated electrochemically and RGD peptide immobilization was followed (Figure 2-15B). Either cyclic RGD or linear RGD was installed onto the surface. Upon recognizing the RGD ligand, cells initiated migration. For the non-dynamic surfaces, RGD peptide (cyclic or linear form) was coupled to the surface before adding cells (Figure 2-15C). For both dynamic and non-dynamic substrates, cells were incubated for 24 hours after migrating on immobilized RGD ligand surfaces. Cells on the fibronectin surface were also incubated for 24 hours. After this period of time, cells from each substrate were collected and RNA was extracted. Total RNA was purified, amplified and labeled with Cy5. As a reference, RNA was obtained from regularly cultured cells in tissue culture flasks and incorporated with Cy3 after purification and amplification. Each sample and reference was hybridized onto a

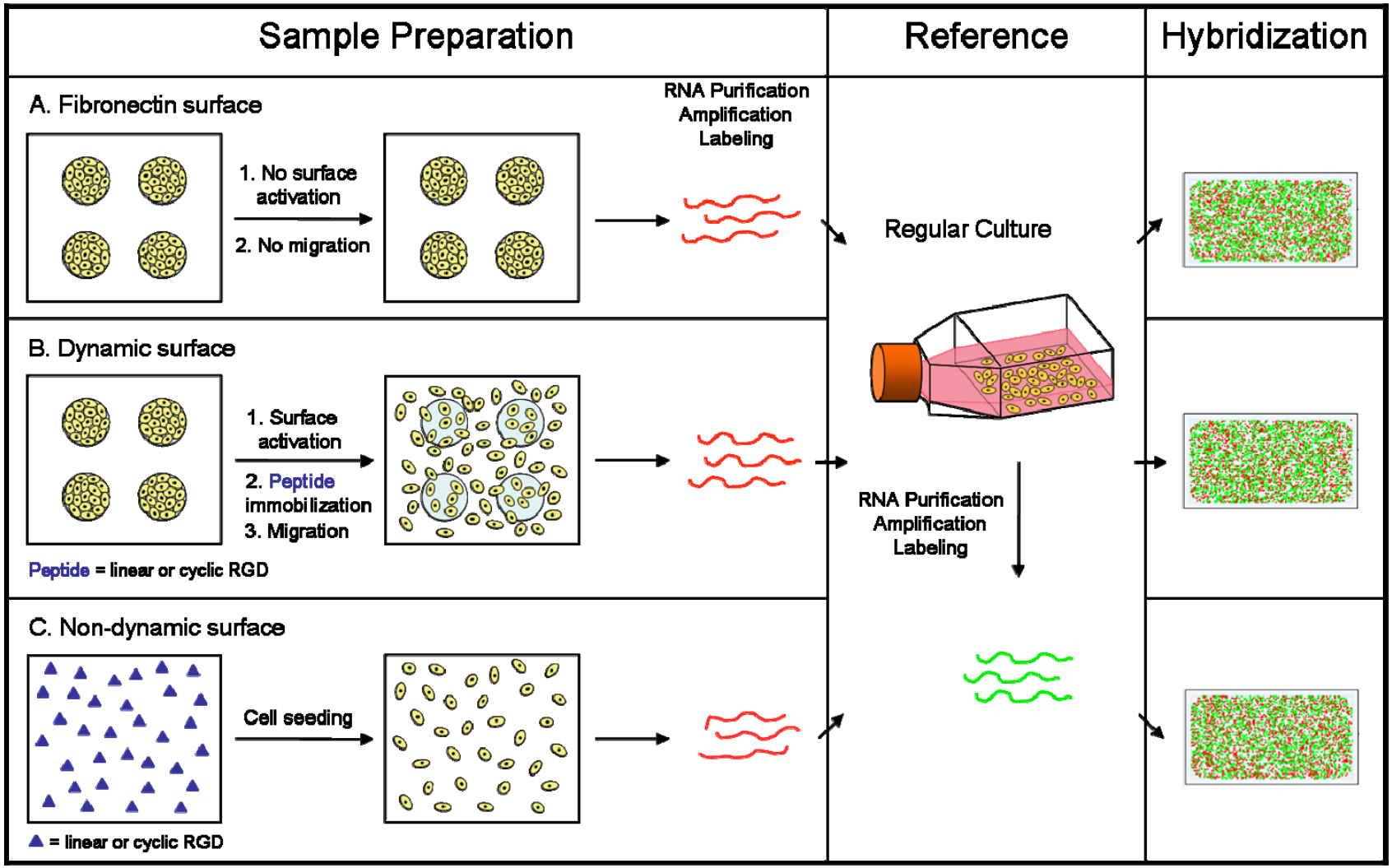
Sample Preparation
Reference
Hybridization
A. Fibronectin surface
1. No surface activation
2. No migration
RNA Purification
Amplification
Labeling
Regular Culture
B. Dynamic surface
1. Surface activation
2. Peptide immobilization
3. Migration
Peptide = linear or cyclic RGD
RNA Purification
Amplification
Labeling
C. Non-dynamic surface
Cell seeding
▲ = linear or cyclic RGD

Figure 2-15. Comparison of gene expression by whole mouse genome microarray. Schematic diagram of two-color whole genome microarray hybridization experiment. A. Fibronectin surface – microcontact printed area was adsorbed with fibronectin to enhance cell attachment. No RGD was added thus there was no cell migration; B. Dynamic surface – in the presence of the cells on the fibronectin patterns, RGD (linear or cyclic form) was immobilized. Cells were allowed to migrate for 24 hours in complete medium at 37 °C, 5 % CO_2; C. Non-dynamic surface – linear or cyclic RGD was immobilized on the SAM surface via an interfacial oxime linkage. Cells were added onto the surface and incubated for 24 hours in the same condition as above. From each surface cells were collected by trypsinization and RNA was extracted. RNAs were amplified using random primers and labeled with Cy5. For the reference of hybridization experiment, cells grown in common culture flask were harvested. RNA was extracted and amplified in the same method and labeled with Cy3. Labeled nucleic acid samples (A, B and C) and reference were used in microarray hybridization. After scanning the microarray slides, the intensity of two colors in each array was normalized and analyzed.

whole mouse genome microarray. Each microarray analysis visualizes differential gene expression between reference and the sample. By normalizing the data, gene expression levels between sample groups can also be compared.

Cell numbers in regular culture were maintained below 70 - 80 % confluency; hence these cells are regarded as proliferating and migrating at a normal rate. Cells on the fibronectin patterns are close packed and the resulting contact inhibition arrests both growth and migration. However, cells on the dynamic surface and non-dynamic surface are permitted to migrate freely on the RGD tailored surfaces, although how the cells gain access to the RGD ligands to initiate migration is different. A cluster image created by GeneSpring software visualizes differential gene expression levels between samples (Figure 2-16).

The gene expression pattern profiles are strikingly different for dynamic, non-dynamic and fibronectin surfaces. The ligand affinity between the cyclic and linear form of RGD also had interesting gene expression profile differences between dynamic and non-dynamic surfaces. For example, Myl7 (Myosin, light polypeptide 7, regulatory) which functions in focal adhesions, tight junctions and regulation of actin cytoskeleton shows higher expression on dynamic surfaces than the reference. In non-dynamic surface conditions it is expressed at even higher levels while fibronectin surface conditions kept the expression level similar to that of reference. Wnt6 (Wingless-related MMTV integration site 6) which is important in the Wnt and hedgehog signaling pathways is up-regulated on the fibronectin surface and dynamic surface but is significantly down-regulated on non-dynamic surface conditions. Cells on both dynamic and non-dynamic surfaces that had been exposed to RGD peptide expressed high levels of IL1a (interleukin-1-α). IL1a is known to be produced as a response to infection or environmental change to stimulate growth and initiate an immune response.

Interestingly the expression level is 3 to 4-fold higher on dynamic substrates, but cells that were directly added onto RGD surfaces expressed extremely high level (15 to 24-fold) of IL1a. Rasgrp2, Ras guanyl releasing protein 2, is a component in MAPK signaling pathway and it can activate Ras. It is up-regulated on dynamic and fibronectin surface samples but on non-dynamic surface samples it has only 60 % the level of regular expression.

Genes that show distinguished patterns between sample surface groups are summarized in Table 2-2. The numbers in the table represent the fold change in expression level compared to the reference sample. Many genes are found to be related to cell signaling pathways which regulate proliferation, migration, development and apoptosis. Also several genes functioning in focal adhesion and cytoskeleton organization/biogenesis are regulated differently according to the surface conditions. The integrin subunits responsible for fibronectin binding (α5β1) are expressed at similar levels for the dynamic surfaces compared to the reference. They are slightly up-regulated on non-dynamic surfaces while down-regulated on the fibronectin surface. A few other integrin subunits show characteristic expression patterns between samples while most integrin subunits have little variation in expression level when compared to the reference. Whether the regulation of such integrin subunit numbers on the cell surface at the transcription level is directly linked to cell migration is not clear. Some extracellular matrix protein genes are regulated at different levels depending on the surface conditions and how the cells use them to modify the surface for subsequent migration is to be investigated. From the overall microarray data analysis several of the genes that have the greatest difference in expression levels have roles in certain key signaling pathways related to proliferation and migration. In particular, a few candidate genes in the Wnt and Hedgehog signaling pathway are of great interest for their specific role

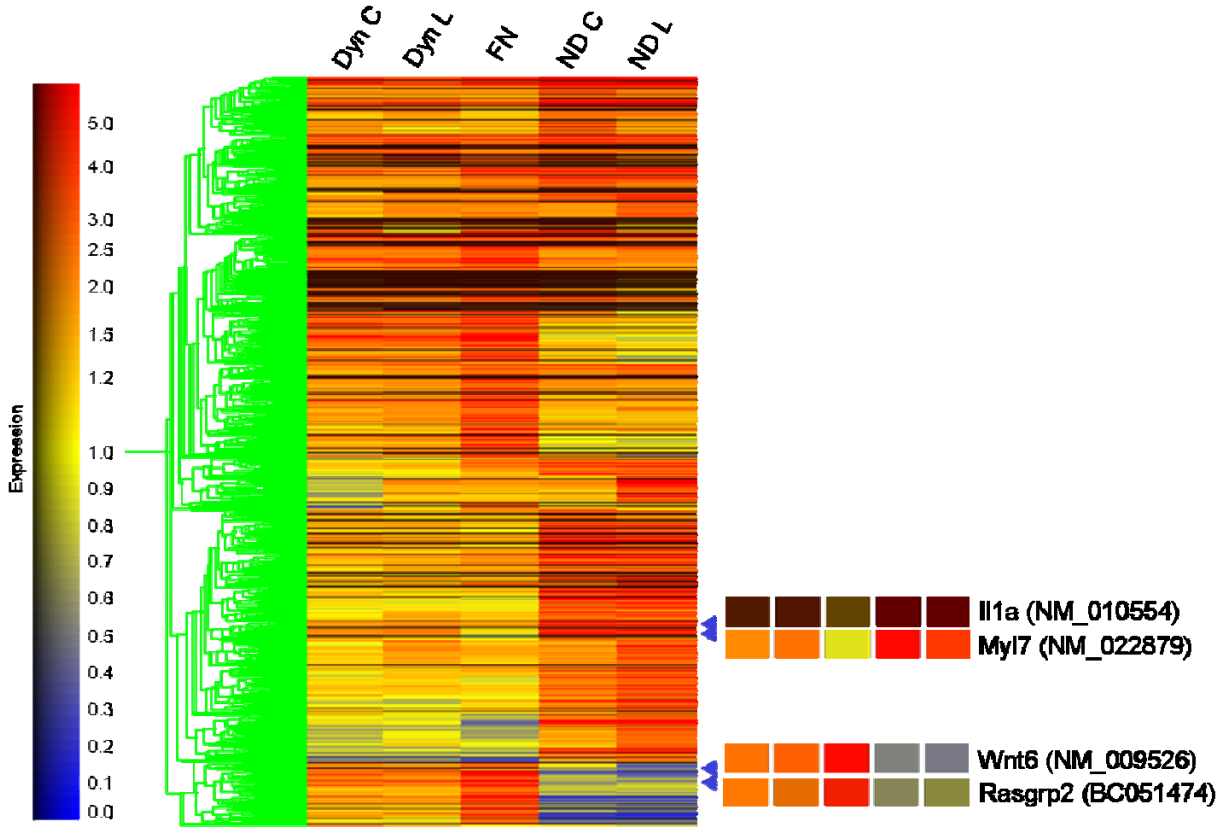

Figure 2-16. Hierarchical cluster analysis of microarray data. The expression profiles of 1716 genes whose intensity differed 2.5-fold or more between the reference and at least one sample were chosen for hierarchical clustering analysis with Genespring software. The cluster image was created according to underlying similarities in patterns of gene expression. The column represents each sample group, in which the mean of four separate microarray data are shown (t-test p-value less than 0.05). The genes are listed in rows. The normalized expression level for each gene is coded by color. Red indicates high expression and blue indicates low expression in each sample. For example, Il1a, interleukin-1-α, is extremely up-regulated in non-dynamic surface samples but only mildly up-regulated in dynamic and fibronectin surface samples. Myl7, Myosin light polypeptide 7, is significantly highly expressed in dynamic and non-dynamic surface samples while it is down-regulated in fibronectin surface sample (gene accession number in parentheses). The expression of Wnt6 and Rasgrp2, wingless-related MMTV integration site 6 and Ras guanyl releasing protein 2 respectively, are up-regulated on dynamic surfaces and fibronectin surface samples while the non-dynamic surface samples have much lower expression. [Dyn C], dynamic surface with cyclic RGD; [Dyn L], dynamic surface with linear RGD; [FN], fibronectin patterned surface; [ND C], non-dynamic surface with cyclic RGD; [ND L], non-dynamic surface with linear RGD].

in cell motility and proliferation mechanisms that influence cell migration memory. Because both Wnt signaling and Hedgehog signaling are important in the development stage, some genes may have key information for migration in development.

To validate the microarray data, semi-quantitative real time polymerase chain reaction (semi qPCR) for some genes was performed and the data was normalized with the data of Gapdh (glyceraldehyde-3-phosphate dehydrogenase) with the assumption that it is a housekeeping gene. The comparison of gene expression level from microarray data and PCR is shown in Table 2-3. Although the PCR method used was much less sensitive than the microarray for quantification of gene expression, the tendency of gene expression degree between surface samples appeared analogous. This genomic profiling analysis combined with proteomic analysis may reveal a signature map that regulates cell motility and cell migration memory.

The Effect of Synergy Peptide PHSRN on Cell Adhesion and Migration

We applied the same ligand coupling methodology to immobilize the PHSRN peptide, which is known as having a synergistic effect in cell adhesion, onto hydroquinone SAM (Figure 2-17). When cells were added onto a PHSRN-presenting (2 % surface density) surface we found that the cells behaved differently from a RGD-presenting surface. The cell movement on the PHSRN or RGD surface was recorded by time-lapse microscopy. The cells on the PHSRN surface generally showed highly dynamic protrusions of lamellipodia and ruffling. As some images are shown in Figure 2-18, the cells on the PHSRN surface threw their membrane out of their body very vigorously appearing like fast random walking while the cells on the RGD surface established some extent of adhesion to the surface.

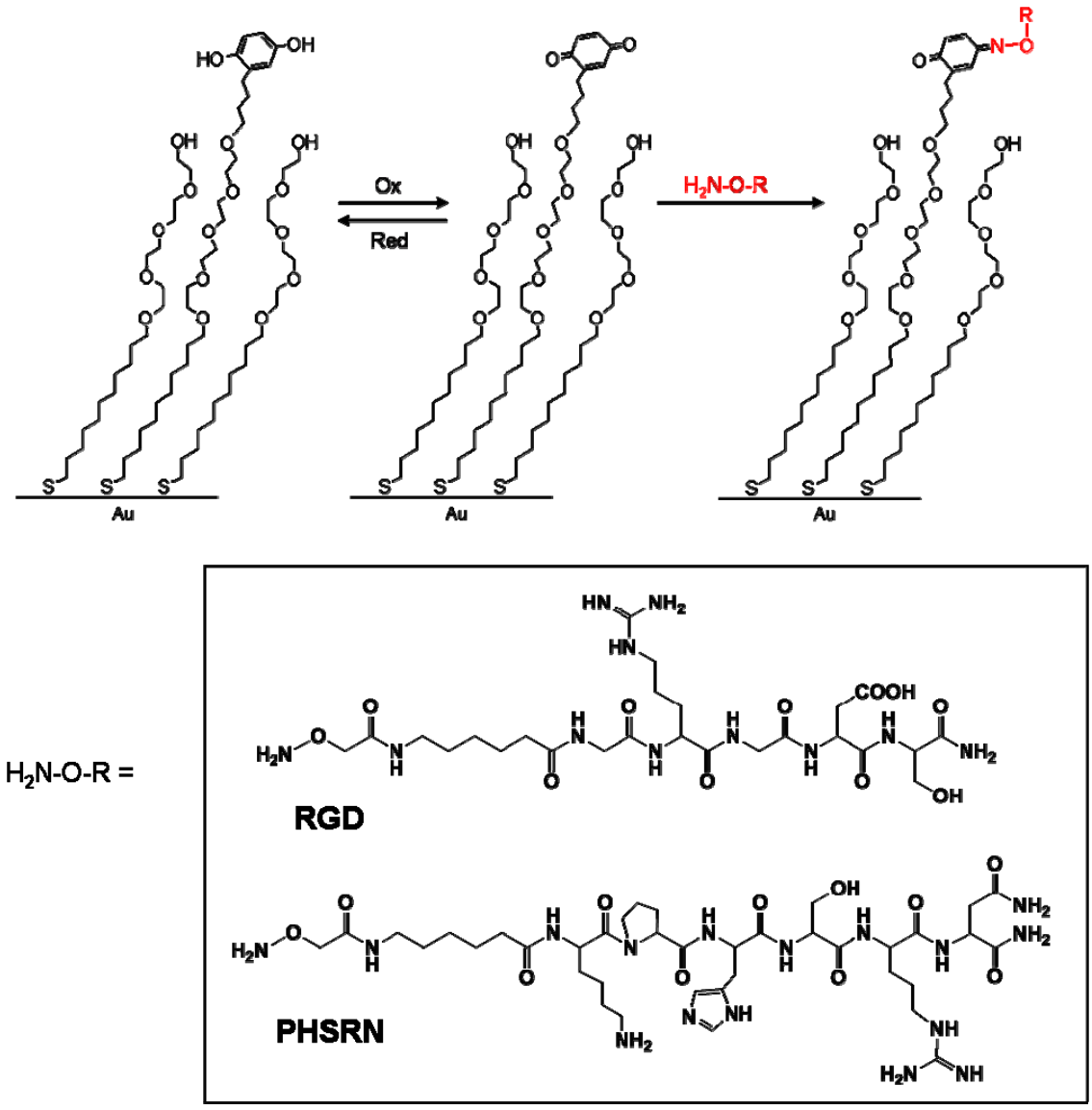

Figure 2-17. Immobilization of RGD and PHSRN onto hydroquinone/quinone monolayer.

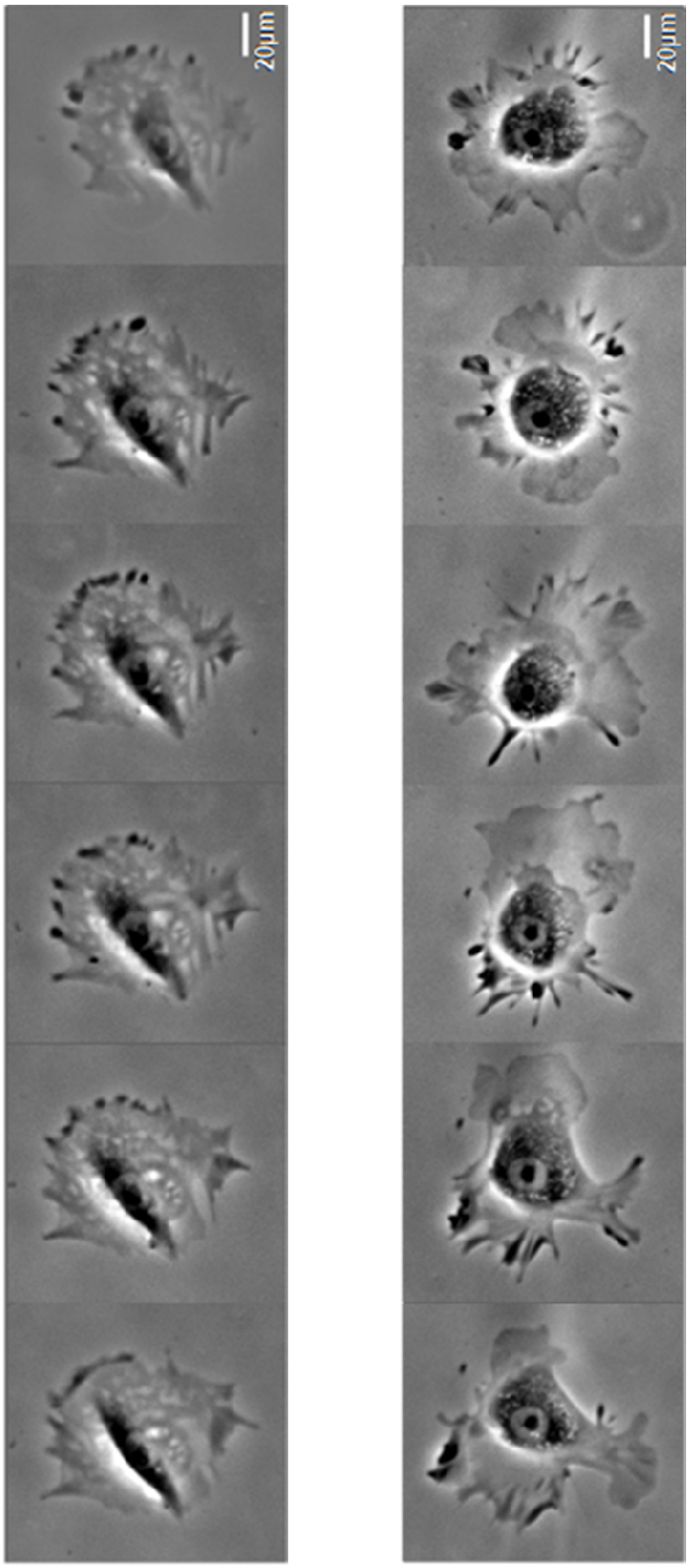
20μm
20μm
A
B

Figure 2-18. Cytoplasmic protrusions on the surface presenting RGD (A) and PHSRN (B). Images were taken every 20 minutes. Cells on PHSRN surface showed highly dynamic protrusions of lamellipodia. The lamellipodia stretched out 1.5 - 2 times of cell body toward all directions. The protrusion of the cells on RGD surface was less dynamic.

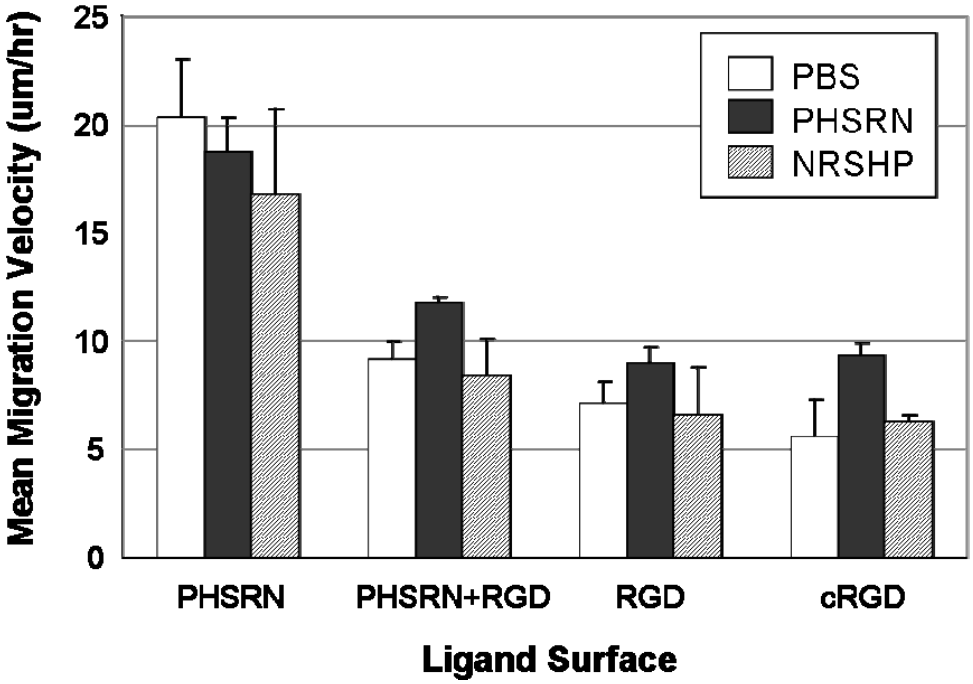

Figure 2-19. The effect of soluble PHSRN onto migration rate. The cells were incubated on the peptide-immobilized (total density 1 %) surfaces. Their movement was tracked upon addition of PBS (control), soluble PHSRN or scrambled peptide NRSHP into the medium (10 μM). The total distance cells migrated for 20 – 24 hours was used to obtain mean velocity. Migration is faster when soluble PHSRN is treated.

We also observed that addition of soluble PHSRN to the cell culture medium drove cells to move faster. Various surfaces with peptide immobilized at 1 % of total surface density were prepared. They included surfaces with PHSRN, linear RGD, cyclic RGD and mixture of PHSRN and linear RGD (1:1 ratio). After 2 hours incubation of the cells on those surfaces movie of the substrates were taken for at least 12 hours. Then soluble PHSRN was added into the cell culture at 10 μM concentration and the movie was taken for another 12 hours. Based on the movie images, cell movement was tracked and the total distance cells migrated over a certain time period gave the mean velocity of cell migration. Figure 2-19 compares the migration rates on various ligand surfaces before and after addition of soluble PHSRN. The fast moving cells on the PHSRN surface showed little decrease in motility after adding the soluble PHSRN, but overall they have the highest migration rate comparing to other ligand surface conditions. The migration rate of the cells on the other three ligand surfaces (i.e. linear RGD, cyclic RGD and mixture of PHSRN and linear RGD) increased after adding the soluble PHSRN. As a control experiment, soluble scrambled peptide NRSHP was added instead of PHSRN: it didn't affect the cell movement. The cells on the surface have their integrins already engaged to the ligand which was immobilized on the surface. How the soluble PHSRN would affect the pre-organized integrin-ligand interactions and therefore change the migratory behavior is interesting.

As focal adhesion morphology can provide information on migration, the immunostaining of focal adhesion was performed. It revealed that the cells on the PHSRN surface could form only a small number of focal adhesions in fibrillar shape at the edge of the cells which corresponds to the fast movement (Figure 2-20). In contrast, the cells adhered on the RGD surface had well-developed focal adhesions at the end of actin stress fiber as a

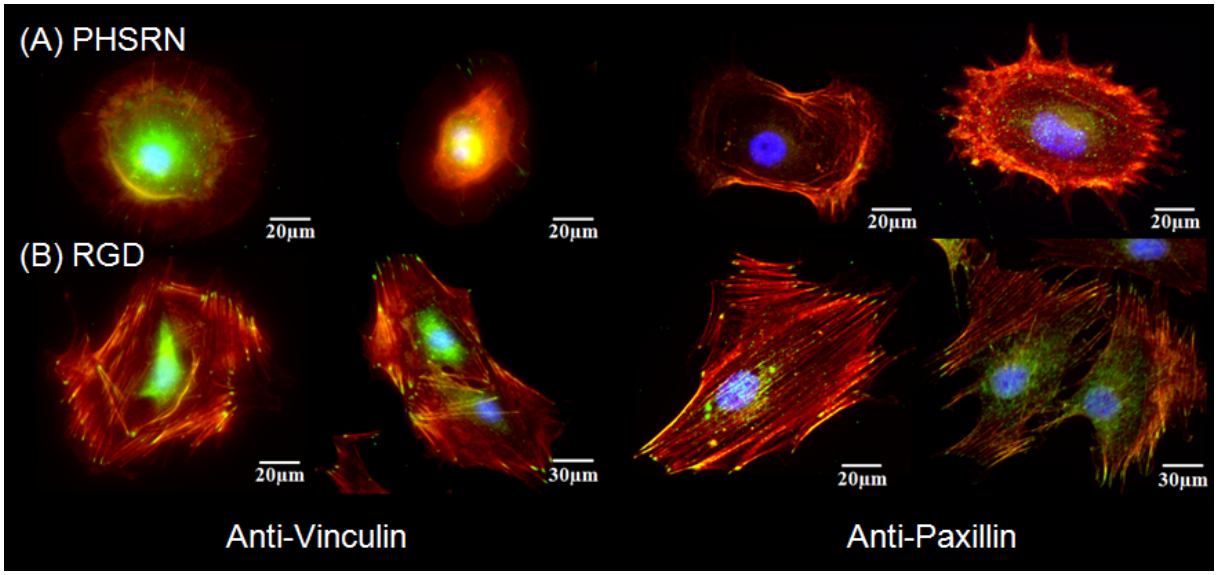

Figure 2-20. Fluorescence images of cells on the surface presenting PHSRN (A) and RGD (B). For characterization of focal adhesion, cells on PHSRN or RGD surface were immunostained with antibodies of vinculin and paxillin. On the PHSRN surface, staining with anti-paxillin does not show focal adhesion. However, staining with anti-vinculin shows clear fibrillar shape focal adhesions. Cells on the RGD-presenting surface showed many actin stress fiber bundles. More focal adhesions were observed for the cells on the RGD surface. Color: green, vinculin or paxillin; red, actin; blue, nuclei.

dot-like shape which is observed in stationary cells rather than migratory cells. This implies that when integrins interact with the RGD or PHSRN ligand they form different focal adhesion in size and shape that are probably caused by recruiting different components at the adhesion site thus affecting downstream signaling.

Rho family GTPases are key regulators of the cytoskeleton, determining cell shape, attachment and movement [24]. Rho proteins act as molecular switches, "on" when GTP-bound, which transduce signals through associated effector proteins, including kinases Rho kinase (ROK) and p21-activated kinase (PAK). In response to extracellular signals and guidance cues, Rho GTPases are activated by exchange factors (GEFs) and down regulated by GTPase activating proteins (GAPs) (Figure 2-21).

One model for how migrating cells maintain polarity is based on the fact that Rho and Rac are mutually antagonistic, each suppressing the other's activity [95]. Active Rac at the leading edge of cells would suppress Rho activity, whereas Rho would be more active at the sides and rear of the cell and suppress Rac activity, thereby preventing Rac-mediated protrusion at sites other than the leading edge. Figure 2-22 summarizes how Rho, Rac and Cdc42 take part in cell motility [96]. Cdc42 regulates polarity, Rac stimulates lamellipodial extension, and Rho regulates rear retraction.

To investigate whether the distinguished features of membrane protrusions, focal adhesion and motility on RGD and PHSRN surfaces is related to the activity in Rac and Rho, we performed GTPase activity assay with the cells cultured on RGD and PHSRN surfaces. As described in Figure 2-23, the assay uses agarose beads attached with GTPase-binding protein which can bind only to the active GTPase. If a cell lysate sample contains active GTPase, the beads will "pull-down" the active form of GTPase and the isolated active

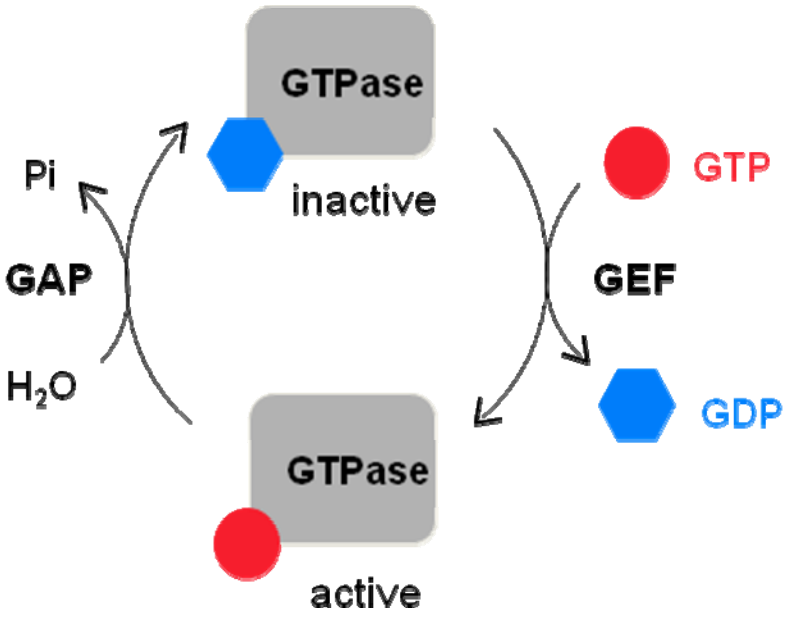

Figure 2-21. The regulation of GTPase activity. GTPases are activated by exchange factors (GEFs) and down regulated by GTPase activating proteins (GAPs).

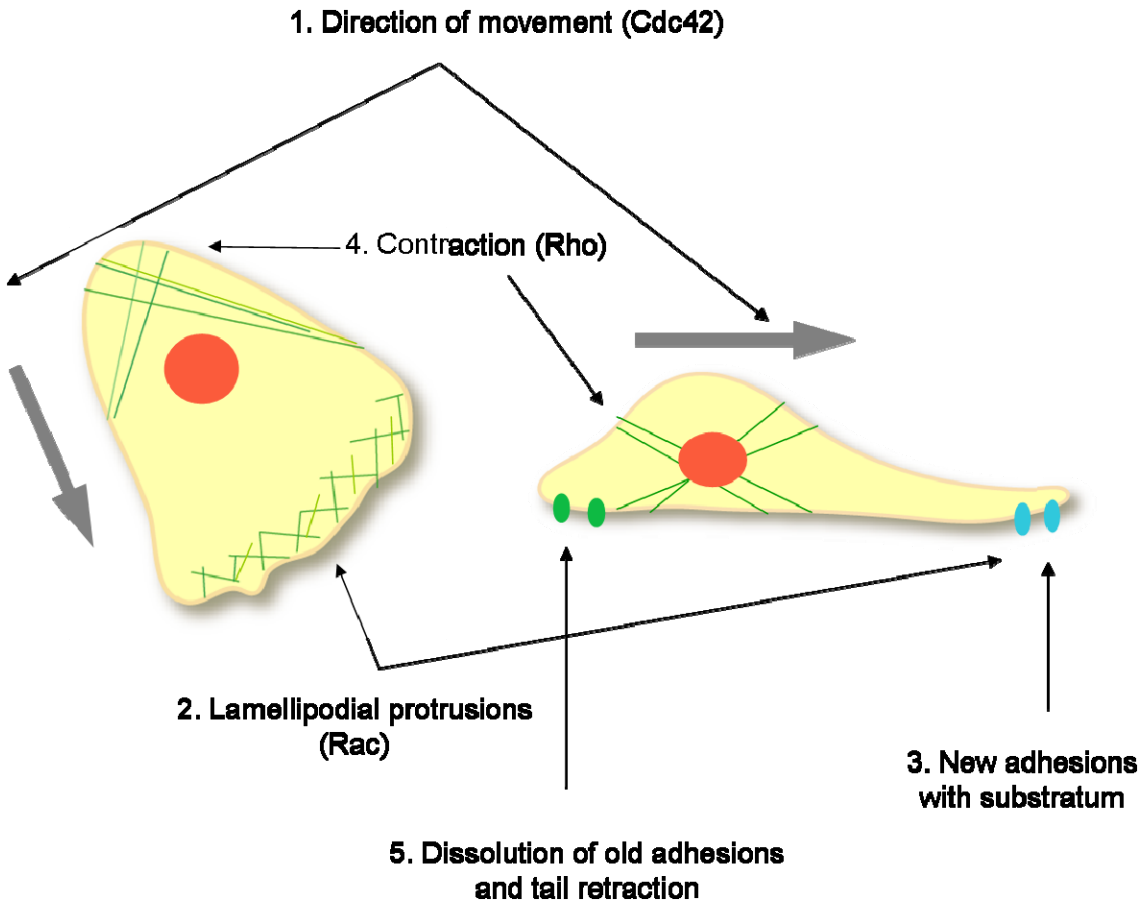

Figure 2-22. Factors in cell motility. The figure was adapted and modified from reference 96.

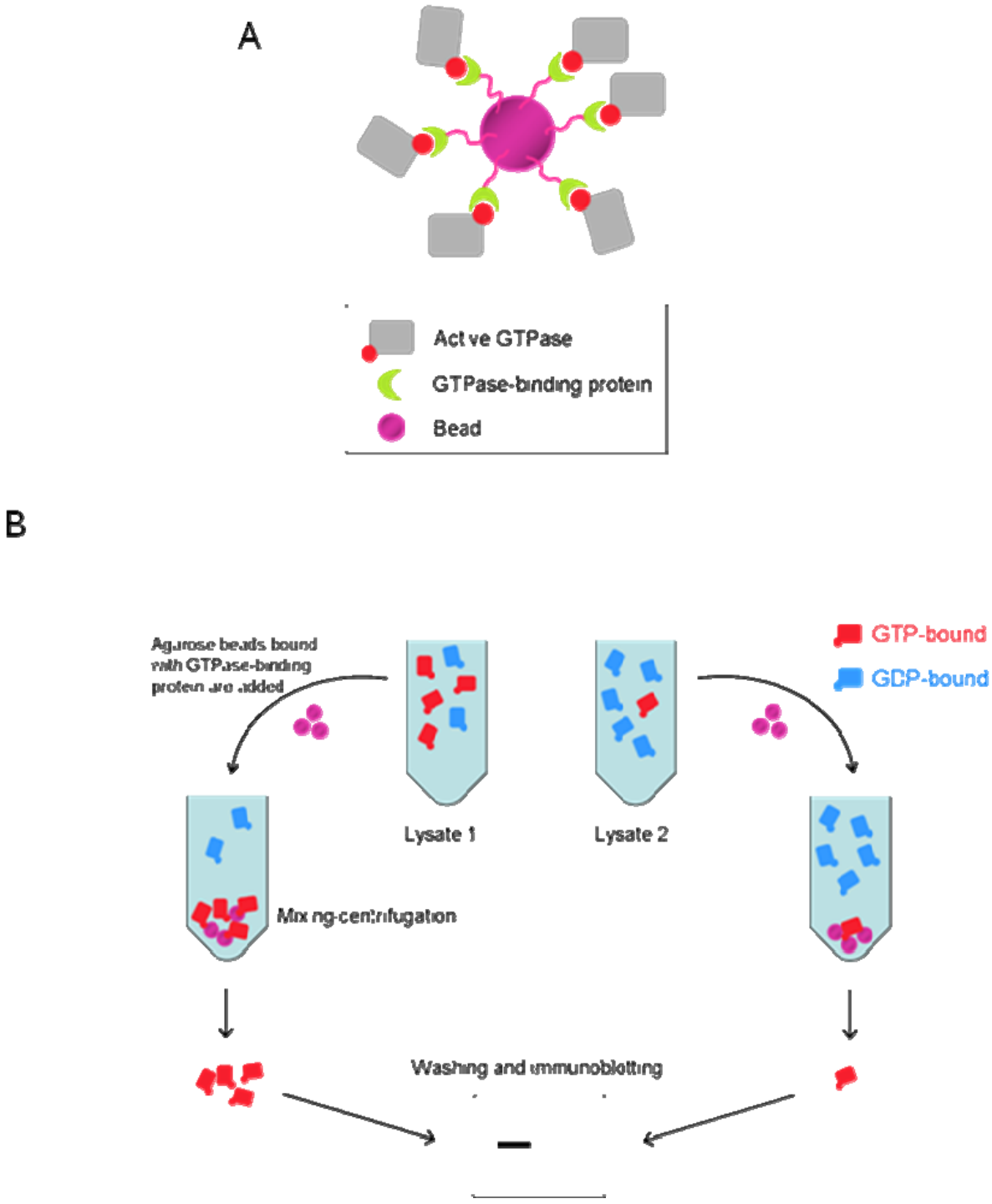

Figure 2-23. GTPase activity assay. A. The assay uses GTPase-binding protein bound bead to selectively pull down active form of GTPase. B. The overview of pull-down assay for GTPase. The active GTPases which were pulled down by the beads can be quantified by immunoblot.

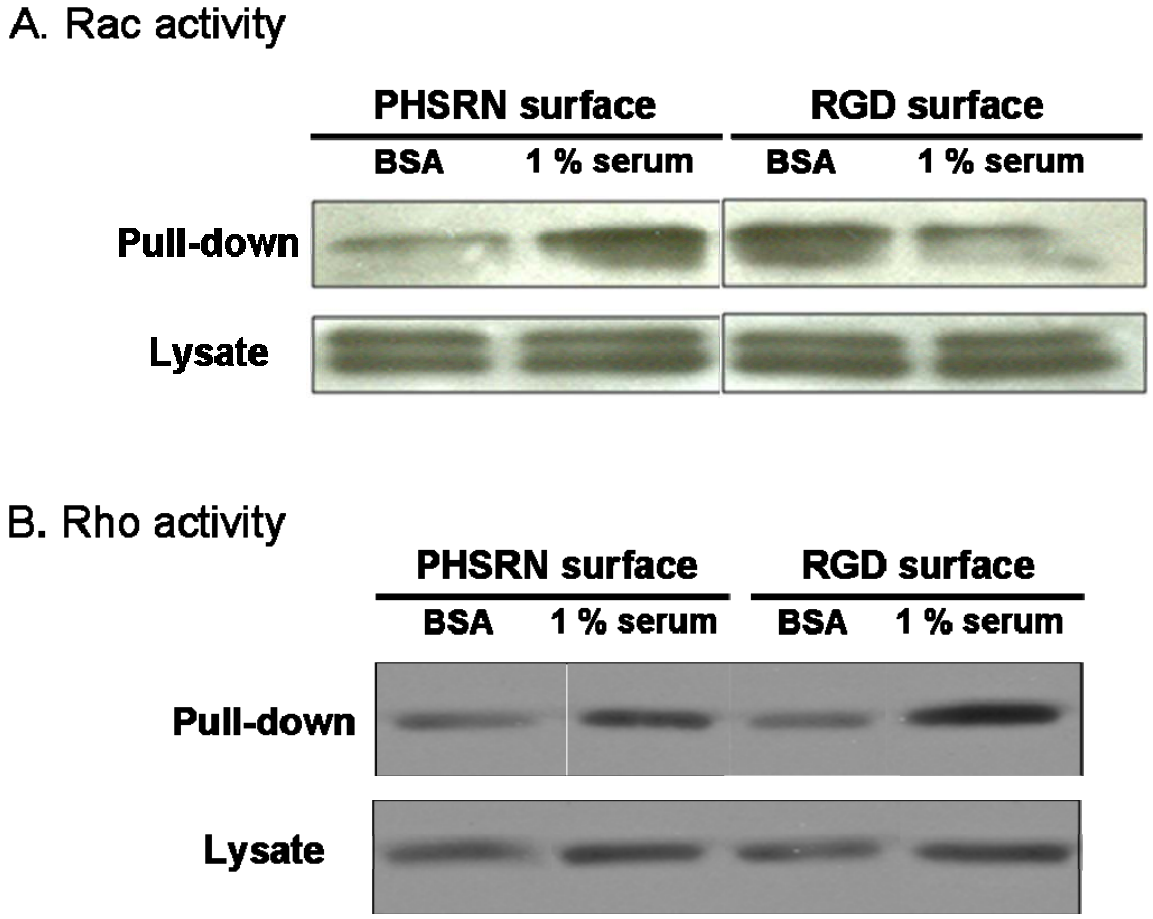

Figure 2-24. The activity of Rac and Rho was compared from the cells cultured on RGD and PHSRN surfaces by pull-down assay. For the Rac activity before and after serum stimulation, the cells on the PHSRN surface showed increased activity while the cells on the RGD surface had decreased activity after serum stimulation. The cells on the RGD surface only showed significant Rho activity increase by serum treatment.

GTPase can be quantified by using immunoblotting (Western blotting). The activity of Rac1 and Rho was specifically assayed. Since our observation was sustained behaviors rather than instant reaction by adhesion onto the surface, we incubated 2 hours on the surface before proceeding to the activity assay. The growth factors in serum which is added in cell culture medium also stimulate Rho and Rac so we performed the assay separately with serum-starved condition (0.5 % BSA) and serum- fed condition (1 % bovine calf serum).

As shown in Figure 2-24, the change in Rac activity before and after serum stimulation is contradictory on PHSRN and RGD surfaces. The Rac activity of the cells on the PHSRN surface was increased while it dropped on the RGD surface after serum stimulation. In the case of Rho activity, only integrin interaction with RGD allows significant Rho activity increment by serum treatment. These results are consistent to the observation in that the cells on the PHSRN are highly motile without polarity while the cells on the RGD surface develop focal adhesion and actin cytoskeleton. This assay also implies that the integrin interaction with PHSRN and RGD triggers different downstream signaling pathways. The nature of the integrin conformation or activation state may recruit molecular components in the focal adhesion in a different manner and it consequently turns on different effector GTPases.

Conclusion

A dynamic substrate has been generated and shown to have spatial and temporal control of cell behavior. The model substrate is based on an electroactive surface where patterned cells can be released upon mild electrochemical activation to install adhesive ligands which are required to initiate and support cell migration and growth. The use of the reversible hydroquinone-quinone system that is under external electrochemical control allows for the

quantitative real-time change in surface properties in the presence of adhered cells. The chemoselective reaction between soluble oxyamine-tethered ligands and the quinone form of the redox couple is compatible with cell culture conditions and this synthetic flexibility allows for tailoring the surface with a variety of biomolecules and ligands. The use of cyclic voltammetry to distinguish between the diagnostic peaks of the product oxime and the initial hydroquinone-quinone peaks is essential for characterizing the extent of the interfacial reaction and therefore allows for the precise control of ligand density on the surface.

It was shown that the dynamic surface has exquisite molecular control of the ligand-receptor interaction between cell and material and it was demonstrated the utility of this methodology by studying the interplay of cell population, ligand density, geometry and integrin composition on cell behavior in real-time. We have also shown for the first time a novel behavior of cell migration memory where cells are able to change their migration velocity and focal adhesion patterns depending on their initial position that supersedes the underlying surface chemistry. Furthermore, whole genome microarray analysis showed several genes regulating cell signaling, cytoskeleton organization and proliferation are expressed at significantly different levels depending on the spatio-temporal control of the surface composition. The ability of the surface to immobilize various kinds of biological ligand allowed the comparison of signaling pathways as well as the observed behaviors.

The dynamic and non-dynamic surfaces can be potentially used to decipher how the dynamic microenvironment influences cell motility in cancer cell biology and development.

Table 2-2. Summary of microarray data (numbers indicate the fold change in expression level compared to the reference sample)

Category	*Dyn C	Dyn L	FN	ND C	ND L	Name	Symbol
Signaling	3.09	3.75	2.78	15.64	13.12	Wingless-related MMTV integration site 2	Wnt2
	2.51	2.90	5.77	0.50	0.48	Wingless-related MMTV integration site 6	Wnt6
	2.48	3.22	8.89	0.81	0.89	Axin2	Axin2
	2.75	2.57	3.00	0.67	0.77	Secreted frizzled-related protein 1	Sfrp1
	3.35	3.81	1.46	23.96	15.28	Interleukin 1 alpha	Il1a
	2.37	2.37	4.91	0.60	0.69	RAS, guanyl releasing protein 2	Rasgrp2
	2.42	3.52	5.68	1.37	1.11	Patched homolog 2	Ptch2
	1.31	1.81	1.17	15.94	14.69	Amphiregulin	Areg
Focal Adhesion/ Regulation of Actin	4.05	3.09	5.99	9.48	15.43	Von Willebrand factor homolog	Vwf
	3.09	3.09	3.62	13.86	10.71	NCK associated protein 1 like	Nckap1l
	1.54	0.75	2.55	0.28	0.23	Insulin-like growth factor 1	Igf1
	1.65	1.88	0.50	0.46	0.29	Actin, alpha 2, smooth muscle, aorta	Acta2
	2.03	2.50	0.90	5.60	4.09	Myosin, light polypeptide 7, regulatory	Myl7
Integrins	7.32	8.38	13.85	1.12	0.63	Integrin, alpha 11	Itga11
	1.50	1.92	1.64	5.39	7.78	Integrin alpha 2	Itga2
	1.04	0.98	0.56	1.80	2.85	Integrin alpha 5 (fibronectin receptor alpha)	Itga5
	0.83	0.91	0.52	1.10	1.17	Integrin beta 1 (fibronectin receptor beta)	Itgb1
Adhesion Molecules	1.34	1.54	3.02	0.64	0.48	Intercellular adhesion molecule	Icam1
	0.88	0.86	2.42	9.45	9.69	Cadherin EGF LAG seven-pass G-type receptor 1	Celsr1
	1.50	1.80	1.30	5.38	5.56	Cadherin 5	Cdh5
	1.53	1.63	0.98	12.77	16.94	Cadherin 6	Cdh6
	2.71	2.81	3.57	10.13	8.98	Junction adhesion molecule 2	Jam2
Extracellular Matrix	1.66	1.56	3.00	0.49	0.32	Procollagen, type II, alpha 1	Col2a1
	3.82	4.78	7.82	3.86	4.20	Procollagen, type XVIII, alpha 1	Col18a1
	6.63	5.24	7.51	1.23	0.98	Laminin, alpha 4	Lama4
	0.71	0.68	0.52	4.56	5.20	Laminin, beta 3	Lamb3
Growth	1.43	1.81	2.31	8.47	6.59	Fibroblast growth factor 21	Fgf21
	1.84	2.19	0.49	2.74	2.22	Connective tissue growth factor	Ctgf
	3.47	2.70	1.33	4.69	3.38	Gremlin 2 homolog, cysteine knot superfamily (Xenopus laevis)	Grem2
	0.66	0.84	0.87	3.81	3.65	Growth differentiation factor 9	Gdf9
Apoptosis	0.86	1.31	1.80	1.29	1.38	Caspase 9	Casp9
	0.52	0.47	1.13	1.23	1.69	Aldehyde dehydrogenase 1 family, member L1	Aldh1l1
	3.78	4.38	4.83	11.56	12.36	Aldo-keto reductase family 1, member C18	Akr1c18

*Symbols:
Dyn C – Dynamic surface with cyclic RGD
Dyn L – Dynamic surface with linear RGD
FN – Fibronectin patterned surface
ND C – Non-dynamic surface with cyclic RGD
ND L – Non-dynamic surface with linear RGD

Table 2-3. Microarray data vs. semi-qPCR data

	Dyn C	Dyn L	FN	ND C	ND L	Name
Itga11	7.32	8.38	13.85	1.12	0.63	Integrin, alpha 11
(PCR)	*2.16*	*2.67*	*2.35*	*0.79*	*0.65*	
Itga5	1.04	0.98	0.56	1.80	2.85	Integrin alpha 5 (fibronectin receptor alpha)
(PCR)	*1.09*	*1.36*	*0.90*	*0.93*	*1.26*	
Itgb1	0.83	0.91	0.52	1.10	1.17	Integrin beta 1 (fibronectin receptor beta)
(PCR)	*1.05*	*1.17*	*0.91*	*0.93*	*0.98*	
Col1a2	1.70	1.27	1.97	0.55	0.52	Procollagen, type I, alpha 2
(PCR)	*1.43*	*1.03*	*0.97*	*1.07*	*1.11*	
Col2a1	1.66	1.56	3.00	0.49	0.32	Procollagen, type II, alpha 1
(PCR)	*0.94*	*0.61*	*0.76*	*0.83*	*0.78*	
Wnt2	3.09	3.75	2.78	15.64	13.12	Wingless-related MMTV integration site 2
(PCR)	*1.92*	*0.40*	*0.63*	*1.32*	*1.21*	
Wnt6	2.51	2.90	5.77	0.50	0.48	Wingless-related MMTV integration site 6
(PCR)	*4.46*	*2.38*	*1.47*	*1.16*	*1.34*	
Ctnnb1	1.12	0.79	1.12	0.90	1.14	Catenin (cadherin associated protein), beta 1
(PCR)	*1.12*	*1.04*	*1.02*	*1.17*	*1.30*	
Actb	0.96	1.59	0.89	1.55	2.35	actin, beta, cytoplasmic
(PCR)	*0.73*	*0.61*	*0.64*	*0.87*	*0.86*	
Tcf7	1.49	1.22	2.51	2.65	4.15	transcription factor 7, T-cell specific
(PCR)	*1.20*	*0.65*	*0.74*	*1.12*	*1.67*	
Gapdh	1.21	1.11	1.20	1.23	0.90	glyceraldehyde-3-phosphate dehydrogenase
(PCR)	*0.80*	*0.77*	*0.87*	*0.93*	*0.93*	

Materials and Methods

Preparation of Monolayers

All gold substrates were prepared by electron-beam deposition of titanium (3 nm) and then gold (12 nm) on glass cover slips (7.5 cm × 2.5 cm). All gold coated glass substrates were cut into 1 cm^2 pieces and washed with absolute ethanol. The substrates were immersed in an ethanolic solution containing the alkanethiols (1 mM) for 12 hours, and then cleaned with ethanol prior to each experiment.

Electrochemical Measurements

All electrochemical experiments were performed using a BAS 100B/W Electrochemical Analyzer (Bioanalytical Systems, Inc., West Lafayette, IN). Electrochemistry on SAMs was performed in 1 M $HClO_4$, using a platinum wire as the counter electrode, Ag/AgCl as reference, and the gold SAM substrate as the working electrode. All cyclic voltammograms were recorded at a scan rate of 50 mV/s.

Solid-Phase Peptide Synthesis

All peptides were synthesized by an automated solid phase peptide synthesis using the CS136XT Peptide Synthesizer (CS Bio Co., Menlo Park, CA).

Linear RGD Fmoc (9-fluorenylmethoxycarbonyl)-protected amino acids were used on Fmoc-Ser(tBu)-Rink Amide-MBHA resin. Synthesized peptide was cleaved from the resin by agitating in a solution of trifluoroacetic acid (TFA):water:triisopropylsilane (95:2.5:2.5) for 3 hours. TFA was evaporated and the cleaved peptide was precipitated in cold diethyl ether. The water-soluble peptide was extracted with water and lyophilized. Mass spectral data

confirmed the peptide product. MS (ESI) (m/z): [M+H$^+$] calculated for linear RGD-oxyamine ($C_{25}H_{45}N_{11}O_{11}$), 676.69; found, 676.5. [M+H$^+$] calculated for control scrambled peptide, GRD-oxyamine ($C_{25}H_{45}N_{11}O_{11}$), 676.69; found, 676.4. [M+H$^+$] calculated for control soluble peptide RGD ($C_{17}H_{31}N_9O_8$), 490.48; found, 490.3.

Cyclic RGD The peptide DfKRG was synthesized using H-Gly-OH preloaded 2-chlorotrityl resin. The mixture of acetic aicd:trifluoroethanol:dichloromethane (1:1:3) was added for cleavage. The resulting peptide was dissolved in DMF and added with N, N-diisopropylethylamine (DIEA) and PyBOP. The reaction was stirred for 12 hours and the solvent was removed in vacuum. The resulting cyclic peptide was treated with TFA:water:triisopropylsilane (95:2.5:2.5) for 3 hours and precipitated in diethyl ether. To introduce the oxyamine group on Lys side chain, the peptide was treated with BOC-aminooxy acetic acid, PyBOP and DIEA in DMF for 10 hours. After removing DMF, the peptide was added with TFA for 1 hour and precipitated in diethyl ether. The sample was dissolved in water and purified by HPLC (Waters). MS (ESI) (m/z): [M+H$^+$] calculated for cyclic RGD-oxyamine ($C_{29}H_{44}N_{10}O_9$), 677.72; found, 677.4.

Cell Culture

The 3T3-Swiss albino cells (Tissue Culture Facility, UNC at Chapel Hill) were cultured in Dulbecco's Modified Eagle's Medium (Sigma) supplemented with 10 % bovine calf serum (Hyclone) and 1 % penicillin/streptomycin (100 units of penicillin/ 100 μg of streptomycin per mL, Gibco) at 37 °C and 5 % CO_2. To detach cells from the culture flask, cells were rinsed with phosphate-buffered saline twice (PBS, sigma) and 0.05 % trypsin /0.53 mM EDTA (Gibco) was added. After incubating for 5 minutes, cells were resuspended in serum-

free medium and centrifuged at 1000 rpm for 5 minutes to remove trypsin. Cells were resuspended in serum-free medium and added onto the substrates for the experiments.

CHO cell lines B2a27, B2a10, and B2 were gift from Prof. Rudy Juliano. CHO cells were cultured in Minimum Essential Medium Containing GlutaMAX™-I (L-Alanyl-L-Glutamine) substituted on a molar equivalent basis for L-glutamine (Gibco) supplemented with 10 % fetal bovine serum (Hyclone) and 1 % penicillin/streptomycin (Gibco) at 37 °C and 5 % CO_2. The same procedure as above was used to detach cells from the culture flask.

Preparation of Dynamic Surfaces

Microcontact printing was used to print hexadecanethiol on the gold-coated substrates in circular or linear patterns with a poly(dimethylsiloxane) stamp. The substrates were immersed in a 1 mM ethanol solution of hydroquinone-terminated alkanethiol and tetra(ethylene glycol)-terminated alkanethiol for 12 hours to make mixed SAMs. The substrates were rinsed with absolute ethanol and dried under air flow. The patterned regions with hexadecanethiolate monolayer were adsorbed with fibronectin (from bovine plasma, Sigma) by adding a solution of fibronectin in PBS (0.1 mg/mL) onto substrates. After 2 hours, the substrates were rinsed with water and dried. The 3T3-Swiss albino cells in serum-free medium were seeded onto the SAM substrates in a concentration of 10^5 cells/mL and incubated at 37 °C and 5 % CO_2. After 3 hours, the serum-free medium was replaced with serum-containing medium and incubated at the same condition. When cells were attached and relaxed evenly on the patterns (usually after 10 – 12 hours), the substrates were rinsed in serum-free medium twice. The substrates were oxidized electrochemically at 750 mV for 5 seconds. To the substrates was added 20 mM RGD-oxyamine peptide (linear, cyclic or mixture RGD) solution in serum-free medium and incubated at 37 °C and 5 % CO_2 for 2

hours. The substrates were then placed in serum-containing medium and incubated at 37 °C and 5 % CO_2 and monitored with live cell microscopy.

Preparation of Non-dynamic Surfaces

Mixed SAMs were prepared by immersing gold-coated glass cover slips in a 1 mM ethanol solution of hydroquinone-terminated alkanethiol (1 to 10 % in v/v) and tetra(ethylene glycol)-terminated alkanethiol for 12 hours. The substrates were rinsed with absolute ethanol and dried under air flow. The substrates were oxidized electrochemically at 750 mV for 10 seconds and rinsed with water. The substrates were incubated with 20 mM RGD (linear, cyclic or mixture RGD peptide) in PBS for 3 hours at room temperature. The substrates were then washed in water and dried. 3T3-Swiss albino fibroblasts were then added in the concentration of 10^4 cells/mL. The low cell seeding density is in order to exclude interactions between cells.

Immunostaining for Fluorescence Microscopy

Adherent cells were fixed with 3.2 % paraformaldehyde in PBS for 10 minutes and then permeabilized with 0.1 % Triton-X100 in PBS (PBST) for 10 minutes. Cells were then stained with anti-paxillin antibodies (1:200, BD biosciences) or anti-α-tubulin antibodies (1:500, Sigma) in PBST containing 5 % goat serum for 1 hour, followed by Cy2-conjugated goat anti-mouse IgG (1:200 in PBST, Jackson ImmunoResearch), phalloidin-tetramethylrhodamine B isothiocyanate (1:100 in PBST, Sigma), and DAPI (4', 6-diamidino-2-phenylindole dihydrochloride, Sigma) (1:500 in PBST) for 1 hour. Substrates were rinsed with deionized water before being mounted onto glass cover slips for microscopy. All optical

and fluorescent micrographs were imaged using a Nikon inverted microscope (model TE2000–E). All images were captured and processed by MetaMorph.

Movies

Time-lapse images were recorded by 2 or 5 minutes interval for 30 – 72 hours. The images were combined using MetaMorph software to create movie files. Cell tracking function in MetaMorph was used to measure the total distance cells had migrated on dynamic or non-dynamic surfaces.

BrdU Staining

Actively growing cells on the dynamic surfaces were pulsed for 1 hour with 10 μM BrdU (bromodeoxyuridine, Sigma) at 37 °C and 5 % CO_2. After washing with PBS, ice cold 70 % ethanol was added and cells were incubated for 20 minutes at room temperature (RT). Cells were washed in PBS and then 2 M HCl was added and incubated at RT for 20 minutes. After rinsing with PBS, cells were treated with 0.1 M sodium borate ($Na_2B_4O_7$, pH 8.5) for 2 minutes at RT. Then 0.5 % BSA (bovine serum albumin) in PBST was added for 15 minutes. Anti-BrdU monoclonal antibody (BD pharmingen) in 0.5 % BSA/PBST (1:500) was added for 1 hour at RT. Cells were washed in PBST and treated with Cy2-conjugated goat anti-mouse IgG (1:100) for 30 minutes at RT. Washing in PBST was followed. DAPI diluted in PBST (1:500) was added for 10 minutes to stain whole nuclei.

Whole Genome Microarray

Dynamic and non-dynamic surfaces were prepared with linear RGD or cyclic RGD as described above. The peptide was immobilized in the density of 2 % of the surface area. Cells were allowed to migrate for 24 hours in the incubator before being collected for RNA

extraction. Cells on the fibronectin pattern were prepared with no addition of RGD ligand, but they were incubated for the equal amount of time with the non-dynamic substrates. As a reference, regularly cultured cells in tissue culture flasks were used. Cells from 70~80 % confluent monolayers with regular morphology and behavior were harvested to extract RNA. Total RNA from each sample and reference was purified using the RNeasy Mini Kit (Qiagen Inc., Valencia, CA, USA) according to the manufacturer's protocol. RNA quality check, labeling, array hybridization and image scanning were performed by the Genomics and Bioinformatics Core at the UNC Lineberger Comprehensive Cancer Center (Chapel Hill, NC, USA) and the following is a brief description of the method. The integrity of the RNA was determined using the 2100 Bioanalyzer RNA Series Ⅱ Kits (Agilent Technologies Inc., Santa Clara, CA, USA). The spike mixes of Two-color RNA Spike-In kit (Agilent Technologies Inc.) were diluted, then added directly to RNA samples prior to amplification and labeling. Total RNA samples (2.0 μg) were amplified using T7 primers to make cRNA. The cRNAs from samples were labeled with Cy5 and the reference cRNA was incorporated with Cy3. The labeled samples and reference were co-hybridized to Agilent Whole Mouse Genome Microarrays (G4122F). They were then washed and scanned on an Agilent DNA microarray scanner (Agilent Technologies Inc.). Each microarray experiment was repeated three more times per sample. The microarray images generated by the scanner were analyzed using Feature Extraction 9.5.3 software (Agilent Technologies Inc.). The raw data tables were uploaded into the UNC Microarray Database where a Lowess normalization is automatically performed to adjust the Cy3 and Cy5 channels. All microarray raw data tables are available at the UNC Microarray Database (https://genome.unc.edu/). The Hierarchical cluster image was created by GeneSpring 7 (Agilent Technologies Inc.). Using this software

the raw data was normalized by intensity dependent (Lowess) normalization (per spot and per chip). Among 41,233 genes, 1716 genes were selected by filtering the data with t-test p-value of four replicates less than 0.05 and normalized data larger than 2.5 in at least 1 of 5 sample conditions.

PCR

Total RNA from each sample and reference was purified using the RNeasy Mini Kit (Qiagen Inc., Valencia, CA, USA) according to the manufacturer's protocol. Reverse transcription was carried out on 1 μg of total RNA. Semi-quantitative real-time PCR was performed with Mastercycler (Eppendorf). Cycling parameters for PCR were as follows; denaturation at 95 °C for 30 seconds, annealing at 60–75 °C for 30 seconds, depending on the primer, and elongation at 72 °C for 5 minutes. The number of cycles was varied between 30 and 40 depending on the respective mRNA abundance. The primer sequences, annealing temperature and the concentration of $Mg^{2+}$are shown in Table 2-4. Three independent samples were analyzed for each condition and results were normalized to GAPDH.

Immunoblot Analysis / GTPase Activity Assay (Rac1)

Cells were deprived of serum for 20 hours in DMEM/BSA (0.5 %) and seeded on either a PHSRN-immobilized surface or a RGD-immobilized surface (peptide density 1 %). After 2 hours incubation, the cells on the surfaces were washed with TBS (Tris-buffered saline; 20 mM Tris buffer, pH 7.6, 150 mM NaCl, 1 mM $MgCl_2$) at 4 °C. Then 900 μL of lysis buffer (50 mM Tris, pH 7.6, 150 mM NaCl, 1 % Triton X-100, 0.5 mM $MgCl_2$ and protease inhibitors-100 mM AEBSF-HCl, 5 mM bestatin, 1.5 mM E-64, 2 mM leupeptin, 1 mM pepstatin A, 80 μM aprotinin) was added onto the cells on the surfaces. On the ice, lysed

cells were scraped off the surface substrates and collected in 1.5 mL tubes. After centrifugation for 5 minutes at 4 °C, the lysates were transferred to new tubes. For the quantification of whole protein amount in each cell lysate, Dc Protein assay (Bio-rad) was used as the manufacturer's instructions and the whole protein amount was equalized for each lysate sample. The lysates were added with PAK (p21-activated protein kinase) PBD (p21-binding domain) Agarose beads (Cell Biolabs) at 7 mg/mL and incubated at 4 °C with agitation for 30 minutes. The beads were centrifuged at 10,000 rpm for 30 seconds and the supernatant was aspirated. The beads were washed four times in a lysis buffer and then suspended in SDS-PAGE sample buffer and boiled at 95 °C for 5 minutes. The lysate and Rac1 pull-down samples were run on 15 % SDS-PAGE gel and transferred to PVDF membrane. Membranes were blocked for 1 hour using 5 % (w/v) dry non-fat milk in TBST (20 mM Tris, pH 7.4, 500 mM NaCl, 0.1 % Tween 20). Membranes were incubated overnight at 4 °C in the same buffer containing primary antibodies, mouse anti-mouse Rac1 (Invitrogen) at 1:1000 dilution. The incubation with horseradish peroxidase-conjugated secondary antibodies (goat anti-mouse IgG, Southern Biotechnology) at 1:5000 dilution for 1 hour was followed. Rac1 were detected by enhanced chemiluminescence (Thermo).

Table 2-4. Primer sequences and PCR conditions

Gene	Primer Sequences		Annealing temp (°C)	$[Mg^{2+}]$ (mM)
Itga5	Forward	5'- CTG CAG CTG CAT TTC CGA GTC TGG -3'	62	1.5
	Reverse	5'- GAA GCC GAG CTT GTA GAG GAC GTA -3'		
Itgb1	Forward	5'- GTG ACC CAT TGC AAG GAG AAG GA -3'	51.2	1.5
	Reverse	5'- GTC ATG AAT TAT CAT TAA AAG TTT CCA -3'		
Itga1	Forward	5'- CGA TGA CGC TCT GCC AAA CT -3'	57	1.5
	Reverse	5'- CCG AAG TTC TGG CAT TGG GA -3'		
Itga11	Forward	5'- CCG CCT TCC TCT GCT TCA TAC CCA T -3'	60	1.5
	Reverse	5'- GCC GCC TCT CCT CGT TCA CAC ACT C -3'		
Col1a2	Forward	5'- CAG AGT GGA ACA GCG ATT ACT -3'	55.8	1.5
	Reverse	5'- GCC CGT CTC CTC ATC CAG GTA CG -3'		
Col2a1	Forward	5'- GTG GAG CAG CAA GAG CAA GGA -3'	60.2	1.5
	Reverse	5'- CTT GCC CCA CTT ACC AGT GTG -3'		
Wnt2	Forward	5'- CTG GCT CTG GCT CCC TCT G -3'	58.8	1
	Reverse	5'- GGA ACT GGT GTT GGC ACT CTG -3'		
Wnt3	Forward	5'- CAA GCA CAA CAA TGA AGC AGG C -3'	58.2	1
	Reverse	5'- TCG GGA CTC ACG GTG TTT CTC -3'		
Wnt6	Forward	5'- TGC CCG AGG CGC AAG ACT G -3'	57.5	0.7
	Reverse	5'- ATT GCA AAC ACG AAA GCT GTC TCT C -3'		
Ctnnb1	Forward	5'- AAG GAA GCT TCC AGA CAT GC -3'	55	1.5
	Reverse	5'- AGC TTG CTC TCT TGA TTG CC -3'		
Tcf7	Forward	5'- GCC AGA AGC AAG GAG TTC AC -3'	57.2	1
	Reverse	5'- TAC ACC AGA TCC CAG CAT CA -3'		
Actb	Forward	5'- CCC CAT TGA ACA TGG CAT TG -3'	54.2	1
	Reverse	5'- ACG ACC AGA GGC ATA CAG G -3'		
Gapdh	Forward	5'- GCC CAT CAC CAT CTT CCA G -3'	57	1.5
	Reverse	5'- TGA GCC CTT CCA CAA TGC C -3'		

REFERENCES

1. Mrksich, M., *A surface chemistry approach to studying cell adhesion.* Chem. Soc. Rev., 2000. **29**: p. 267-273.

2. Chen, C.S., et al., *Geometric control of cell life and death.* Science, 1997. **276**: p. 1425-1428.

3. Fashena, S.J. and S.M. Thomas, *Signaling by adhesion receptors.* Nat. Cell Biol., 2000. **2**(12): p. E225-E229.

4. Geiger, B., et al., *Transmembrane extracellular matrix-cytoskeleton crosstalk.* Nat. Rev. Mol. Cell Biol., 2001. **2**: p. 793-805.

5. Giancotti, F.G., *Integrin signaling: specificity and control of cell survival and cell cycle progression.* Curr. Opin. Cell Biol., 1997. **9**: p. 691-700.

6. Lauffenburger, D.A. and A.F. Horwitz, *Cell migration: a physically integrated molecular process.* Cell, 1996. **84**: p. 359-369.

7. Ridley, A.J., et al., *Cell migration: integrating signals from front to back.* Science, 2003. **302**: p. 1704-1709.

8. Varner, J.A. and D.A. Cheresh, *Integrins and cancer.* Curr. Opin. Cell Biol., 1996. **8**(5): p. 724-730.

9. Giancotti, F.G. and E. Ruoslahti, *Integrin signaling.* Science, 1999. **285**: p. 1028-1032.

10. Gumbiner, B.M., *Cell adhesion: the molecular basis of tissue architecture and morphogenesis.* Cell, 1996. **84**: p. 345-357.

11. Schwartz, M.A., M.D. Schaller, and M.H. Ginsberg, *Integrins: emerging paradigms of signal transduction.* Annu. Rev. Cell Biol., 1995. **11**: p. 549-599.

12. Hynes, R.O., *Integrins: versatility, modulation, and signaling in cell adhesion.* Cell, 1992. **69**: p. 11-25.

13. Hynes, R.O., *Integrins: bidirectional, allosteric signaling machines.* Cell, 2002. **110**: p. 673-687.

14. Ylanne, J., et al., *Distinct functions of integrin alpha and beta subunit cytoplasmic domains in cell spreading and formation of focal adhesions.* J. Cell Biol., 1993. **122**: p. 223-233.

15. Carman, C.V. and T.A. Springer, *Integrin avidity regulation: are changes in affinity and conformation underemphasized?* Curr. Opin. Cell Biol., 2003. **15**(5): p. 547-556.

16. Xiong, J.-P., et al., *Crystal structure of the extracellular segment of integrin alpha V beta 3 in complex with an Arg-Gly-Asp ligand.* Science, 2002. **296**(5565): p. 151-155.

17. Sastry, S.K. and K. Burridge, *Focal adhesions: A nexus for intracellular signaling and cytoskeletal dynamics.* Exp. Cell Res., 2000. **261**: p. 25-36.

18. Zamir, E., et al., *Dynamics and segregation of cell-matrix adhesions in cultured fibroblasts.* Nat. Cell Biol., 2000. **2**(4): p. 191-196.

19. Nobes, C.D. and A. Hall, *Rho, Rac, and Cdc42 GTPases regulate the assembly of multimolecular focal complexes associated with actin stress fibers, lamellipodia, and filopodia.* Cell, 1995. **81**(1): p. 53-62.

20. Rottner, K., A. Hall, and J.V. Small, *Interplay between Rac and Rho in the control of substrate contact dynamics.* Curr. Biol., 1999. **9**(12): p. 640-649.

21. Gaidano, G., et al., *Integrin distrubution and cytoskeleton organizqtion in normal and malignant monocytes.* Leukemia, 1990. **4**: p. 682-687.

22. Bretscher, M.S., *Endocytosis and recycling of the fibronectin receptor in CHO cells.* EMBO J., 1989. **8**: p. 1341-1348.

23. Bretscher, M.S., *Circulating integrins: alpha 5 beta1, alpha 6 beta 4 and Mac-1, but not alpha 3 beta1, alpha 4 beta 1 or LFA-1.* EMBO J., 1992. **11**: p. 405-410.

24. Walsh, C.T., D. Stupack, and J.H. Brown, *G Protein-Coupled Receptors Go Extracellular: RhoA Integrates the Integrins.* Mol. Interv., 2008. **8**(4): p. 165-173.

25. Pankov, R., et al., *Integrin dynamics and matrix assembly: tensin-dependent translocation of alpha 5 beta1 Integrins promotes early fibronectin fibrillogenesis.* J. Cell Biol., 2000. **148**(5): p. 1075-1090.

26. Avnur, Z. and B. Geiger, *The removal of extracellular fibronectin from areas of cell-substrate contact.* Cell, 1981. **25**(1): p. 121-132.

27. McDonald, J.A., D.G. Kelley, and T.J. Broekelmann, *Role of fibronectin in collagen deposition: Fab' to the gelatin-binding domain of fibronectin inhibits both fibronectin and collagen organization in fibroblast extracellular matrix.* J. Cell Biol., 1982. **92**(2): p. 485-492.

28. Akiyama, S.K., et al., *Analysis of fibronectin receptor function with monoclonal antibodies: roles in cell adhesion, migration, matrix assembly, and cytoskeletal organization.* J. Cell Biol., 1989. **109**(2): p. 863-875.

29. Harris, A.K., D. Stopak, and P. Wild, *Fibroblast traction as a mechanism for collagen morphogenesis.* Nature, 1981. **290**(5803): p. 249-251.

30. Webb, D.J., J.T. Parsons, and A.F. Horwitz, *Adhesion assembly, disassembly and turnover in migrating cells - over and over and over again.* Nat. Cell Biol., 2002. **4**: p. E97-E100.

31. Hynes, R.O., *Cell adhesion: old and new questions.* Trends in Genetics, 1999. **15**: p. M33-M37.

32. Bretscher, M.S., *On the shape of migrating cells -- a `front-to-back' model.* J. Cell Sci., 2008. **121**(16): p. 2625-2628.

33. Small, J.V., et al., *How do microtubules guide migrating cells?* Nature Rev., 2002. **3**: p. 957-964.

34. Berrier, A.L., et al., *Activated R-ras, Rac1, PI 3-kinase and PKCepsilon can each restore cell spreading inhibited by isolated integrin beta1 cytoplasmic domains.* J. Cell Biol., 2000. **151**: p. 1549-1560.

35. Berrier, A.L., et al., *The integrin beta tail is required and sufficient to regulate adhesion signaling to Rac1.* J. Cell Sci., 2002. **115**: p. 4285-4291.

36. Emsley, J., et al., *Structural basis of collagen recognition by integrin alpha 2 beta 1.* Cell, 2000. **101**(1): p. 47-56.

37. Etienne-Manneville, S. and A. Hall, *Rho GTPases in cell biology.* Nature, 2002. **420**(6916): p. 629-635.

38. Itoh, R.E., et al., *Activation of Rac and Cdc42 video imaged by fluorescent resonance energy transfer-based single-molecule probes in the membrane of living cells.* Mol. Cell. Biol., 2002. **22**(18): p. 6582-6591.

39. Tadokoro, S., et al., *Talin binding to integrin beta tails: a final common step in integrin activation.* Science, 2003. **302**: p. 103-106.

40. Arias-Salgado, E.G., et al., *Src kinase activation by direct interactin with the integrin beta cytoplasmic domain.* Proc. Natl. Acad. Sci. U.S.A., 2003. **100**: p. 13298-13302.

41. Bakal, C., et al., *Quantitative Morphological Signatures Define Local Signaling Networks Regulating Cell Morphology.* Science, 2007. **316**(5832): p. 1753-1756.

42. Adams, J.C. and F.M. Watt, *Regulation of development and differentiation by the extracellular matrix.* Development, 1993. **117**(4): p. 1183-1198.

43. Frisch, S.M. and E. Ruoslahti, *Integrins and anoikis.* Curr. Opin. Cell Biol., 1997. **9**(5): p. 701-706.

44. Pierschbacher, M.D. and E. Ruoslahti, *Cell attachment activity of fibronectin can be duplicated by small synthetic fragments of the molecule.* Nature, 1984. **309**: p. 30-33.

45. Ruoslahti, E. and M.D. Pierschbacher, *New perspectives in cell adhesion: RGD and integrins.* Science, 1987. **238**(4826): p. 491-497.

46. Arnaout, M.A., S.L. Goodman, and J.-P. Xiong, *Coming to grips with integrin binding to ligands.* Curr. Opin. Cell Biol., 2002. **14**(5): p. 641-652.

47. Lutolf, M.P. and J.A. Hubbell, *Synthetic biomaterials as instructive extracellular microenvironments for morphogenesis in tissue engineering.* Nat. Biotechnol., 2005. **23**(1): p. 47-55.

48. Kao, W.J., *Evaluation of protein-modulated macrophage behavior on biomaterials: designing biomimetic materials for cellular engineering.* Biomaterials, 1999. **20**(23-24): p. 2213-2221.

49. Hersel, U., C. Dahmen, and H. Kessler, *RGD modified polymers: biomaterials for stimulated cell adhesion and beyond.* Biomaterials, 2003. **24**(24): p. 4385-4415.

50. Houseman, B.T. and M. Mrksich, *Efficient solid-phase synthesis of peptide-substituted alkanethiols for the preparation of substrates that support the adhesion of cells.* J. Org. Chem., 1998. **63**: p. 7552-7555.

51. Liu, Z. and F.W.X. Chen, *Integrin alpha v beta 3 -targeted cancer therapy.* Drug Dev. Res., 2008. **69**(6): p. 329-339.

52. LaFlamme, S.E., et al., *Integrins as regulators of the mitotic machinery.* Curr. Opin. Cell Biol., 2008. **20**(5): p. 576-582.

53. Lazarus, R.A. and R.S. McDowell, *Structural and functional aspects of RGD-containing protein antagonists of glycoprotein IIb-IIIa.* Curr. Opin. Biotechnol., 1993. **4**(4): p. 438-445.

54. Bennett, J.S., *Novel platelet inhibitors.* Annu. Rev. Med., 2001. **52**: p. 161-184.

55. Aota, S., T. Nagai, and K.M. Yamada, *Characterization of regions of fibronectin besides the arginine-glycine- aspartic acid sequence required for adhesive function of the cell- binding domain using site-directed mutagenesis.* J. Biol. Chem., 1991. **266**(24): p. 15938-15943.

56. Obara, M., M.S. Kang, and K.M. Yamada, *Site-directed mutagenesis of the cell-binding domain of human fibronectin: Separable, synergistic sites mediate adhesive function.* 1988. **53**(4): p. 649-657.

57. Aota, S., M. Nomizu, and K.M. Yamada, *The short amino acid sequence Pro-His-Ser-Arg-Asn in human fibronectin enhances cell-adhesive function.* J. Biol. Chem., 1994. **269**(40): p. 24756-24761.

58. Bowditch, R.D., et al., *Identification of a novel integrin binding site in fibronectin. Differential utilization by beta 3 integrins.* J. Biol. Chem., 1994. **269**(14): p. 10856-10863.

59. Leahy, D.J., I. Aukhil, and H.P. Erickson, *2.0 Å Crystal structure of a four-domain segment of human fibronectin encompassing the RGD loop and synergy region.* Cell, 1996. **84**(1): p. 155-164.

60. García, A.J., P. Ducheyne, and D. Boettiger, *Effect of surface reaction stage on fibronectin-mediated adhesion of osteoblast-like cells to bioactive glass.* J. Biomed. Mater. Res., 1998. **40**(1): p. 48-56.

61. Iuliano, D.J., S.S. Saavedra, and G.A. Truskey, *Effect of the conformation and orientation of adsorbed fibronectin on endothelial cell spreading and the strength of adhesion.* J. Biomed. Mater. Res., 1993. **27**(8): p. 1103-1113.

62. Grinnell, F. and M.K. Feld, *Adsorption characteristics of plasma fibronectin in relationship to biological activity.* J. Biomed. Mater. Res., 1981. **15**(3): p. 363-381.

63. Keselowsky, B.G., D.M. Collard, and A.J. Garcia, *Integrin binding specificity regulates biomaterial surface chemistry effects on cell differentiation.* Proc. Natl. Acad. Sci. U.S.A., 2005. **102**(17): p. 5953-5957.

64. Allen, L.T., et al., *Interaction of soft condensed materials with living cells: phenotype/transcriptome correlations for the hydrophobic effect.* Proc. Natl. Acad. Sci. U.S.A., 2003. **100**(11): p. 6331-6336.

65. Brodbeck, W.G., et al., *Biomaterial adherent macrophage apoptosis is increased by hydrophilic and anionic substrates invivo.* Proc. Natl. Acad. Sci. U.S.A., 2002. **99**(16): p. 10287-10292.

66. García, A.J., M.D. Vega, and D. Boettiger, *Modulation of cell proliferation and differentiation through substrate-dependent changes in fibronectin conformation.* Mol. Biol. Cell, 1999. **10**(3): p. 785-798.

67. Mardilovich, A. and E. Kokkoli, *Biomimetic peptide-amphiphiles for functional biomaterials: the role of GRGDSP and PHSRN.* Biomacromolecules, 2004. **5**(3): p. 950-957.

68. Ochsenhirt, S.E., et al., *Effect of RGD secondary structure and the synergy site PHSRN on cell adhesion, spreading and specific integrin engagement.* Biomaterials, 2006. **27**(20): p. 3863-3874.

69. Dillow, A.K., et al., *Adhesion of alpha 5 beta 1 receptors to biomimetic substrates constructed from peptide amphiphiles.* Biomaterials, 2001. **22**(12): p. 1493-1505.

70. Aucoin, L., et al., *Interactions of corneal epithelial cells and surfaces modified with cell adhesion peptide combinations.* J. Biomater. Sci. Polym. Ed., 2002. **13**: p. 447-462.

71. García, A.J., J.E. Schwarzbauer, and D. Boettiger, *Distinct activation states of alpha 5 beta 1 integrin show differential binding to RGD and synergy domains of fibronectin.* Biochemistry, 2002. **41**(29): p. 9063-9069.

72. Yeo, W.-S., M.N. Yousaf, and M. Mrksich, *Dynamic interfaces between cells and surfaces: electroactive substrates that sequentially release and attach cells.* J. Am. Chem. Soc., 2003. **125**: p. 14994-14995.

73. Yousaf, M.N., B.T. Houseman, and M. Mrksich, *Turning on cell migration with electroactive substrates.* Angew. Chem. Int. Ed., 2001. **40**: p. 1093-1096.

74. Yousaf, M.N., E.W.L. Chan, and M. Mrksich, *The kinetic order of an interfacial Diels-Alder reaction depends on the environment of the immobilized dienophile.* Angew. Chem. Int. Ed., 2000. **39**: p. 1943-1946.

75. Yousaf, M.N. and M. Mrksich, *Diels-Alder reaction for the selective immobilization of protein to electroactive self-assembled monolayers.* J. Am. Chem. Soc., 1999. **121**: p. 4286-4287.

76. Chan, E.W.L. and M.N. Yousaf, *Immobilization of ligands with precise control of density to electroactive surfaces.* J. Am. Chem. Soc., 2006. **128**: p. 15542-15546.

77. Chan, E.W.L., S. Park, and M.N. Yousaf, *An electroactive catalytic dynamic substrate that immobilizes and releases patterned ligands, proteins and cells.* Angew. Chem. Int. Ed., 2008. **47**: p. 6267-6271.

78. Chan, E.W.L. and M.N. Yousaf, *Site-selective immobilization of ligands with control of density on electroactive microelectrode arrays.* ChemPhysChem, 2007. **8**: p. 1469-1472.

79. Prime, K.L. and G.M. Whitesides, *Self-assembled organic monolayers: model systems for studying adsorption of proteins at surfaces.* Science, 1991. **252**(5009): p. 1164-1167.

80. Kahsai, A.W., et al., *Quinocarmycin analog DX-52-1 inhibits cell migration and targets radixin, disrupting interactions of radixin with actin and CD44.* Chem. Biol., 2006. **13**(9): p. 973-983.

81. Valster, A., et al., *Cell migration and invasion assays.* Methods, 2005. **37**(2): p. 208-215.

82. Klemke, R.L., et al., *CAS/Crk coupling serves as a "molecular switch" for induction of cell migration.* J. Cell Biol., 1998. **140**: p. 961-972.

83. Jiang, X., et al., *Directing cell migration with asymmetric micropatterns.* Proc. Natl. Acad. Sci. U.S.A., 2005. **102**(4): p. 975-978.

84. Kim, S., et al., *Synthetic MMP-13 degradable ECMs based on poly(N-isopropylacrylamide-co-acrylic acid) semi-interpenetrating polymer networks. I. Degradation and cell migration.* J. Biomed. Mater. Res. A, 2005. **75A**(1): p. 73-88.

85. Maheshwari, G., et al., *Cell adhesion and motility depend on nanoscale RGD clustering.* J. Cell Sci., 2000. **113**(10): p. 1677-1686.

86. Shimizu, T., et al., *Cell sheet engineering for myocardial tissue reconstruction.* Biomaterials, 2003. **24**(13): p. 2309-2316.

87. Bauer, J.S., et al., *Functional role of the cytoplasmic domain of the integrin alpha 5 subunit.* J. Cell Biol., 1993. **122**(1): p. 209-221.

88. Haubner, R., et al., *Structural and functional aspects of RGD-containing cyclic pentapeptides as highly potent and selective integrin αvβ3 antagonists.* J. Am. Chem. Soc., 1996. **118**: p. 7461-7472.

89. Thumshirn, G., et al., *Multimeric cyclic RGD peptides as potential tools for tumor targeting: solid-phase peptide synthesis and chemoselective oxime ligation.* Chem. Eur. J., 2003. **9**: p. 2717-2725.

90. Palecek, S.P., et al., *Integrin-lingand binding properties govern cell migration speed through cell-substratum adhesiveness.* Nature, 1997. **385**: p. 537-540.

91. Albini, A., V. Mirisola, and U. Pfeffer, *Metastasis signatures: genes regulating tumor-microenvironment interactions predict metastatic behavior.* Cancer Metastasis Rev., 2008. **27**: p. 75-83.

92. Padua, D., et al., *TGFβ primes breast tumors for lung metastasis seeding through angiopoietin-like 4.* Cell, 2008. **133**: p. 66-77.

93. Grinnell, F., *Focal adhesion sites and the removal of substratum-bound fibronectin.* J. Cell Biol., 1986. **103**: p. 2697-2706.

94. Turner, C.E., J.R. Glenney, and K. Burridge, *Paxillin: a new vinculin-binding protein present in focal adhesions.* J. Cell Biol., 1990. **111**: p. 1059-1068.

95. Sander, E.E., et al., *Rac downregulates Rho activity: reciprocal balance between both GTPases determines cellular morphology and migratory behavior.* J. Cell Biol., 1999. **147**: p. 1009-1021.

96. Raftopoulou, M. and A. Hall, *Cell migration: Rho GTPases lead the way.* Dev. Biol., 2004. **265**(1): p. 23-32.

CHAPTER 3

Development of Gradient Surfaces for Biology

Introduction

In this chapter the application of photo-patterning and molecular gradient surfaces in the studies of cell polarity, migration and co-culture will be discussed.

Molecular Gradients in Biology

Generating biomolecular gradients is an important signaling method for guiding cell growth, migration and differentiation *in vivo* [1-7]. In the dynamic three-dimensional environment of living tissue the spatiotemporal profile of a specific biomolecular gradient often plays essential roles in many processes such as development, inflammation, wound healing and cancer [8, 9]. During developmental processes, the concentration gradients of morphogens determine shape and size of organs and the pattern of development [10-12]. Chemoattractants direct leukocytes to correct locations in immune system [13] and proper integration of directional cue is essential for nerve growth cone guidance [14-16]. For proper biological function in all these processes, high fidelity is required and cells do this by modulating many gradient-induced signaling cascades.

However we do not understand how the gradient of those signaling molecules are generated and maintained and take direct action on cells to induce distinct cellular responses. A chemical gradient serves as a directional signal and cells respond with changes in cell

morphology and motility [17-19]. Cell migration can be induced by different mechanisms [20-22]. While chemokinesis is non-directed migration, chemotaxis is directed migration toward soluble protein and haptotaxis is directed migration toward insoluble, substrate-bound protein. There have been abundant studies in chemotaxis but much less is known about the signal transduction mechanisms in haptotaxis due to the limited availability of gradient substrate of immobilized ligand [23-25]. Therefore it is necessary to develop a general methodology to create a gradient surface of immobilized molecules. The ideal gradient surface should generate a continuous gradient with precise control of molecular density and be able to chemoselectively install the target molecule with the quantification tools available. The ability to present a ligand gradient within a selective region with temporal control is extremely useful to investigate concentration-dependent cell response.

Methods for Gradient Generation

There have been numerous efforts to develop *in vitro* methods to simulate the biological gradient [26]. The traditional *in vitro* gradient-generating methods have contributed significantly to our understanding in that the gradient signaling is highly regulated by the factors such as unique complement, concentration and spatiotemporal distribution. Biological hydrogels made from collagen, fibrin, or agarose are used to expose cells to biomolecular gradients [27, 28]. Cells or tissue are either seeded on a cell culture surface and overlaid with gel, or are homogeneously mixed with the liquid hydrogel solution prior to gelation. The gradient can be generated by a co-culture of transfected cells that release the biomolecules of interest, or molding voids within the gel and filling them with soluble biomolecules at a known concentration. The biological hydrogel method is easy and

provides cells with an environment more similar to *in vivo* tissue, but it has little control over the spatiotemporal evolution of the gradient and generates gradients with poor reproducibility.

Under a microscope, gradients can be generated by injecting a biomolecule solution into the extracellular environment of the cell culture using a micropipette [29]. This method is often used for characterizing single cell responses. Boyden chamber or transwell assay is often used for chemotaxis study [30]. A chemoattractant solution is added in the lower compartment and cells seeded on a porous membrane are placed in the upper compartment. The chemoattractant diffuses into the upper compartment and a gradient across the membrane is generated. Cells respond by migrating through the membrane to the bottom surface where they can be fixed, stained and counted to quantify the degree of chemotaxis induced by the gradient. However these traditional methods cannot control the gradient formation over space and time and have poor reproducibility.

With the rapid advance in microfabrication technology over the past 30 years, methods for creating and modulating micrometer-scale environments for cell culture have evolved [31-33]. Microfluidics as a gradient-generating method enhances the reproducibility of the gradient and the level of quantification of biological responses. The gradient can be generated by selectively adsorbing or tethering biomolecules to the cell culture surface through microfluidic channels or by connecting gradient generators. Although a gradient is better characterized using microfluidics, creating dynamic control over the shape, position, or concentration of the gradient would require a significant level of expertise and equipment. Many other methods have been also employed to generate gradients, including polymer blend [34, 35], laminar flow [36, 37], photo-patterning [38, 39], soft lithography [40], and electric fields [41, 42], but all these methods have limited success in the preparation of

molecularly defined gradients for studying the influence of gradient slope on ligand-mediated cell migration (haptotaxis).

Our gradient surface is based on a photo-labile group protected hydroquinone monolayers on gold. The deprotection of the nitroveratryloxycarbonyl (NVOC) group by UV illumination to reveal the hydroquinone group is well characterized owing to the redox activity of the resulting hydroquinones (Figure 3-1) [43, 44]. NVOC protected hydroquinone is electrochemically inactive but the yield of the deprotection reaction is obtained by cyclic voltammetry (CV) measurements of the redox active hydroquinone/quinone pair. The reaction fits with the first order rate constant of 0.11 min^{-1} [43]. The hydroquinone groups in the gradient can be electrochemically oxidized to the corresponding quinones and addition of oxyamine tethered molecules produces an oxime linkage [45]. The oxyamine groups react quickly with quinones and the different CV of the oxime redox pair from hydroquinone/quinone enables measurement of the yield of the coupling reaction (Chapter 1). The chemoselective reaction between quinones and oxyamines allows for the immobilization of any kind of biomolecules on the surface by introducing the oxyamine functional group to the molecule of interest. The use of a photo-mask with a gradient pattern when deprotecting NVOC group by UV results in hydroquinone groups residing in the corresponding gradient pattern, therefore the coupling biomolecules are also patterned in the gradient.

Photo-patterning for Co-culture Model

The photo-patterning method can be combined with microcontact printing to generate a model substrate for co-culture study. *In vivo* tissues are composed of various cell types and the interactions between them create unique microenvironments to affect cellular and

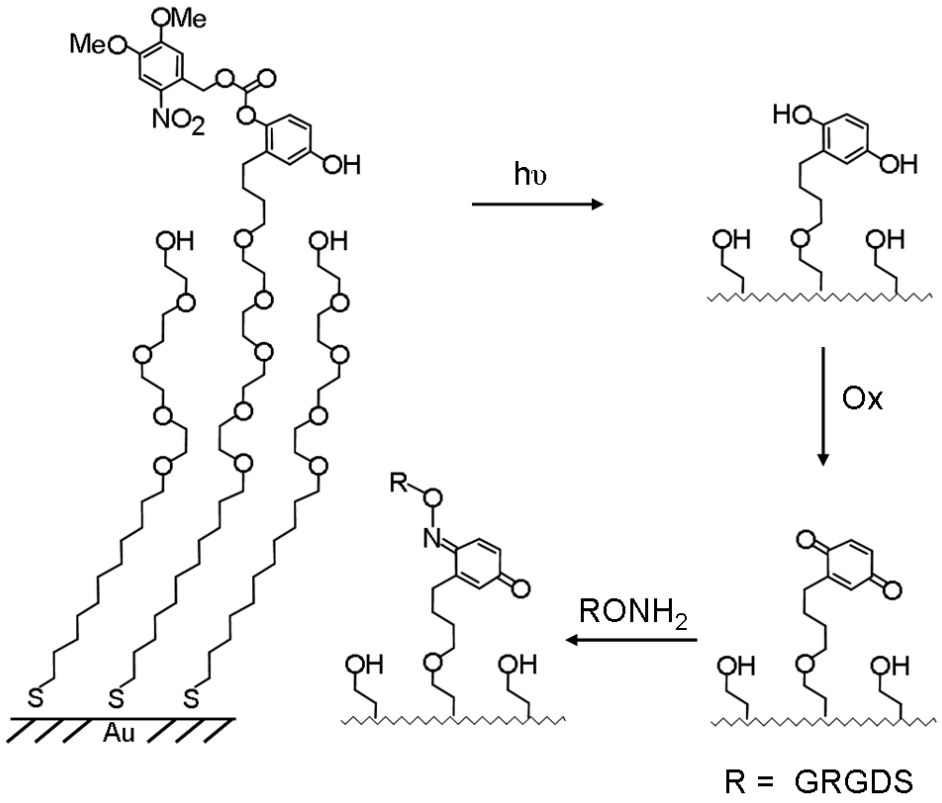

Figure 3-1**.** A photochemical strategy for patterning immobilized ligands to an electroactive self-assembled monolayer. Mixed monolayers presenting NVOC protected hydroquinone and tetra(ethylene glycol) groups are illuminated with ultraviolet light (365 nm). Photochemical deprotection of the NVOC group reveals the hydroquinone. Electrochemical oxidation of the monolayer converts the hydroquinone to the quinone. The resulting quinone monolayer can then undergo selective immobilization with aminooxy terminated peptide ligands.

physiological functions [46-50]. There have been reports proving how cell-cell interactions modulate overall cellular or tissue function. Heterotypic cell interaction between parenchymal cells and nonparenchymal neighbors alter cell growth, migration and differentiation [51]. In a co-culture of transgenic cells and wild type cells the release of regulatory signals by wild type cells helps the transgenic cells restore the cellular function [52]. Also lineage commitment of mesenchymal progenitor cells is influenced by cell signaling from adjacent cells [53]. Therefore creation of model systems to study heterotypic cellular interactions would benefit area of research such as stem cell differentiation, nerve regeneration, cancer cell transformation, immune mechanisms and tissue engineering.

There have been approaches of various co-culture systems to mimic intercellular interactions. Starting from random mixing of different cell lines, a co-culture model has been developed to have more functional and elegant control. They include thermo responsive polymer surfaces [54, 55], soft lithography generated substrates [56-58], extracellular matrix (ECM) components deposited layers [59] and three-dimensional scaffold [60]. As many complex factors (growth factors, ECM guidance and soluble signaling molecules, etc.) are involved in cell-cell communication *in vivo* rather than simple cell-cell contact, it would be extremely beneficial if we can mimic such complexity in a co-culture system.

For studies of co-culture systems, self-assembled monolayer (SAM)-based substrates which efficiently pattern different cell types with spatial control by combining microcontact printing and photo-patterning were generated. These substrates possess the ability to present biological ligand molecules on the surface and thus biospecific interactions between ligand and cell surface receptors can be studied. The photo-patterning also enables ligand molecules

to be immobilized in the gradient in the presence of cells and this feature adds microenvironmental complexity to the co-culture system.

Results and Discussion

Synthesis of Nitroveratryloxycarbonyl (NVOC) Protected Hydroquinone Alkanethiol

Hydroquinone alkanethiol protected by a photo-labile nitroveratryloxycarbonyl group (**3e**) was synthesized by the scheme shown in Figure 3-2. Deprotonation of di-tetrahydropyran-hydroquinone (**1h**) with *t*-butyllithium followed by the addition of dibromohexane provided the di-tetrahydropyran-hydroquinone-hexylbromide (**3a**). Addition of sodium hydride to deprotonate tetra(ethylene glycol)alkanethiol-trityl (**1j**) followed by addition of the bromide (**3a**) afforded the conjugate (**3b**). The tetrahydropyran groups were deprotected with mixture of acetic acid, water and THF (**3c**). The addition of 6-nitroveratryloxycarbonyl chloride with 4-dimethylaminopyridine installed the NVOC group on the hydroquinone (**3d**). Deprotection of the trityl group with TFA provided the NVOC group protected hydroquinone alkanethiol (**3e**).

Ligand Slope, Density and Affinity Direct Cell Polarity and Migration

To generate ligand defined gradients a substrate presenting a mixed monolayer of NVOC protected hydroquinone (20 %) and tetra(ethylene glycol) (80 %) was prepared. After ultraviolet (UV) illumination through a photo-mask with a dumbbell gradient pattern for 30 minutes, the monolayer substrate was electrochemically activated by applying an oxidative potential at 750 mV for 10 seconds. As shown in Figure 3-3, the immobilization of the ligand

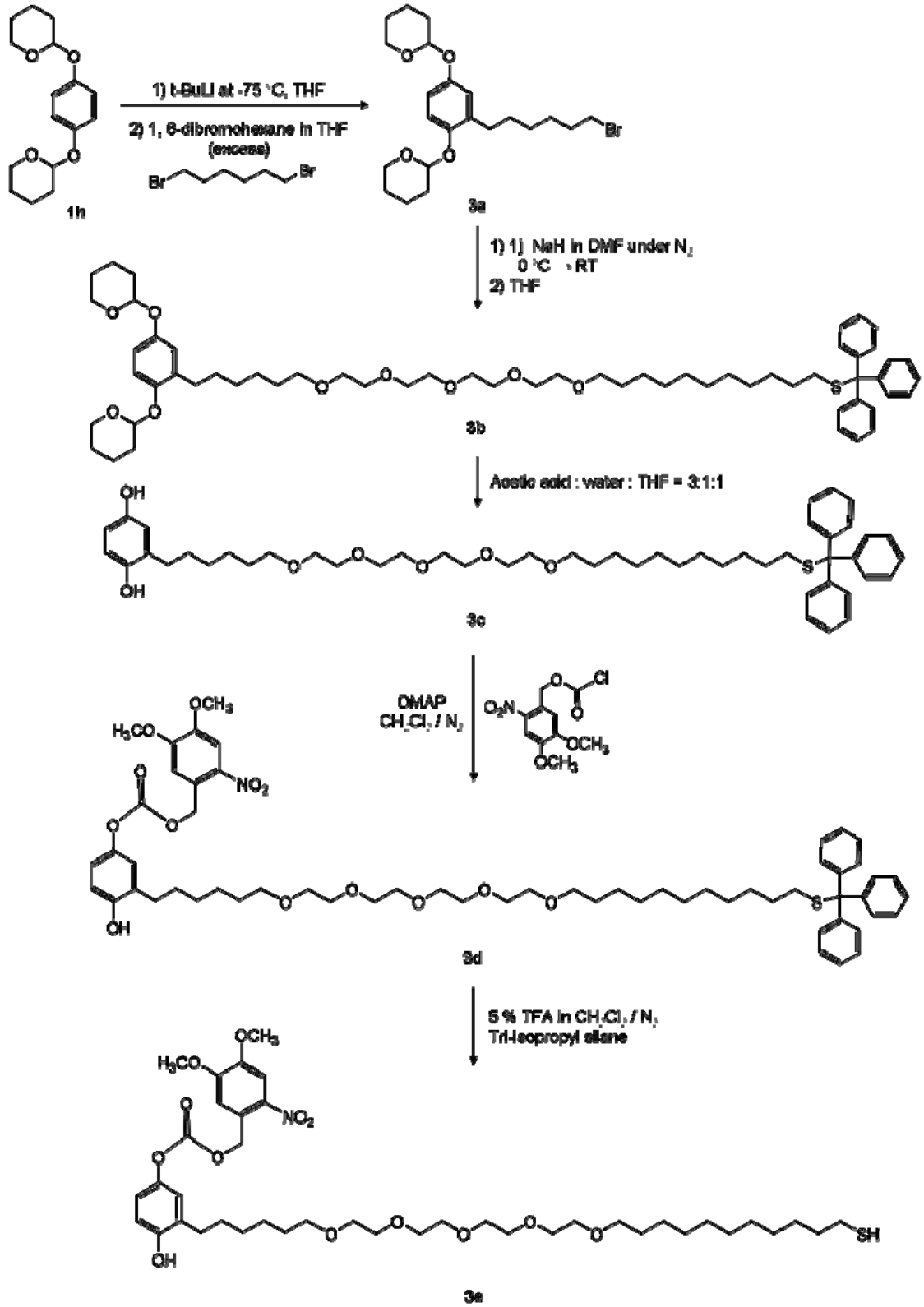

Figure 3-2. Synthetic route to nitroveratryloxycarbonyl (NVOC) protected hydroquinone alkanethiol (**3e**).

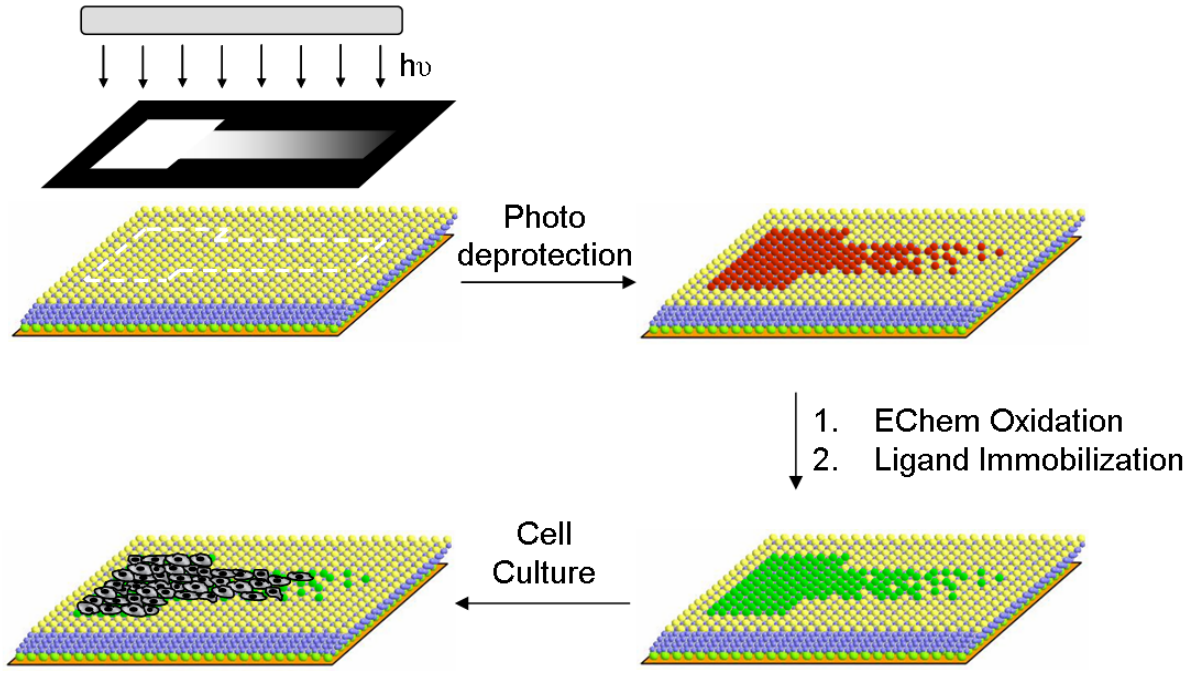

Figure 3-3. A strategy for generating gradients of immobilized peptide ligands for attached cell culture. UV Illumination of the NVOC protected hydroquinone monolayers through a gradient photo-mask reveals the hydroquinone in selective regions on the monolayer. Electrochemical oxidation of the hydroquinone monolayer to the quinone permits selective immobilization of soluble peptide ligands to the patterned gradient surface. Addition of cells to the resulting peptide gradient surface mediates cell attachment and migration on a molecularly defined surface.

creates a gradient surface of biomolecules and this substrate is compatible with regular cell culture. We first immobilized soluble rhodamine oxyamine (50 mM in methanol, 2 hours) in order to characterize the surface modification by fluorescence microscopy. Direct visualization of the monolayer by fluorescence microscopy was prohibited due to quenching of the fluorescence by the gold film [61]. Therefore, in order to visualize the surface we transferred the monolayer to a transparent medium where we could then characterize the photo-patterning and subsequent immobilization by fluorescent microscopy. Figure 3-4A shows the optical micrographs of various photo-masks used in generating the dumbbell gradients. Figure 3-4B shows fluorescent images of rhodamine oxyamine conjugated to the quinone monolayer after the photo-patterning. The immobilization of rhodamine oxyamine in selective region results in a gradient pattern identical to that of the photo-mask. This result confirms that the surface chemistry is compatible with the use of photo-mask to generate complex ligand defined gradients on monolayer surfaces.

This photochemical strategy was used to pattern RGD ligands in gradients for attached cell culture to determine the relationship between slope and ligand density on cell adhesion and migration. A mixed monolayer presenting 1 % NVOC protected hydroquinone and 99 % tetra(ethylene glycol) groups was prepared. Illumination through various dumbbell gradient photo-mask patterns followed by electrochemical oxidation converted the surface to gradient regions of reactive quinone monolayer. Selective immobilization of oxyamine-RGD (20 mM in PBS for 4 hours) to the quinone monolayer generated the peptide gradients on the surface. Addition of Swiss 3T3 fibroblasts resulted in cell attachment to the dumbbell gradient patterns. The cells initially attached to the higher peptide density regions of the gradients. The monolayer substrates were then placed in serum containing media to allow cell growth

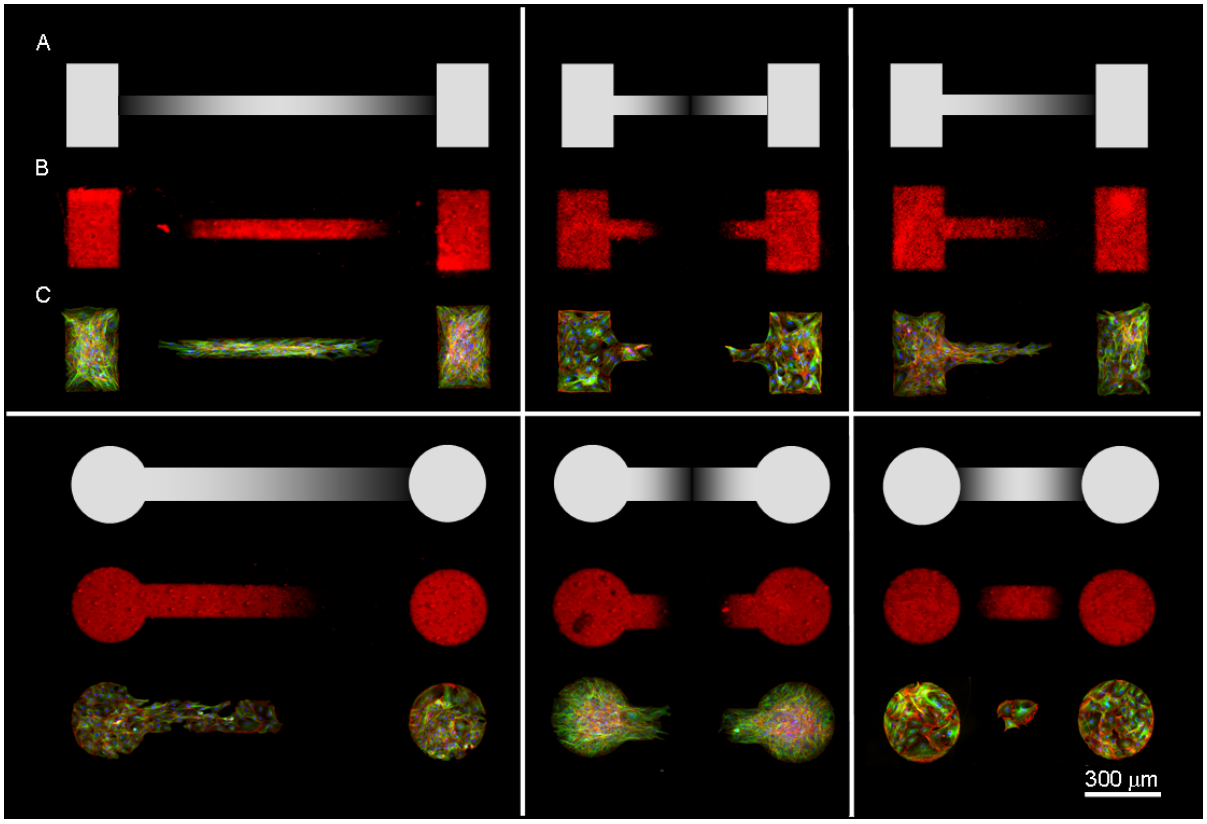

Figure 3-4. Representative images for the photo-patterning of fluorescent molecules and peptide ligand mediated cell attachment and migration on molecularly defined gradients. A. Optical micrographs of the photo-masks used in generating several dumbbell gradient patterns with varying slopes. B. Fluorescent images of surface immobilized rhodamine oxyamine after the photo-patterning. C. Fluorescent images of Swiss 3T3 fibroblasts on linear-RGD ligand gradients. Cells were allowed to attach, proliferate and migrate on the gradients until they stopped moving and then fixed and stained for actin (red), tubulin (green), and DNA (blue).

and migration. The cells proliferated and moved down the gradients and then stopped at their final positions due to the lack of peptide ligand density to support further adhesion and migration. Figure 3-4C shows representative fluorescent images of fixed cells on various RGD immobilized gradients. The images show that the adherent cells are completely confined within the patterns demonstrating that the use of UV light and electrochemical oxidation did not damage the monolayer surfaces which would lead to nonspecific cell attachment. Furthermore, cell attachment on these peptide gradients clearly depends on the density and slope of immobilized ligands. As the peptide density decreases along the gradient a minimum density is reached below which cell adhesion cannot be supported. Finally, the relative positions at which cells attached along both sides of the gradients are remarkably similar on most of the symmetrical patterns. This result implies that both the photo-patterning and the surface chemistry that control the peptide immobilization are well defined on these gradient surfaces. As controls we immobilized a scrambled peptide-oxyamine (GRD-ONH_2) to the gradient surfaces and no cells attached. We also added a soluble competing RGD peptide (1 mM for 30 minutes) to the media and all the adhered cells on gradients detached indicating a biospecific attachment between the cells and the surface.

Whether ligand density alone or the combination of slope and ligand density governs cell migration is intriguing. If cell migration is solely based on the underlying ligand density, the adherent cells would migrate down the gradient until the ligand density is insufficient for supporting cell attachment. The minimum ligand density for cell attachment over long periods of time (equilibrium position) would therefore be similar on all the gradients. In order to determine the peptide density for cell attachment along the gradient, we used an image analyzing software (ImageJ) to first obtain a density profile of the gradient based on

the pixel intensity of the photo-mask. Figure 3-5A shows the optical micrographs of the photo-masks. Figure 3-5B shows the fluorescent images of the attached cell culture on RGD immobilized dumbbell gradients generated by the photo-mask shown in Figure 3-5A. Figure 3-5C shows a plot for the relative density with respect to the distance along the gradient generated from ImageJ. To extrapolate the density along the gradient from this plot, the maximum peptide density was assumed as 2.7×10^4 molecules/μm^2 (2.7×10^{12} molecules/cm^2) based on a 1 % NVOC hydroquinone monolayer that has been completely modified to the peptide ligand on the surface. The ligand density at 1 % NVOC hydroquinone was determined based on integration of the area under the oxidative or reductive waves corresponding to the hydroquinone monolayer after the photo-deprotection of monolayer presented only the NVOC hydroquinone groups. By aligning the density plot with the patterned cells, the minimum ligand density for supporting cell adhesion along the gradient was precisely determined. Interestingly, the data show that the minimum density varies on each gradient. This result suggests that cell migration is not solely dependent on density of surface-bound ligands.

We next examined how the slope of ligand presentation may play a role in affecting how, where and when cells migrate. By allowing the cells migrate from a higher density of ligand toward a lower density on gradients with different slopes, a correlation between the angle of the slope and minimum ligand density for cell attachment on the gradient can be established. For these experiments, gradient patterns with various slopes on a photo-mask were generated by systematically varying the length of the gradients. To calculate the slope arbitrary values for both the density and distance along the gradient obtained from ImageJ were used. Then the peptide gradients with slopes ranging from -1 (the shallowest) to -8 (the

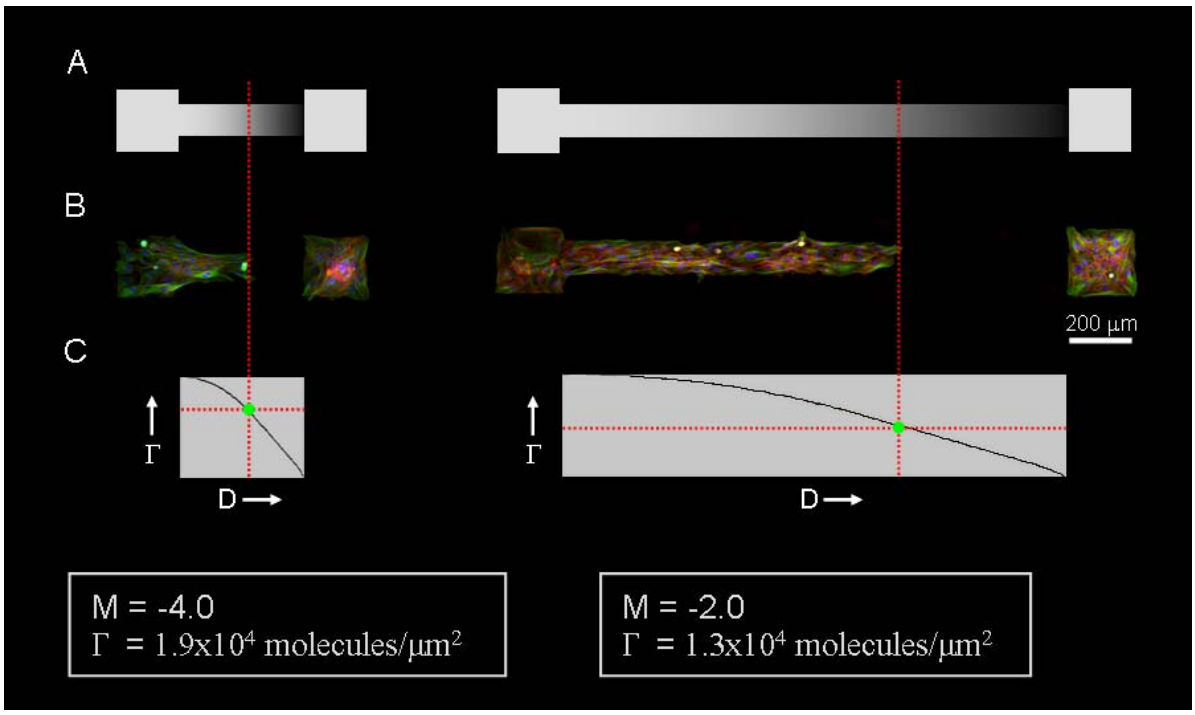

Figure 3-5. Analysis of the slopes and ligand densities along various linear-RGD ligand gradients to determine their influence on cell adhesion and migration. A. Optical micrographs of the different gradient photo-masks. B. Fluorescent images of fixed and stained cells after they stopped migrating on peptide gradients of various slopes. C. A plot of ligand density versus distance along the gradient was generated from the photo-mask shown in A using ImageJ. The plot is aligned perpendicularly with the patterned cells in order to determine the minimum density required to support cell migration on a peptide gradient.

steepest) were prepared for cell culture. Figure 3-6 shows a plot for the dependence of minimum ligand density for cell attachment of various cell-types on the slopes of gradients. The data show that the cells on steeper slopes terminate migration at higher peptide density when compared to the cells on shallower slopes. This result suggests cells that migrate on linear RGD defined gradients can sense and therefore respond accordingly to the subtle changes due to ligand presentation on the surface.

To establish a connection between the underlying gradient and intracellular protein activation, the migration experiment was repeated using focal adhesion kinase-null (FAK-/-) cells derived from mouse embryos. FAK is a non-receptor protein tyrosine kinase localized at focal adhesions and is essential for integrin-stimulated cell migration [62]. Focal adhesions are sites found at the plasma membrane that mechanically link and anchor the cytoskeleton to integrin clusters and the extracellular matrix. These are also centers for complex biochemical signaling for many pathways critical for cell function [63]. Deletion of FAK expression has been shown to impair cell migration [64]. Unlike the Swiss 3T3 fibroblasts, FAK-null cells on linear RGD gradients migrated to the same ligand density at equilibrium regardless of the slopes (red line). A separate experiment with wild-type (FAK+/+) cells exhibited similar dependence of ligand density on the slopes as the Swiss fibroblasts (black line). This result suggests that focal adhesion kinase may be critical in sensing ligand presentation during cell migration.

As further evidence that ligand affinity also plays a role in cell migration, the surface immobilized with cyclic RGD was used to compare the cell migration equilibrium positions with linear RGD peptide gradients (blue line). At steeper slopes the FAK+/+ cells required more cyclic RGD ligand density than for linear RGD. This result implies that although the

affinity for cyclic RGD is greater than that for linear RGD the steepness of the gradient across a cell length alters the requirements for ligand density for cell migration. These are the first results to compare ligand affinity, density and slope for cell migration studies.

Figure 3-7 shows an illustration summarizing the data obtained from Figure 3-6 for linear RGD immobilized surfaces. Upon addition of FAK+/+ and FAK-/- cells to the surface, both cell lines initially attached to the region of the gradient that presents the highest linear RGD ligand density. The cells migrated and proliferated at this high density region until they became contact inhibited and then started to migrate down the gradient. For the FAK+/+ cells there is no impairment of their cell migration machinery and are therefore able to sense the change in ligand density across their length and tune their position along the gradient. FAK+/+ cells require a higher ligand density to support adhesion on steep gradients and a lower ligand density on shallow gradients. In contrast FAK-/- cells that have their focal adhesions severely compromised due to the absence of the critical focal adhesion kinase were unable to sense the peptide gradient and positioned themselves to the same density irrespective of slope. For the FAK+/+ cells the severity of the change in ligand density at steep slopes induce the cells to require more ligands to support adhesion. On shallow slopes the cells are able to migrate to regions with a much lower ligand density indicating fewer ligands are required to support cell function and adhesion. These results show that a cell has the ability to modulate its behavior by precisely determining the change in ligand density and affinity from its leading to trailing edge. The ability for a cell to modulate its internal nano-architecture to sense and respond to the surface environment is critical for regulating directional movement.

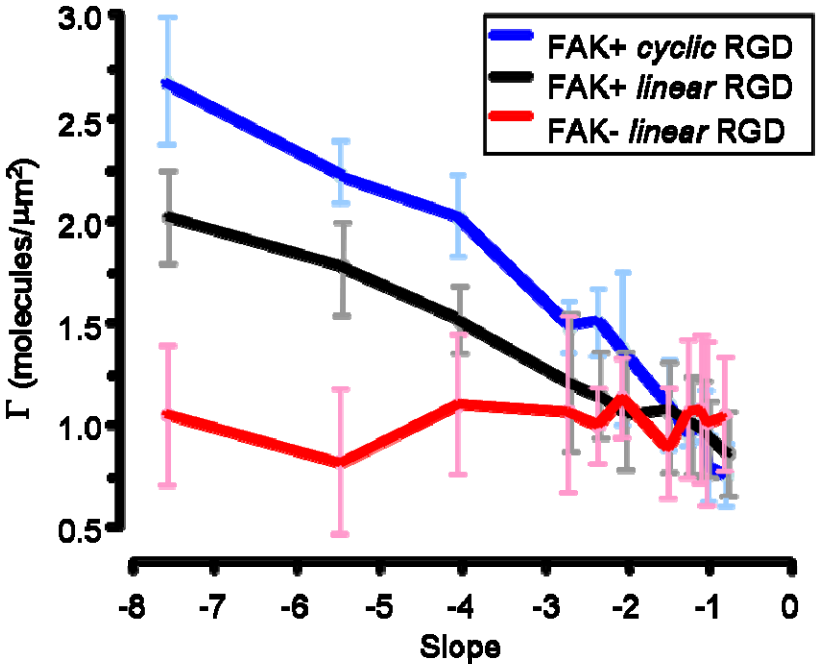

Figure 3-6. Relationship between ligand density, ligand affinity and gradient slope for two different cell-types. Each data point represents an average from four separate sets of experiments. The cells over time position themselves to varying ligand density depending on the slope of the gradient. Mouse embryonic fibroblasts (FAK+) cells re-adjust their position depending on the slope and affinity of peptide ligand while FAK-null fibroblasts (FAK-) which have a focal adhesion defect, position themselves to the same density irrespective of slope and ligand affinity.

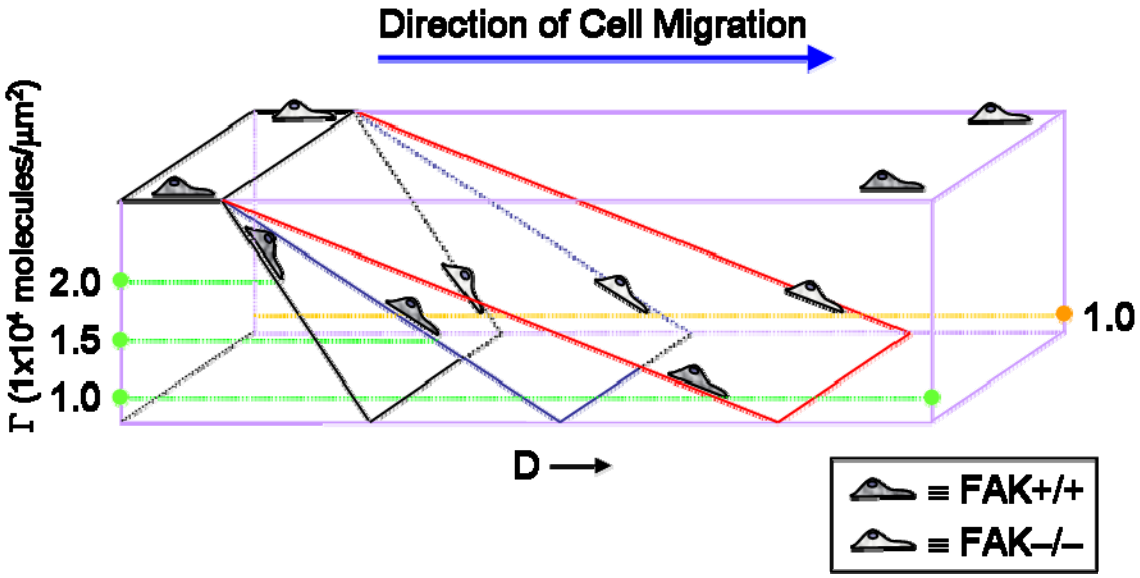

Figure 3-7. An illustration describing the dependence of ligand density (linear RGD) on the slopes of gradients for FAK+/+ cells and FAK-/- cells. The cells initially attach to the higher density region of the gradient pattern (left) and proliferate and migrate down various slopes to their final equilibrium position over time. The migration of FAK+/+ cells is governed by a combination of ligand density and slope of the gradient. The cells migrate to different ligand density along the gradient and therefore are able to modulate their position according to the steepness of the slope. In contrast, the migration and final position of FAK-/- cells depends only on the ligand density. These cells move to the same ligand density regardless of slope.

This methodology was extended to study single cell polarization. The ability for a cell to polarize and therefore generate asymmetry within itself due to external factors is critical for a range of biological processes [65]. The role of the underlying adhesive environment and cell-cell interactions is critical to establish cell polarity but is not well understood due to a lack of studies on molecularly well-defined surfaces. In order to study the underlying surface chemistry requirements for cell polarity, cells were confined to small pattern gradients where the cells attach and become polarized due to the underlying linear RGD ligand gradient but are not able to migrate (Figure 3-8). The most conclusive method to determine cell polarity is to measure the vector between the cell nucleus, concentrated Golgi and centrosome. The polarity of a cell can be experimentally observed and measured through the systematic reorientation and alignment of these organelles, which can be visualized using fluorescent dyes to map the direction of polarity [66]. Giantin, a protein found in the membrane of the Golgi apparatus cisternae was chosen as a marker for that organelle [67]. As can be seen in the series of fluorescent micrographs in Figure 3-8, the adherent cells adopt a morphology in which the nucleus is located approximately in the center of the cell. By determining the alignment vector of the Golgi apparatus relative to the nucleus and centrosome, we found no consistent directional polarity on the non-gradient square patterns for many cells (n = 18). In fact, almost all cells had a diffuse Golgi around the nucleus, a strong indicator of no polarity. For gradient square patterns (Figure 3-8, middle and right columns) the cells are polarized towards the higher density linear RGD regions as shown by the relative positions of the nucleus and the concentrated Golgi apparatus. Statistical analysis of the three patterns show the polarity vector for cells on the gradients is directed to the higher density and therefore more adhesive region of the pattern, whereas there is no net vector in any direction on the

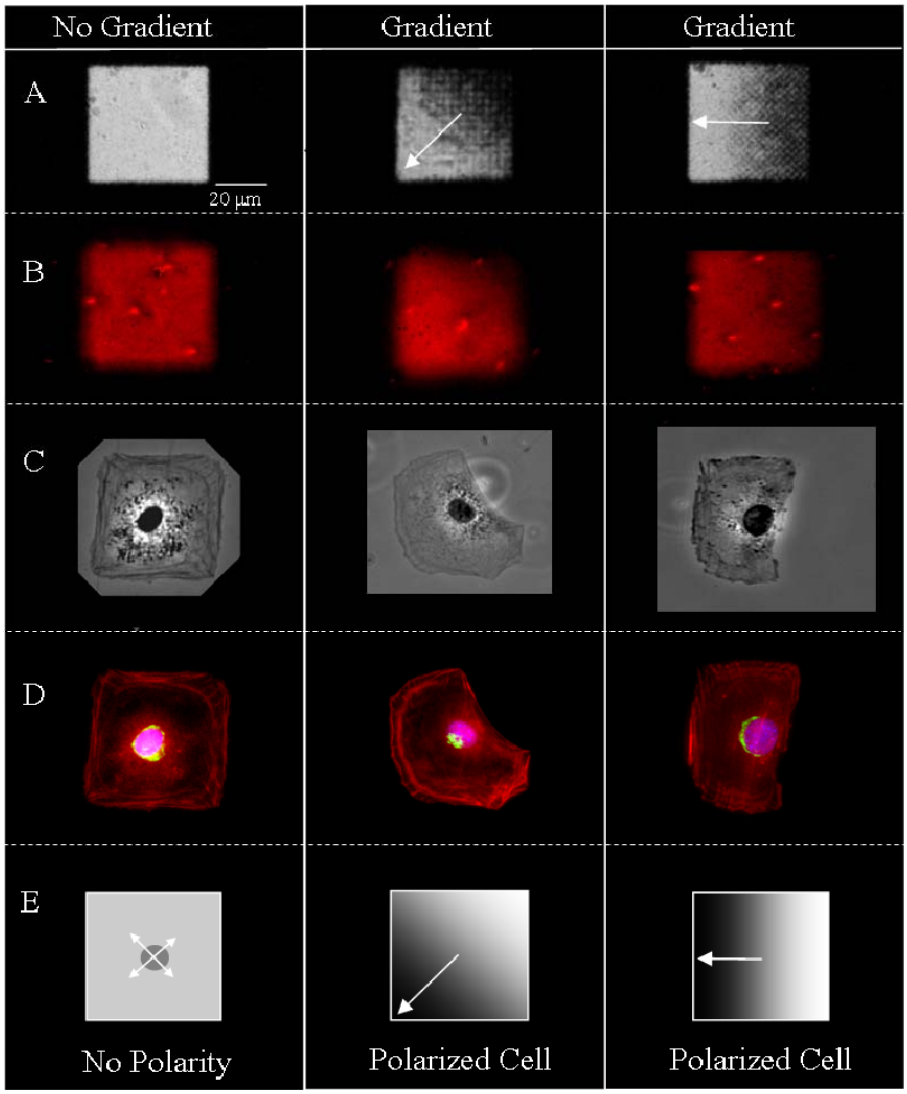

Figure 3-8. Single cell fluorescent images of polarized cells on small pattern linear-RGD immobilized gradients. A. Optical micrograph of the microfiche photo-mask used for the photo-deprotection of the NVOC-hydroquinone to generate a surface gradient. B. Fluorescent image of immobilized rhodamine-oxyamine to the surface generated by the gradient photo-mask. This fluorescent gradient is used to show that the ligands immobilized on the surface have the same slope as the photomask. C. Representative phase contrast micrographs of 3T3 Swiss Albino mouse fibroblast adhered to non-gradient and gradient patterns of immobilized linear RGD peptide. D. Fluorescent images of the cells stained for actin (red) nuclei (blue) and Golgi apparatus (green) to determine the direction of cell polarity. The vector between the concentrated Golgi with respect to the nucleus and centrosome determine directional cell polarity (E). For the non-gradient pattern (left column), the diffuse distribution of the Golgi surrounding the nucleus indicates the cell is not polarized. For cells on the gradient surfaces (center and right columns) the net vector points consistently towards the higher density adhesive regions. These results show the underlying peptide ligand gradient directs cell polarization.

non-gradient or uniform square pattern (Figure 3-8E). These results clearly show in the absence of cell-cell interactions a cell can be directly influenced by its surface gradient environment to polarize towards the higher density ligands. Interestingly, when a higher affinity ligand (cyclic RGD) is immobilized to the gradient patterns no net directional polarity occurred. We hypothesize the affinity of the ligand and the spatial presentation of the ligands combine to govern the ability for the cell to polarize.

Spatio-Temporal Control of Cell Morphing on Dynamic Pattern and Gradient Surfaces

We designed our substrates to express RGD ligands in a continuous gradient in the presence of the cells in selected region. First we generated a pattern by microcontact printing hexadecanethiols on a gold surface (Figure 3-9). The remaining bare gold was backfilled with tetra(ethylene glycol)- and NVOC-protected hydroquinone-terminated alkanethiols (99:1 ratio) in order to render the surface resistance to the non-specific adsorption of proteins (see Chapter 1). The UV light was irradiated to the monolayers through the photo-mask for 10 minutes. The NVOC groups underneath the transparent pattern of the photo-mask are cleaved to expose hydroquinone groups. The use of a photo-mask with gradient design can produce corresponding gradient pattern of hydroquinones on monolayers. The addition of cells onto the monolayers resulted in the attachment of the cells exclusively on the hydrophobic microcontact printed pattern. In the presence of the cells on the surface, a mild electrochemical potential (750 mV for 10 seconds) was applied to oxidize hydroquinones to quinones. The subsequent addition of soluble RGD-oxyamine (20 mM for 1 hour) installed the adhesive ligand molecules on the monolayers as oxime adducts. The oxidative potential applied to the surface and the addition of soluble RGD to the substrate does not affect

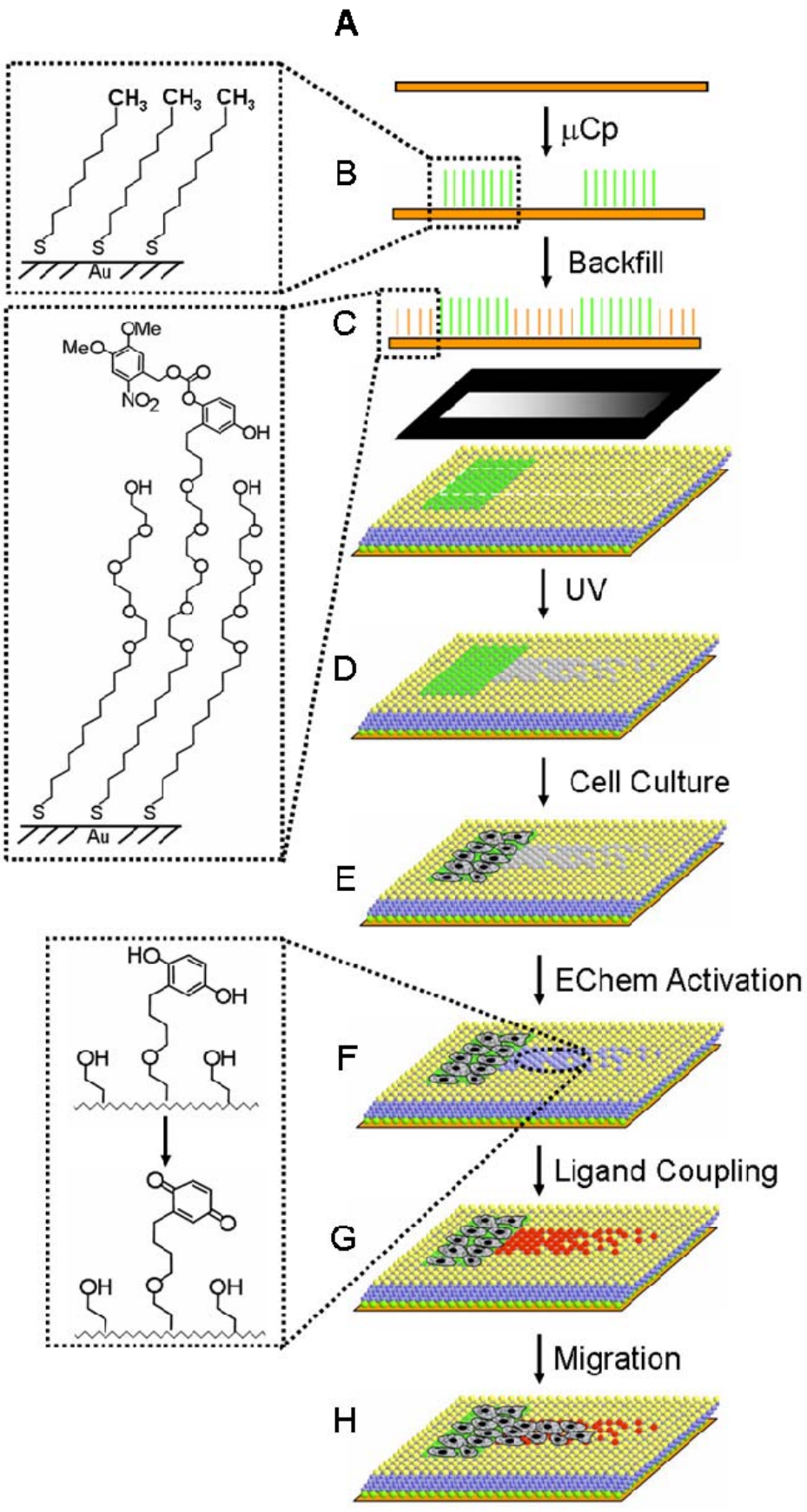
A
B
C
D
E
F
G
H
μCp
Backfill
UV
Cell Culture
EChem Activation
Ligand Coupling
Migration
Au
Au

Figure 3-9. A strategy for the spatial and temporal control of cell migration on dynamic gradients. A. An optically transparent gold coated glass substrate was fabricated by depositing a layer of titanium (3 nm) followed by a layer of gold (12 nm) onto microscope glass cover slips. B. Hexadecanethiols were microcontact printed in order to generate a hydrophobic pattern on the gold coated substrate. C. The remaining bare gold region was backfilled with a mixed monolayer presenting both the NVOC hydroquinone and tetra(ethylene glycol) groups. D. UV illumination through a photo-mask with gradient pattern deprotected the NVOC groups to reveal the hydroquinone in selective region on the monolayer surface. E. Cells were then added onto the substrate, and adhered exclusively to the hydrophobic patterns. The adherent cells proliferated but remained confined within the patterns. F. The monolayer substrate was then applied by a mild oxidative potential to convert the unreactive hydroquinone monolayer to the corresponding reactive quinone. G. Addition of soluble adhesive peptide (RGD) oxyamine installed the peptide to the quinone monolayer via a stable oxime formation. The oxime conjugate subsequently converted the surface property from inert to cell adhesive. H. As the adherent cells near the edge of the patterns sensed the changes in the microenvironment, they initiated migration toward the peptide defined gradient generated by the photo-patterning.

integrity of monolayers or viability of the cells. If the cells confined in the first pattern recognize the RGD ligands in the photo-pattern, they would initiate migration towards the second pattern. This is similar to the dynamic surface in Chapter 2. The difference is that the RGD ligand is patterned on the surface, therefore the cells on the initial geometry would morph to the confined photo-patterned geometry. Also a gradient of RGD is important factor for the cell migration.

Figure 3-10 shows representative fluorescence microscopy images of the cells migrating from initial pattern to photo-generated ligand patterned area. As the cells in a round pattern sense RGD in the adjacent photo-patterned rectangle the migration is directed and is shown as the two patterns merging in Figure 3-10A. The left half of Figure 3-10B shows a dumbbell shape photo-mask with gradient that was used to generate a photo-pattern across the microcontact printed line pattern. When the RGD gradient was applied on the photo-pattern, the cells were observed to migrate up to a certain density of the ligand on the surface. This implies that the cells have a gradient sensing mechanism and the density of the RGD molecules along the gradient is directly related to the decision of motility on the surface. The observation in this experiment was consistent with the studies of ligand slope and density of previous section.

We also tested if cells are able to "hop" over certain distances to achieve migration by designing the substrate in which the microcontact printed pattern and photo-pattern were not in contact (Figure 3-10B, right). Interestingly, morphing from the first pattern to the second was observed in that the cells were able to bridge to the ligand presenting area. At this point it is not clear whether the cells were able to sense adhesive ligand from a distance (within 50 μm) to direct migration or they happened to discover the RGD region by random checking.

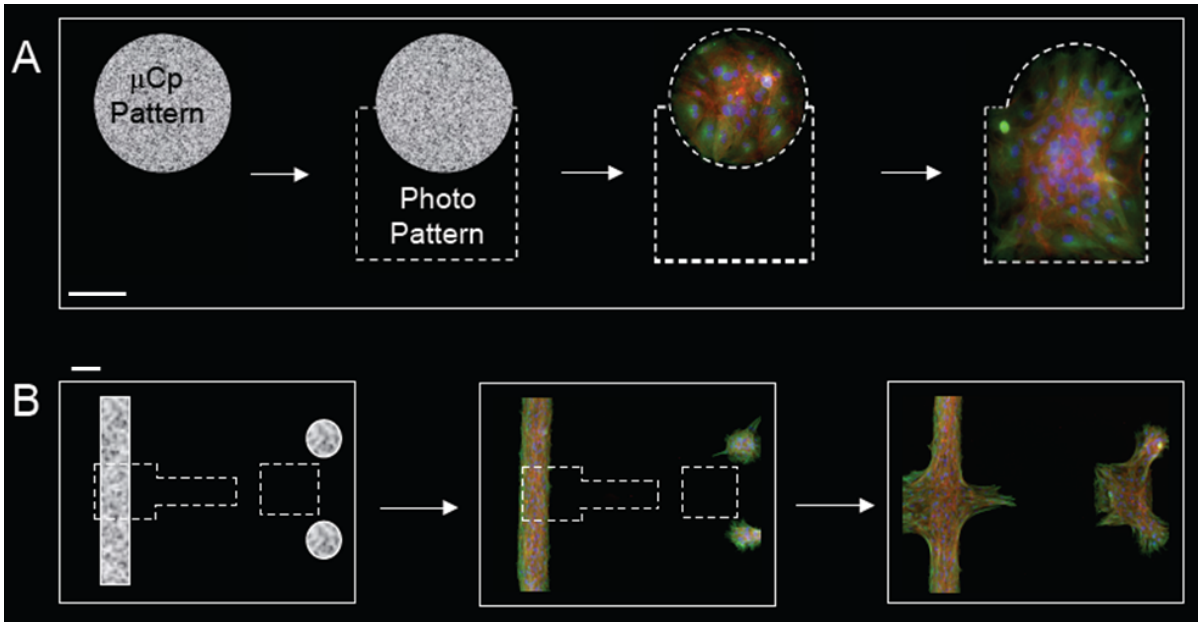

Figure 3-10. Fluorescence micrographs showing morphing in which patterned cells migrated toward photo-patterned ligand area. A. A photo-mask of rectangle was used to generate a photo-pattern of hydroquinone monolayers that overlapped the microcontact printed circular pattern. The photo-patterned region was completely inert to cell attachment, resulting in 3T3 Swiss albino cells adhering exclusively to the hydrophobic circular pattern generated by microcontact printing. Electrochemical oxidation and addition of RGD oxyamine immobilized adhesive ligand onto the photo-patterned monolayers. Cell migration occurred by adhesive interaction between cell surface receptor integrins and RGD. Scale bar 60 μm. B. Left. In the presence of the cells on microcontact printed line pattern, gradient of RGD ligand was generated in dumbbell shape across the line pattern by photo-patterning. Cells migrated accordingly by sensing underlying ligand gradient. Right. Photo-generated square pattern was located 50 μm apart from the microcontact printed cell pattern. The cells were still observed to migrate toward the square pattern which supported RGD presentation. Scale bar 200 μm.

To investigate how the cell migration is affected by gradient factors, we designed a substrate in which two RGD gradient patterns with different slopes were positioned across the microcontact printed line patterns (Figure 3-11). The time-lapse images of the cells were recorded over 51 hours at 37 °C and 5 % CO_2. In this experiment we can test whether the cells tend to migrate up or down the gradient and how fast they migrate according to the underlying gradient of ligands. As shown in Figure 3-11, when the cells move to the head parts of the dumbbell shaped pattern the ligand density underneath is almost constant and the highest. The cells moving in the direction of the red arrows are migrating toward decreasing ligand density (down the gradient). In contrast cells along the blue arrows are migrating in the direction of increasing ligand density (up the gradient).

The cells initially confined in the microcontact printed lines show active sampling toward RGD dumbbell patterns by throwing out their filopodia and lamellipodia. In 10 to 15 hours, cell fronts were seen to move toward RGD gradient patterns. The confluent layer of the cells on the microcontact printed region did not lose cell to cell interactions and the joined cells migrate collectively rather than migrating individually. In 51 hours cells were found to fill up the dumbbell patterns completely. The migration of the cell front was measured in each designated region (A-G) and the plot of migration over time is shown in Figure 3-12.

The cells in zone D are moving to the highest density of RGD and the migration was completed at an early stage (20 hours). The cells in zone A are moving from the highest density down the gradient's steep slope and accomplished 70 % migration in 20 hours and 100 % in 35 hours. The cells in zone E are migrating from a high density of RGD to the low density along a gentle slope. They reached 100 % migration within 35 hours although they

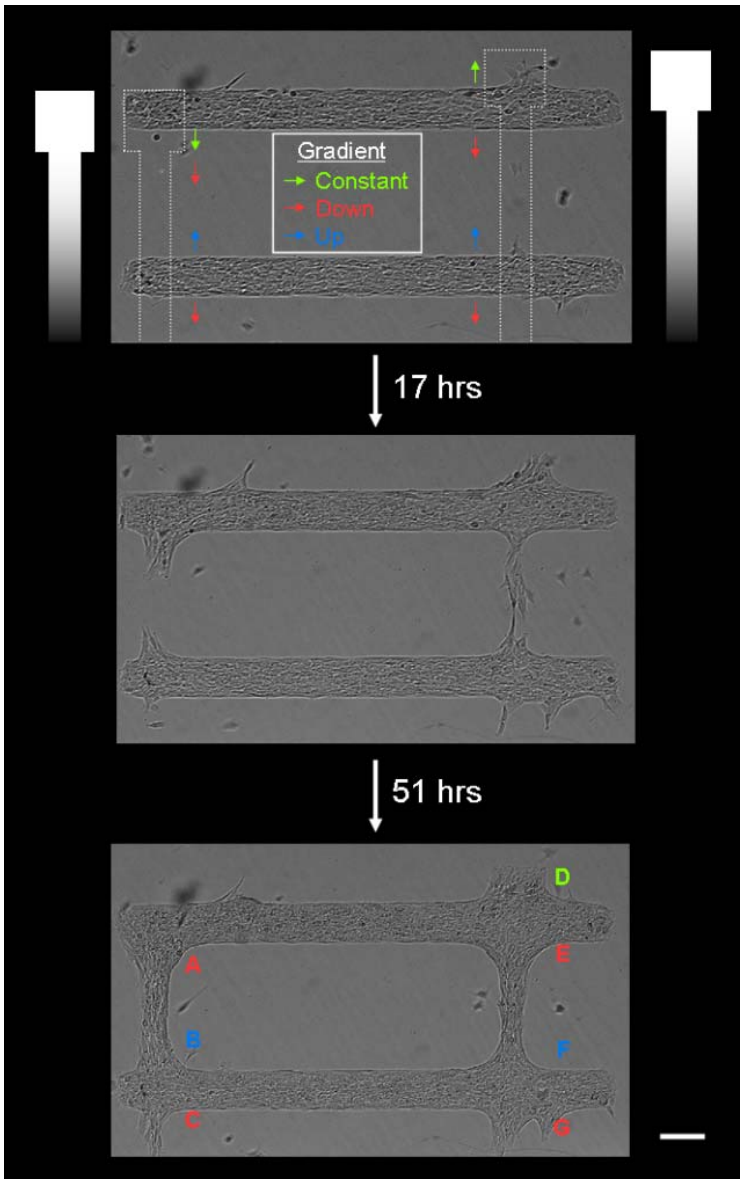

Figure 3-11. Time-lapse micrographs showing the migration of patterned cells toward photo-generated RGD peptide gradients. Two dumbbell shape gradients of RGD with different slope were generated across the micro-contact printed line patterns of the cells. Within 17 hrs the cells started to migrate actively toward RGD gradient patterns and the dumbbell gradient patterns were seen to be filled with migrating cells in 51 hrs. We can analyze migration according to the direction of the gradient. The RGD density in the green arrow zone is constant and the highest. The cells moving in the direction of the red arrow would be experiencing the density of the RGD decreasing while the cells in the blue arrow zone are moving up the gradient of RGD. For further analysis each zone was labeled A-G. Scale bar 200 μm.

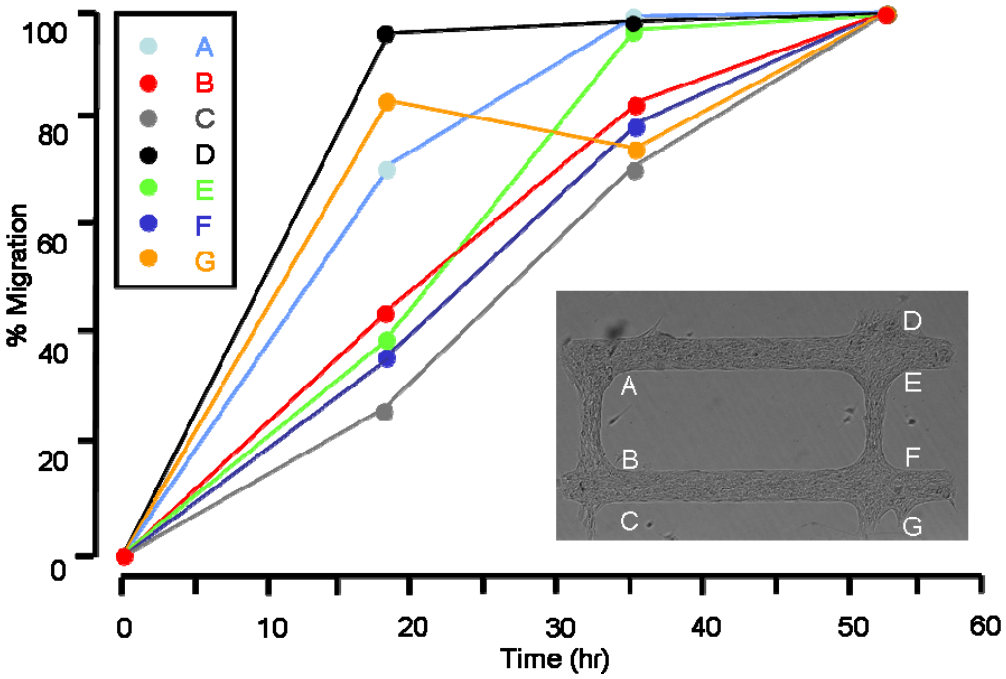

Figure 3-12. A plot showing migration over time in each zone A-G from Figure 3-11. The migration was set to 100 % where the two cell fronts migrating from both microcontact printed regions merged at the gradient pattern and the % migration was determined relatively. For the cells migrating toward the edge of the photo-pattern, reaching at the edge was considered as 100 % migration. The cells in high density of RGD zone moving down the gradient tend to migrate faster (A and E). The migration of the cells moving up the gradient of RGD is rather slow but steady (B and F).

moved only 35 % of the total distance in 20 hours. The RGD density is low in zone G and the cells migrate toward an even lower density of RGD. In the early stage the cells seemed to migrate quickly but the cell front was tracked back and overall migration was slow. The cells in zones B and F are migrated towards a higher density of RGD and the overall migration was gradual. The cells in zone B migrate a bit faster than the ones in zone F and it may be because of the slope difference in the ligand gradient. The zone C is in the similar condition to G and the cells were observed to migrate at a low rate probably due to the small numbers of RGD molecules. Overall the cells tend to migrate faster when they move down the gradient rather than up the gradient. Also the cells on the gradient with a steep slope were observed to respond faster than the cells on the mild gradient in both directions, either up or down the gradient. Therefore microscopy compatible gradient surface allows illustrating cell migration in the response to change in the ligand density.

In summary, we have created a photo-patterned gradient surface in which electroactive quinone monolayers became available for ligand coupling by photo-deprotection of the NVOC group. With this photo-patterning methodology, ligand immobilization onto the SAM surface is as quantitative and effective as hydroquinone/quinone monolayer. Combined with microcontact printing, the gradient of adhesive ligand was presented dynamically in the presence of the cells. As demonstrated in the migration study, this gradient surface is ideal for studying concentration-dependent cellular responses. Owing to the flexibility of ligand immobilizing method the substrate is applicable to tissue patterning and developmental modeling.

Application of Microcontact Printing and Photo-patterning for Ligand Mediated Co-cultures

For the co-culture of different cell types, two patterns were separately created on a substrate using chemical methods. The first pattern was generated by microcontact printing (Figure 3-13) and mixed SAMs of tetra(ethylene glycol)-terminated alkanethiols (99 %) and NVOC-protected hydroquinone-terminated alkanethiols (1 %) were prepared. The removal of NVOC groups upon UV illumination patterned the hydroquinone groups on the surface. Fibronectin was adsorbed onto the microcontact printed region to enhance the attachment of the first cell type. Electrochemical activation of hydroquinone groups and the following addition of oxyamine-functionalized RGD installed the adhesive peptide onto the photo-patterned area *via* oxime linkage to the quinones. When the second cell type was added, the cells adhered only to the photo-patterned RGD region as integrin receptors recognized the RGD ligand. In the same manner any biomolecule tethered with an oxyamine group can be coupled to the quinones by forming oxime adduct therefore this type of substrate has potential to be used for various ligand-receptor interactions. The oxime is chemically stable but the previous study showed that electrochemical reduction of the monolayer in pH 7 buffer solution can break the oxime and release the surface-bound ligand as a hydroxyl group, resulting the hydroquinone monolayer being recovered (Figure 3-14) [44]. When a reductive potential was applied onto the co-culture substrate, the cell type that attached to the RGD ligand was released.

The photo-patterning method provides an important feature in that ligand molecules can be installed onto the surface in gradient. By the use of photo-mask with gradient design ligand gradient with various slopes can be generated and it can stimulate cellular response such as migration within the pattern. Photo-pattering with gradient design highlights the

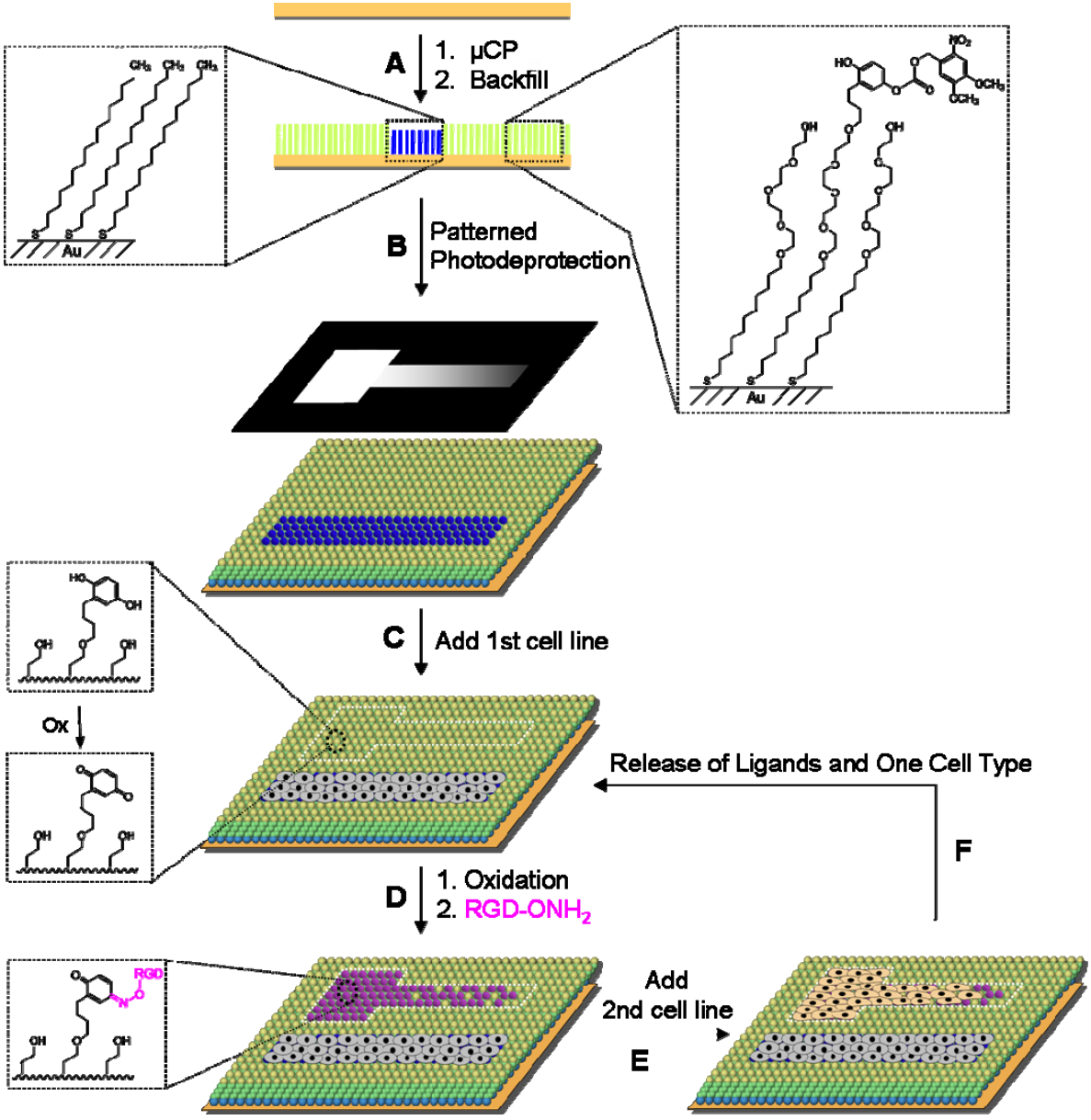
A
1. μCP
2. Backfill
B
Patterned
Photodeprotection
C
Add 1st cell line
Ox
D
1. Oxidation
2. RGD-ONH2
E
Add
2nd cell line
F
Release of Ligands and One Cell Type
RGD
Au

Figure 3-13**.** Schematic overview of substrate preparation for co-culture. A glass coverslip was coated with Ti (3 nm) and then gold (12 nm) by an electron-beam deposition method. A. To generate patterned surfaces, hexadecanethiols were microcontact printed onto the gold surface and the remaining bare gold regions were backfilled with a mixture of NVOC-hydroquinone and tetra(ethylene glycol) alkanethiols (1:99 ratio). B. The substrate was illuminated with UV light through a patterned microfiche mask, which resulted in the selective deprotection of NVOC groups to reveal the electroactive hydroquinone. C. An adhesive protein, fibronectin, was added to the substrate and only adsorbed to the hydrophobic microcontact printed pattern. Cells were seeded onto the entire substrate but exclusively adhered to the fibronectin patterned regions. D. The patterned hydroquinone groups were then converted to the reactive quinone groups by application of a mild oxidative electrochemical potential. Addition of soluble RGD-ONH_2 led to the installation of the adhesive peptide to the patterned quinone region via a stable covalent oxime linkage. E. Addition of a second cell line generated patterned co-cultures with exquisite spatial control. F. By application of a mild reductive electrochemical potential the oxime linkage is broken and the RGD peptides are released which in turn causes one population of cells to release from the surface. This strategy allows for the analysis of both cell types where their interactions are controlled spatially and temporally on a surface.

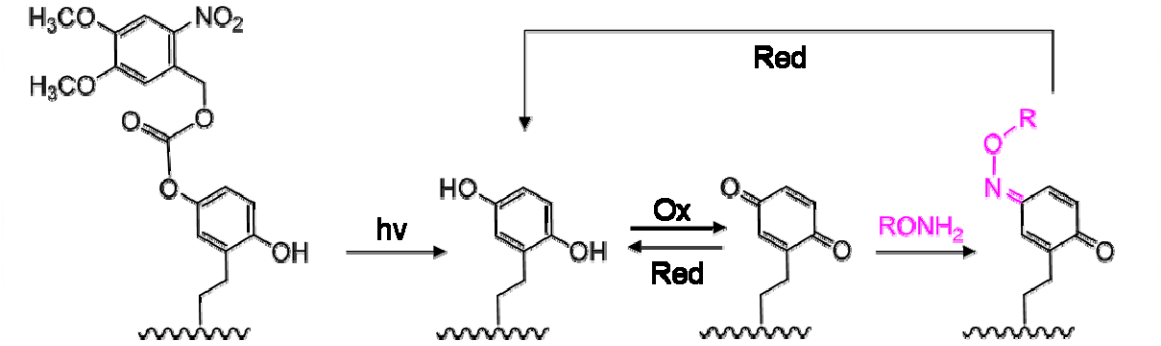

Figure 3-14. Application of a mild reductive potential to the oxime at the physiological pH releases surface-bound ligand and regenerates hydroquinone alkanethiolates.

delicate interaction between ligand and receptors. The characterization of gradient surface generated by photo-patterning is shown in Figure 3-15. In order to visualize the gradient pattern with fluorescence microscopy, rhodamine was immobilized through an oxime linkage. The rhodamine gradient slope gained from the imaging software was in accord with the gradient slope of the photo-mask. When RGD peptide was immobilized in the gradient pattern, cells attached up to certain density of ligand on the surface. In Figure 3-15A, cell adhesion diminished significantly when the ligand density reduced to 16 % on the gradient, where 100 % is the maximum density of RGD prepared on a surface of hydroquinone and tetra(ethylene glycol) (1:99 ratio). The minimal density of ligand for cell adhesion is dependent of gradient slope. Also cell migration can be induced by the immobilized adhesive ligands depending on ligand type, density and affinity. Hence this co-culture system has the potential to model cellular microenvironment where not only cell-cell contacts but also ligand effects in cell-cell interactions can be studied.

Figure 3-16A shows micrographs of the co-culture of two different cell lines. The microcontact printed area (rectangular shape) was patterned with cell lines transformed with GFP-actin therefore they were seen by both optical and fluorescence microscopy. The photo-patterned RGD region was attached by regular mouse fibroblast and they were only seen by brightfield imaging. Application of the reductive potential onto this surface discharged the oxime linkage. The release of the RGD ligand from the surface resulted in that the photo-patterned region did not support cell adhesion any longer and therefore the cells in the pattern were released as well (Figure 3-16B). The cell-cell contact can be spatially controlled by varying pattern size, geometry and distance of two patterns by use of a printing stamp and photo-mask. By deciding when to activate the surface with a specific ligand the substrate can

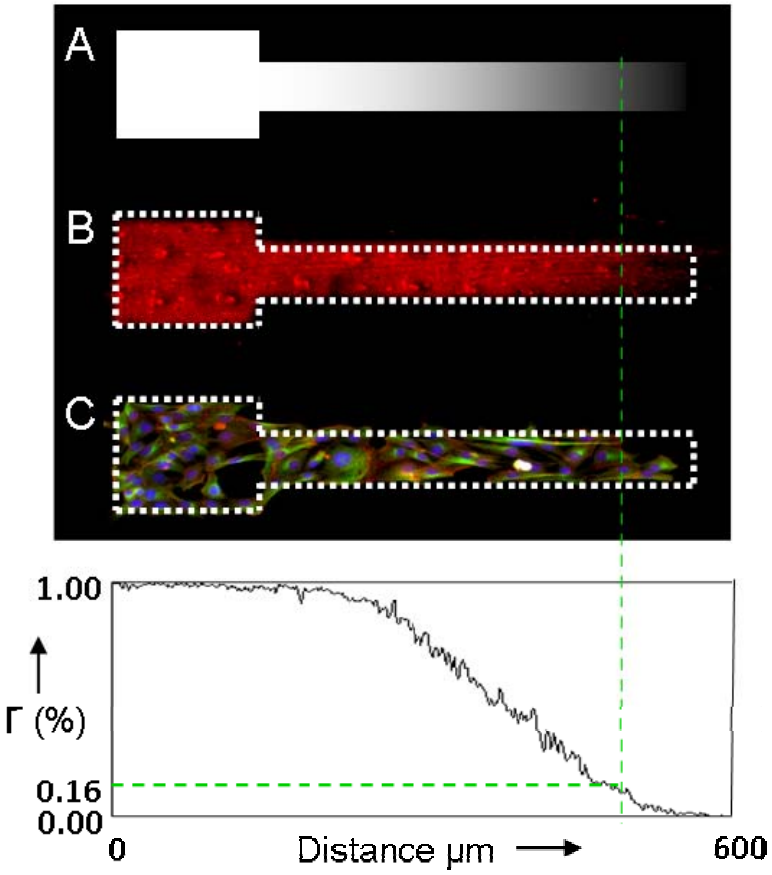

Figure 3-15. Characterization of the ligand gradient. Ligand gradient generated by photo-patterning affects cell adhesion. Using a mask with gradient pattern effectively produces gradient surface of hydroquinones thus creates ligand gradient on the surface. Imaging software (ImageJ) generated the gradient slope from the fluorescence image as shown at the bottom. By comparing the cell image with the slope profile of the ligand gradient, the required ligand density for cell adhesion can be traced. In this figure cell adhesion was greatly diminished when the ligand density was reduced to 16 % from the "saturated" ligand density.

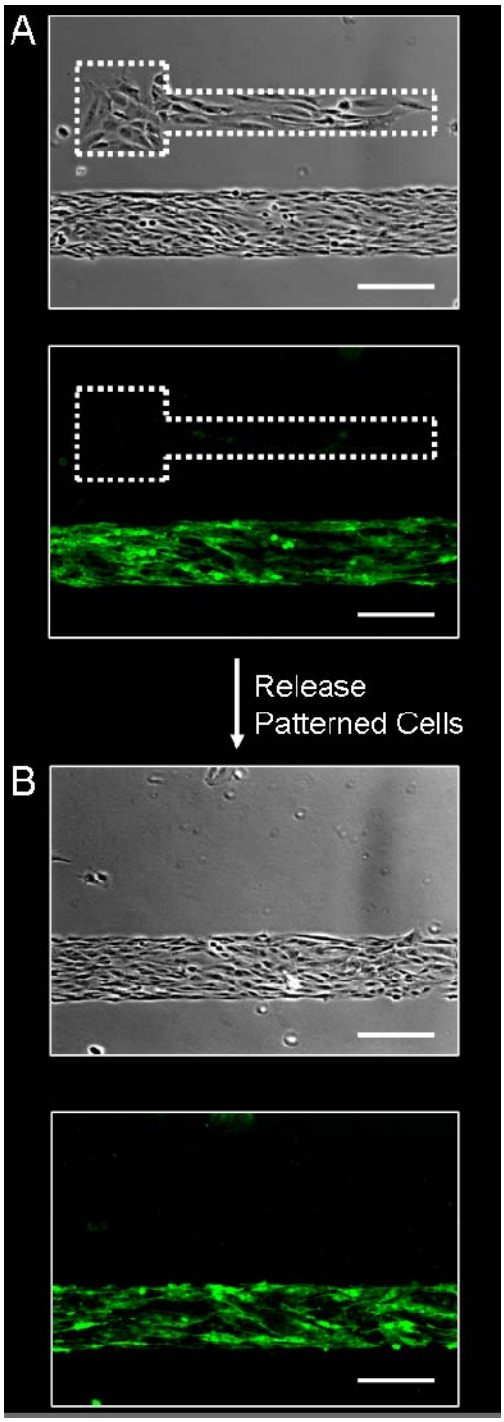

Figure 3-16. The co-culture of two different cell lines. The microcontact printed region was patterned with GFP-actin transformed cell line and the photo-patterned RGD area with regular fibroblast. The views under the optical brightfield microscopy and the fluorescence microscopy prove the combined method of microcontact printing and photo-patterning is effective to prepare a substrate for co-culture purpose. The photo-patterned RGD was released by applying reductive potential, as the result, the fibroblast cells detached from the pattern. (Scale bar: 100 μm)

be also temporally controlled. Furthermore how the ligand gradient affect cellular behavior and cell-cell communication can be studied with this co-culture system.

In summary, we generated a functional co-culture substrate by combining the strategy of microcontact printing and photo-patterning. This co-culture model substrate is spatiotemporally controlled and adds complexity of microenvironment by applying biological ligands in gradient onto the surface. The co-culture patterning strategy with ligand immobilization can be applied in the studies of nerve regeneration or tissue engineering for treatment purpose.

Materials and Methods

All the solvents for the synthesis were HPLC grade. THF was distilled from sodium benzophenone under nitrogen before use. Absolute ethanol was purchased from Aaper Alcohol Chemical Company. Flash chromatography was carried out using silica gel (230–400 mesh). All amino acids and resin were purchased from Anaspec, Inc. (La Jolla, CA). All other chemical reagents were purchased from Sigma Aldrich and Acros and used as received. FAK+/+ and FAK–/– mouse embryonic fibroblasts (MEF) were purchased from American Type Culture Collection (Manassas,VA).

*Di-tetrahydropyran-hydroquinone-hexylbromide (**3a**)*

To a solution of **1h** (3.0 g, 10.78 mmol) in dry THF (50 mL) at -75 °C was added *t*-butyllithium solution in pentane (1.7 M, 11.8 mL, 20 mmol) dropwise under atmosphere of nitrogen. The mixture was stirred for 40 minutes at 0 °C and brought to RT and stirred for an additional 30 minutes. To this solution excess 1, 6- dibromohexane (4.88 g, 20 mmol) in

THF was slowly added and the mixture was stirred at RT for 12 hours under atmosphere of nitrogen. Using rotary evaporation THF was removed and the reaction mixture was extracted in ethylacetate. After washing with NH_4Cl, water and brine, the crude product was dried over Na_2SO_4. The resulted clear oil was purified by column chromatography with hexane/ethyl acetate (8/1) to afford a white solid (1.9 g, 40 % yield). ^{1}H NMR (400 MHz, $CDCl_3$) δ 1.38-2.05 (m, 20 H), 2.62 (t, 2 H, J = 7.6 Hz), 3.47 (t, 2 H, J = 6.8 Hz), 3.50-3.57 (m, 2 H), 3.81-3.89 (m, 2 H), 5.30 (m, 2 H), 6.79-6.85 (m, 2 H), 6.99-7.0 (m, 1 H).

*Di-tetrahydropyran-hydroquinone-tetra(ethylene glycol)alkane-trityl (**3b**)*

The solution of **1j** (1.4 g, 2.25 mmol) in DMF (8 mL) was chilled to 0 °C and NaH (144 mg, 6 mmol) was added slowly. The reaction mixture was stirred at 0 °C for 1 hour and then stirred at RT for 2 hours. To this solution **3a** (0.6 g, 1.36 mmol) dissolved in dry THF (5 mL) was added dropwise. The reaction mixture was stirred at RT for 12 hours. By rotary evaporation THF and DMF was removed and the mixture was diluted with 20 mL ethyl acetate. The reaction mixture was washed with saturated NH_4Cl and brine, and dried over Na_2SO_4. The resulted yellow oil was purified by column chromatography with hexane/ethyl acetate (1/1) to give the product (0.6 g, 44.8 % yield) ^{1}H NMR (300 MHz, $CDCl_3$) δ 1.16-1.39 (m, 20 H), 1.49-1.68 (m, 14 H), 1.75-1.85 (m, 4 H), 2.14 (t, 2 H, J = 7.2 Hz), 2.60 (t, 2 H, J = 7.6 Hz), 3.38-3.43 (m, 4 H), 3.47-3.56 (m, 18 H), 3.79-3.89 (m, 2 H), 5.30 (m, 2 H), 6.77-6.85 (m, 2 H), 7.0 (d, 1 H), 7.19-7.25 (m, 3 H), 7.28-7.33 (m, 6 H), 7.39-7.42 (m, 6 H).

*Hydroquinone-tetra(ethylene glycol) alkane-trityl (**3c**)*

The product **3b** (0.6 g, 0.61 mmol) was taken up in 30 mL of a 3:1:1 mixture of acetic acid/water/THF and stirred at RT for 16 hours. The reaction mixture was concentrated under

high vacuum condition and dissolved in ethyl acetate. The solution was washed with water three times and brine, and dried over Na_2SO_4. The crude product was directly used for next reaction as ^{1}H NMR indicated only minor impurities (0.3 g, 61.3 % yield) ^{1}H NMR (400 MHz, $CDCl_3$) δ 1.14-1.40 (m, 18 H), 1.52-1.66 (m, 8 H), 2.11 (t, 2 H, J = 7.3 Hz), 2.54 (t, 2 H, J = 7.5 Hz), 3.40-3.44 (m, 4 H), 3.53-3.64 (m, 16 H), 6.50-6.53 (m, 1 H), 6.59-6.63 (m, 2 H), 7.16-7.20 (m, 3 H), 7.24-7.28 (m, 6 H), 7.38-7.40 (d, 6 H, J = 7.4 Hz).

*6-Nitroveratryloxycarbonyl hydroquinone-tetra(ethylene glycol) alkane-trityl (**3d**)*

To a solution of **3c** (0.3 g, 0.368 mmol) in anhydrous methylene chloride (20 mL) was added 4-(dimethylamino)pyridine (67.43 mg, 0.552 mmol) and 4, 5-dimethoxy-2-nitrobenzyl chloroformate (also called 6-nitroveratryloxycarbonyl chloride or NVOC-Cl) (111.6 mg, 0.405 mmol). The reaction mixture was stirred at RT for 12 hours under nitrogen. The resulted clear orange solution was diluted with 20 mL of methylene chloride, then washed with 1 M HCl (0.38 mL), water and brine. The organic layer was dried and concentrated to yellow oil. The column chromatography with hexane/ethyl acetate (2/8) gave the product (0.2 g, 51.5 % yield). ^{1}H NMR (400 MHz, $CDCl_3$) δ 1.19-1.38 (m, 18 H), 1.47-1.62 (m, 8 H), 2.14 (t, 2 H, J = 7.3 Hz), 2.61 (t, 2 H, 7.7 Hz), 3.38-3.42 (m, 4 H), 3.48-3.56 (m, 16 H), 3.95 (s, 3 H), 3.97 (s, 3 H), 5.60 (s, 2 H), 6.82-6.89 (m, 2 H), 6.96 (d, 1 H), 7.20-7.24 (m, 4 H), 7.29-7.33 (m, 6 H), 7.39-7.41 (m, 6 H), 7.75 (s, 1 H).

*6-Nitroveratryloxycarbonyl hydroquinone-tetra(ethylene glycol) alkanethiol (**3e**)*

Methylene chloride (30 mL) containing 5 % trifluoroacetic acid was added with 205 μL of tri-isopropylsilane (1 mmol). This solution was added to **3d** (0.2 g, 0.19 mmol) and stirred at RT for 12 hours under nitrogen. The reaction mixture was concentrated to yellow oil and

the purification by column chromatography (hexane/ethyl acetate (5/1) to hexane/ethyl acetate (1/2)) afforded the product as clear oil (0.1 g, 64.8 % yield). ^{1}H NMR (400 MHz, $CDCl_3$) δ 1.28-1.38 (m, 18 H), 1.48-1.68 (m, 8 H), 2.48 (t, 1 H, J = 7.4 Hz), 2.61 (t, 2 H, J = 7.7 Hz), 2.70 (t, 1 H, J = 7.3 Hz), 3.38-3.42 (m, 4 H), 3.49-3.56 (m, 16 H), 3.96 (s, 3 H), 3.98 (s, 3 H), 5.63 (s, 2 H), 6.82-6.89 (m, 2 H), 6.97 (d, 1 H), 7.23 (s, 1 H), 7.75 (s, 1 H).

Microscopy of Surface Immobilized Rhodamine

Scotch tape (3M) was adhered to the monolayer. The resulting substrate was then cured at 85 ºC for 20 minutes. The tape was peeled from the substrate, resulting in transfer of the monolayer from the gold substrate to the tape.

Microscopy of Attached Cell Culture

Adherent cells were fixed in 3.7 % paraformaldehyde in phosphate buffer saline (PBS) for 10 minutes and then permeabilized with 0.1 % Triton X in PBS (PBST) for 10 minutes. Cells were then stained with anti-tubulin (1:1000) in PBS containing 10 % goat serum for 1 hour, followed by Alexa 488-conjugated goat anti-mouse IgG (1:100 in PBST), phalloidin-tetramethylrhodamine B isothiocyanate (1:50 in PBST), and DAPI (1:300 in PBST) for 1 hour. Substrates were rinsed with deionized water before mounted onto glass cover slips for microscopy. For single cell polarity studies on surface gradients, a combination of fluorescent dyes were used to visualize the fibroblasts: DAPI (4', 6-diamidino-2-phenylindole dihydrochloride for the nucleus, Sigma, St. Louis, MO), phalloidin-tetramethylrhodamine B isothiocyanate (Sigma, St. Louis, MO) for F-actin cytoskeleton, anti-giantin (Covance Research Products, Berkeley, CA) with a fluorescent tagged secondary antibody (fluorescein conjugated goat anti-rabbit IgG, Jackson ImmunoResearch

Laboratories, Inc., West Grove, PA) targeting the Golgi apparatus, and mouse monoclonal anti-gamma tubulin (Sigma) to track centrosome position. All optical and fluorescent micrographs were imaged using a Nikon inverted microscope (model TE2000–E). All images were captured and processed by MetaMorph.

Fabrication of Photo-masks

The photopatterns were designed and drawn in PowerPoint. The patterns were then reduced 25 times and printed onto microfiches.

Photochemical Deprotection of Substrates

A substrate presenting NVOC protected hydroquinone and tetra(ethylene glycol) groups (2:8) was illuminated with ultraviolet light (100W Hg lamp, Nikon) filtered through a band-pass filter (365 nm) for 30 minutes to ensure complete deprotection of the NVOC groups. A substrate presenting NVOC protected hydroquinone and tetra(ethylene glycol) groups (1:99) was illuminated with ultraviolet light for 10 minutes.

Photopatterning of Peptide Ligands

UV illumination of a substrate presenting NVOC protected hydroquinone and tetra(ethylene glycol) groups (1:99) through a photo-mask for 10 minutes removed the NVOC groups. The substrate was then oxidized electrochemically at 750 mV for 10 seconds to convert the hydroquinone to the quinone. A RGD-oxyamine solution (20 mM in PBS) was added to the substrate for 4 hours to ensure complete immobilization of the peptide ligands. The substrate was then cleaned with water and dried before using for cell culture.

Cell Culture

Swiss 3T3 fibroblasts, FAK+/+ and FAK–/– MEF were cultured in Dulbecco's Modified Eagle Medium (Gibco) supplemented with 10 % calf bovine serum and penicillin/streptomycin. Cells were removed with a solution of 0.05 % trypsin/ 0.53 mM EDTA, resuspended in serum-free culture medium (10,000 cells/mL), and plated onto the SAM substrates. After 2 hours, the substrates were placed in serum containing media and maintained at 37 °C in a humidified 5 % CO_2 atmosphere.

Cell Patterning with Microcontact Printing

Hexadecanethiols (1 mM in ethanol) were printed on the gold-coated substrates using poly(dimethylsiloxane) stamp. The substrates were immersed in a 1 mM mixed ethanol solution of NVOC protected hydroquinone tetra(ethylene glycol) alkanethiol and tetra(ethylene glycol) alkanethiol for 12 hours. Photo-deprotection of NVOC group by illuminating UV light through photo-mask was followed by cell seeding onto the SAM substrates. The 3T3-Swiss albino cells in serum-free medium were added in a concentration of 10^5 cells/mL and incubated at 37 °C and 5 % CO_2. After 3 hours, the serum-free medium was replaced with serum-containing medium and incubated at the same condition.

Time-lapse Microscopy

Time-lapse images were recorded by at 10 minute intervals for 51 hours. The images were combined using MetaMorph software to create a movie file.

Photopatterning of Peptide Ligands for Co-culture

After removing NVOC groups by UV illumination, the first cell line was seeded onto the microcontact printed surface. The substrate was then oxidized electrochemically at 750

mV for 10 seconds to convert the hydroquinone to the quinone. An RGD oxyamine solution (10 mM in serum-free medium) was added to the substrate for 1 hour for immobilization of the peptide ligands. The substrate was then cleaned with serum-free medium. The addition of the second cell line was followed.

REFERENCES

1. Hubbell, J.A., *Bioactive biomaterials.* Curr. Opin. Biotechnol., 1999. **10**: p. 123-129.

2. Langer, R. and D.A. Tirrell, *Designing materials for biology and medicine.* Nature, 2004. **428**: p. 487-492.

3. Khetani, S.R. and S.N. Bhatia, *Engineering tissues for in vitro applications.* Curr. Opin. Biotechnol., 2006. **17**: p. 524-531.

4. Mrksich, M., *A surface chemistry approach to studying cell adhesion.* Chem. Soc. Rev., 2000. **29**: p. 267-273.

5. Yousaf, M.N., B.T. Houseman, and M. Mrksich, *Turning on cell migration with electroactive substrates.* Angew. Chem. Int. Ed., 2001. **40**: p. 1093-1096.

6. Chan, E.W.L. and M.N. Yousaf, *Surface chemistry control to silence gene expression in Drosophila Schneider 2 cells through RNA interference.* Angew. Chem. Int. Ed., 2007. **46**: p. 3881-3884.

7. Hoover, D.K., et al., *Electroactive nanoarrays for biospecific ligand mediated studies of cell adhesion.* ChemBioChem, 2007. **8**: p. 1920-1923.

8. Hannon, B.M. and M. Ruth, *Modeling dynamic biological systems*, ed. M. Ruth and B.M. Hannon. 1997, New York: **Springer**.

9. Yousaf, M.N. and M. Mrksich, *Dynamic substrates: modulating the behaviors of attached cells.* In new technologies for life sciences: a trends guide, 2002: p. 28-35.

10. Ashe, H.L. and J. Briscoe, *The interpretation of morphogen gradients.* Development, 2006. **133**: p. 385-394.

11. Tabata, T. and Y. Takei, *Morphogens, their identificatin and regulation.* Development, 2004. **131**: p. 703-712.

12. Early, A., T. Abe, and J. Williams, *Evidence for positional differentiaion of prestalk cells and for a mophogenetic gradient in Dictyostelium.* Cell, 1995. **83**(91-99).

13. Bar-Shavit, R., et al., *Monocyte Chemotaxis: stimulation by specific exosite region in thrombin.* Science, 1983. **220**: p. 728-731.

14. Rosoff, W.J., et al., *A new chemotaxis assay shows the extreme sensitivity of axons to molecular gradients.* Nature Neurosci., 2004. **7**: p. 678-682.

15. Song, H.-j. and M.-m. Poo, *Signal transduction underlying growth cone guidance by diffusible factors.* Curr. Opin. Neurobiol., 1999. **9**: p. 355-363.

16. Mueller, B.K., *Growth cone guidance: first steps towards a deeper understanding.* Annu. Rev. Neurosci., 1999. **22**: p. 351-388.

17. Devreotes, P. and C. Janetopoulos, *Eukaryotic chemotaxis: distinctions between directional sensing and polarization.* J. Biol. Chem, 2003. **278**: p. 20445-20448.

18. Ridley, A.J., et al., *Cell migration: integrating signals from front to back.* Science, 2003. **302**: p. 1704-1709.

19. Lauffenburger, D.A. and A.F. Horwitz, *Cell migration: a physically integrated molecular process.* Cell, 1996. **84**: p. 359-369.

20. Rhoads, D.S. and J.-L. Guan, *Analysis of directional cell migration on defined FN gradients: role of intracellular signalin molecules.* Exp. Cell Res., 2007. **313**: p. 3859-3867.

21. Nelson, P.R., S. Yamamura, and K.C. Kent, *Extracellular matrix proteins are potent agonists of human smooth muscle cell migration.* J. Vasc. Surg, 1996. **24**(1): p. 25-33.

22. Aznavoorian, S., et al., *Signal transduction for chemotaxis and haptotaxis by matrix molecules in tumor cells.* J. Cell Biol., 1990. **110**: p. 1427-1438.

23. Jeon, N.L., et al., *Generation of solution and surface gradients using microfluidic systems.* Langmuir, 2000. **16**: p. 8311-8316.

24. Nakanishi, J., et al., *Spatiotemporal control of cell adhesion on a self-assembled monolayer having a photocleavable protecting group.* Anal. Chim. Acta, 2006. **578**: p. 100-104.

25. Nakanishi, J., et al., *Spatiotemporal control of migration of single cells on a photoactivatable cell microarray.* J. Am. Chem. Soc., 2007. **129**: p. 6694-6695.

26. Keenan, T.M. and A. Folch, *Biomolecular gradients in cell culture systems.* Lab Chip, 2008. **8**: p. 34-57.

27. Heit, B., et al., *An intracellular signaling hierarchy determines direction of migration in opposing chemotactic gradients.* J. Cell Biol., 2002. **159**(1): p. 91-102.

28. Chen, H., et al., *Semaphorin neuropilin interactions underlying sympathetic axon responses to class III semaphorins.* Neuron, 1998. **21**(6): p. 1283-1290.

29. Gundersen, R.W. and J.N. Barrett, *Neuronal chemotaxis: chick dorsal-root axons trun toward hight concentrations of nerve growth factor.* Science, 1979. **206**: p. 1079-1080.

30. Boyden, S., *The chemotactic effect of mixtures of antibody and antigen on polymorphonuclear leucocytes.* J. Exp. Med., 1962. **115**: p. 453-466.

31. Flemming, R.G., et al., *Effects of synthetic micro- and nano-structured surfaces on cell behavior.* Biomaterials, 1999. **20**(6): p. 573-588.

32. Folch, A. and M. Toner, *Microengineering of cellular interactions.* Annu. Rev. Biomed. Eng., 2000. **2**(1): p. 227-256.

33. El-Ali, J., P.K. Sorger, and K.F. Jensen, *Cells on chips.* Nature, 2006. **442**(7101): p. 403-411.

34. Tsai, I.Y., M. Kimura, and T.P. Russel, *Fabrication of gradient heterogenous surface using homopolymers and diblock polymers.* Langmuir, 2004. **20**: p. 5952-5957.

35. Hersel, U., C. Dahmen, and H. Kessler, *RGD modified polymers: biomaterials for stimulated cell adhesion and beyond.* Biomaterials, 2003. **24**: p. 4385-4415.

36. Gunawan, R.C., et al., *Cell Migration and polarity on microfabricated gradients of extracellular matrix proteins.* Langmuir, 2006. **22**: p. 4250-4258.

37. Dertinger, S.K.W., et al., *Gradients of substrate bound laminin orient axonal specification of neurons.* Proc. Natl. Acad. Sci. U.S.A., 2002. **99**: p. 12542-12547.

38. Harris, B.P., et al., *Photopatterned polymer brushes promoting cell adhesion gradients.* Langmuir, 2006. **22**: p. 4467-4471.

39. Herbert, C.B., et al., *Micropatterning gradients and controlling surface densities of photoactivatable biomolecules on self-assembled monolayers of oligo(ethylene glycol) alkanethiolates.* Chem. Biol., 1997. **4**: p. 731-737.

40. Mayer, M., et al., *Micropatterned agarose gels for stamping arrays of proteins and gradients of proteins.* Proteomics, 2004. **4**: p. 2366-2376.

41. Wang, Q. and P.W. Bohn, *Surface composition gradients of immobilized cell signaling molecules. Epidermal growth factor on gold.* Thin Solid Films, 2006. **513**: p. 338-346.

42. Plummer, S.T., et al., *Electrochemically derived gradients of the extracellular matrix protein fibronectin on gold.* Langmuir, 2003. **19**: p. 7528-7536.

43. Chan, E.W.L. and M. Yousaf, *A photo-electroactive surface strategy for immobilizing ligands in patterns and gradients for studies of cell polarization.* Mol. BioSyst., 2008. **4**: p. 746-753.

44. Chan, E.W.L., S. Park, and M.N. Yousaf, *An electroactive catalytic dynamic substrate that immobilizes and releases patterned ligands, proteins and cells.* Angew. Chem. Int. Ed., 2008. **47**: p. 6267-6271.

45. Chan, E.W.L. and M.N. Yousaf, *Immobilization of ligands with precise control of density to electroactive surfaces.* J. Am. Chem. Soc., 2006. **128**: p. 15542-15546.

46. Clark, E.A. and J.S. Brugge, *Integrins and signal transduction pathways: the road taken.* Science, 1995. **268**: p. 233-239.

47. Davies, P.F., *Biology of disease: vascular cell interactions with special reference to the pathogenesis of atherosclerosis.* Lab. Invest., 1986. **55**: p. 5-24.

48. van Breemen, C., et al., *Endothelium-smooth muscle intractions in blood vessels.* Clin. Exp. Pharmacol. Physiol., 1997. **24**: p. 989-992.

49. Camps, J.L., et al., *Fibroblast-mediated acceleration of human epithelial tumor growth in vivo.* Proc. Natl. Acad. Sci. USA, 1990. **87**: p. 75-79.

50. Chen, C.S., J. Tan, and J. Tien, *Mechanotransduction at cell-matrix and cell-cell contacts.* Annu. Rev. Biomed. Eng., 2004. **6**: p. 275-302.

51. Bhatia, S.N., et al., *Effect of cell-cell interactions in preservation of cellular phenotye: cocultivation of hepatocytes and nonparenchymal cells.* FASEB J., 1999. **13**: p. 1883-1900.

52. Zhou, H., et al., *Osteoblasts directly control lineage commitment of mesenchymal progenitor cells through Wnt Signaling.* J. Biol. Chem., 2008. **283**: p. 1936-1945.

53. Aufderheide, E., R. Chiquet-Ehrismann, and P. Ekblom, *Epithelial-messenchymal interactions in the developin gkidney lead to expression of terascin in the mesenchyme.* J. Cell Biol., 1987. **105**: p. 599-608.

54. Tsuda, Y., et al., *The use of patterned dual thermoresponsive surfaces for the collective recovery as co-cultured cell sheets.* Biomaterials, 2005. **26**: p. 1885-1893.

55. Yamamoto, M., et al., *Novel patterned cell co-culture utilising thermally responsive grafted polymer surfaces.* J. Biomed. Mater. Res., 2001. **55**: p. 137-140.

56. Khademhosseini, A., et al., *Co-culture of human embryonic stem cells with murine embryonic fibroblasts on microwell-patterned substrates.* Biomaterials, 2006. **27**: p. 5968-5977.

57. Bhatia, S.N., M.L. Yarmush, and M. Toner, *Controlling cell interactions by micropatterning in co-cultures: Hepatocytes and 3T3 fibroblasts.* J. Biomed. Mater. Res., 1997. **34**: p. 189-199.

58. Folch, A. and M. Toner, *Microengineering of cellular interactions.* Annu. Rev. Biomed. Eng., 2000. **2**: p. 227-256.

59. Jukuda, J., et al., *Micropatterned cell co-cultures using layer-by-layer deposition of extracellular matrix components.* Biomaterials, 2006. **27**: p. 1479-1486.

60. Fan, H., et al., *Enhanced differentiation of mesenchymal stem cells co-cultured with ligament fibroblasts on geletin/silk fibroin hybrid scaffold.* Biomaterials, 2008. **29**: p. 1017-1027.

61. Waldeck, D.H., A.P. Alivisatos, and C.B. Harris, *Nonradiative damping of molecular electronic excited-states by metal surfaces.* Surf. Sci., 1985. **158**: p. 103-125.

62. Schlaepfer, D.D. and C.R. Hauck, *Signaling through focal adhesion kinase.* Prog. Biophys. Mol. Biol., 1999. **71**: p. 435-478.

63. Wang, H.-B., et al., *Focal adhesion kinase is involved in mechanosensing during fibroblast migration.* Proc. Natl. Acad. Sci. U.S.A., 2001. **98**: p. 11295-11300.

64. Sastry, S.K. and K. Burridge, *Focal adhesions: A nexus for intracellular signaling and cytoskeletal dynamics.* Exp. Cell Res., 2000. **261**: p. 25-36.

65. Nelson, W.J., *Adaptation of core mechanisms to generate cell polarity.* Nature, 2003. **422**: p. 766-774.

66. Théry, M., et al., *Anisotropy of cell adhesive microenvironment governs cell internal organization and orientation of polarity.* Proc. Natl. Acad. Sci. U.S.A., 2006. **103**: p. 19771-19776.

67. Linstedt, A.D. and H.P. Hauri, *Giantin, a novel conserved Golgi membrane protein containing a cytoplasmic domain of at least 350 kDa.* Mol. Biol. Cell, 1993. **4**: p. 679-693.

CHAPTER 4

The Use of a Model Substrate for Cell Adhesion in Dip-pen Nanolithography and Total Internal Reflection Fluorescence Microscopy

Introduction

Dip-pen Nanolithography for Cell Biology

Lithographic methods are widely used in microfabrication, nanotechnology and molecular electronics. Dip-pen nanolithography (DPN) is based on a scanning-probe technique in which an atomic force microscopy (AFM) tip is used to pattern molecules onto a surface with precise nanometer-scale features (Figure 4-1) [1]. Unlike many other lithographic methods, DPN transports small amount of molecules to a substrate in a positive printing mode and it does not rely on a resist, stamp, or complicated processing methods. DPN technique is widely used in fabrication of nanostructures and nanoarrays of DNA and proteins [2-5]

In biology it is challenging to study subcellular nanoarchitecture structure because there are not many tools available. For example, integrin receptors on the cell surface regulate affinity against adhesive ligands and the nature of interaction between ligand and integrins determines whole cell body's behavior. In particular, the number and size of biospecific interactions between extracellular ligands and integrins can be critical for cell adhesion and cell migration. However, we do not quite understand such physical features due to the lack of

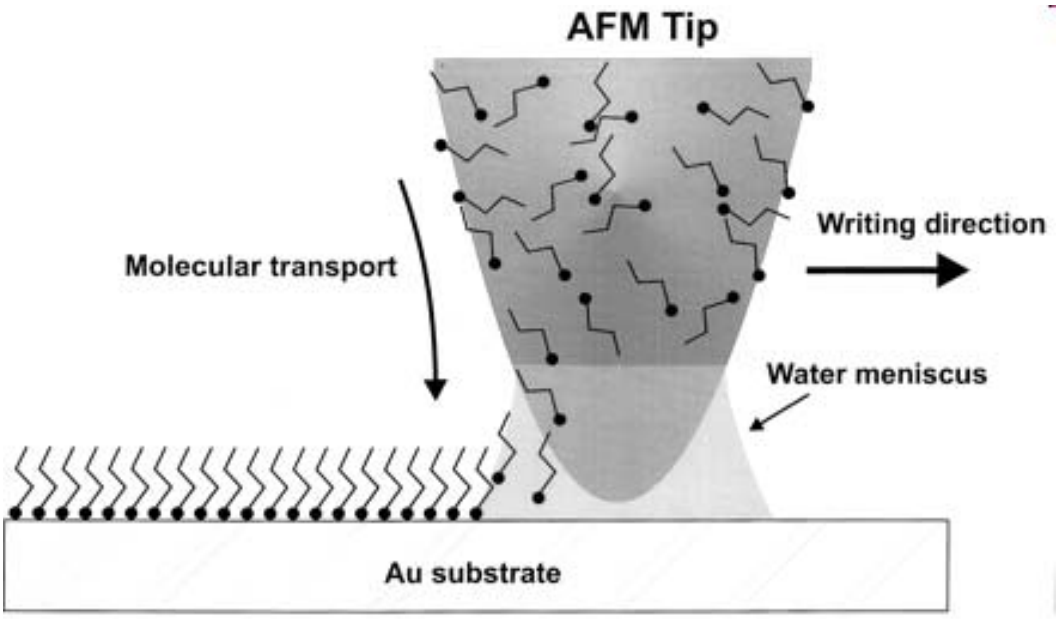

Figure 4-1. Schematic representation of DPN. The figure was taken from reference 1.

molecularly defined nanopatterned model substrates. The protein nanoarrays created by nonspecific adsorption of protein to nanometer-sized patterns do not offer precise control over the orientation and spatial distribution of the immobilized ligand [6, 7]

A model substrate which can present nanometer size ligand molecules with precise control of spatial distribution will be useful to understand the nanoarchitecture of adherent cells. Combining the ligand immobilization method on quinone monolayers with DPN, a chemoselective peptide-immobilized electroactive nanoarray was generated and its use in cell-adhesion studies will be discussed [8].

Total Internal Reflection Fluorescence Microscopy

A number of molecular events in cellular surfaces such as cell adhesion and membrane dynamics have been studied with conventional fluorescence microscopes [9, 10]. However, fluorophores that are bound to the specimen surface and those in the surrounding medium exist in an equilibrium state. When the fluorophores are excited and there is a much larger population of non-bound molecules in the medium, the resulting fluorescence from the fluorophores bound to the specimen surface would be overwhelmed by the background fluorescence. Total internal reflection fluorescence microscopy (TIRFM) was developed to solve this problem [11]. TIRFM employs the phenomenon of total internal reflection, which occurs at the interface between an optically dense medium, such as glass, and an optically less dense medium –water or aqueous solution. At a large angle of incidence, the excitation beam reflects back into the glass and generates at the interface with water so called evanescent wave. The evanescent wave is generated only when the incident light is totally reflected at the glass-water interface. The evanescent electromagnetic field decays

exponentially from the interface, and thus penetrates to a depth of only approximately 100 nm into the sample medium. Thus the TIRFM enables a selective visualization of surface regions such as the basal plasma membrane of cells [12-14]. TIRF efficiently rejects background signal from the bulk of solution and allows for super sensitive detection - down to single molecules. TIRF is real-time, low volume (< 0.1 μL), *in situ* technique which is well-suited for analysis of biomolecular interactions such as protein-protein, receptor-ligand, protein-DNA, DNA-DNA, and protein-membrane interactions [10, 15-19].

TIRFM has been used to study a variety of systems, including single molecule fluorescence [20] as well as events and structures at the cell surface such as exocytosis [21, 22], and ion channels [23]. It has also been integrated with other methods such as interference reflection microscopy [24] and fluorescence correlation spectroscopy [25].

Due to the flexibility of surface chemistry and conductivity, gold has been widely used for biointerfacial studies and as a platform for many biotechnologies. However, due to gold's efficient quenching of fluorescence, limited optical transparency, and lack of long-term stability due to monolayer desorption, it has not found wide use in practical biosensor applications. Until recently, it was thought that gold surfaces precluded the use of live-cell high resolution fluorescence microscopy to study internal cell structure dynamics. However the combination of fluorescence microscopy (a fundamental tool in cell biology research) and gold surfaces as model substrates in cell biology allows for the development of sophisticated immobilization strategies to install a variety of biologically relevant ligands on the surface.

The use of TIRFM to study cell adhesion on patterned self-assembled monolayers (SAMs) on gold surfaces will be discussed. Microcontact printing was used to pattern hydrophobic features to which the extracellular protein fibronectin was adsorbed, while DPN

was used to produce electroactive nanoarrays of hydroquinone-terminated alkanethiol on gold-coated quartz substrates [26]. The hydroquinone was electrochemically oxidized to the corresponding quinone, and an oxyamine-tethered linear Arg-Gly-Asp (RGD) peptide was chemoselectively immobilized. A prism-based method of TIRFM was used to examine adhered cells on both microscale and nanoscale features. TIRFM can be used to visualize internal features of a cell on chemoselectively tailored gold SAM surfaces and open many areas for integrating TIRFM with material science and cell signaling dynamics to study cell behavior.

Results and Discussion

Electroactive Nanoarrays for Biospecific Ligand Mediated Studies of Cell Adhesion

Hydroquinone-terminated alkanethiol was patterned by DPN in nanometer-sized spots on a gold substrate (Figure 4-2). The remaining bare gold region was then backfilled with tetra(ethylene glycol)-terminated alkanethiol. Application of an oxidative electrochemical potential converts the hydroquinone to the corresponding reactive quinone on the surface. The resulting quinone monolayer then undergoes a chemoselective coupling reaction with the soluble oxyamine-tethered peptide.

This nanoarray is molecularly well-defined as immobilized ligands on the monolayer which are uniformly presented in a homogeneous environment. The use of tetra(ethylene glycol)-terminated alkanethiol ensures that cell adhesion is due only to biospecific interactions between immobilized ligands and cell receptors. The density of ligand on the surface can be precisely determined owing to the electroactive nature of both the original monolayer and the resultant immobilized ligand. The use of electrochemistry allows

measuring the extent of the reaction and thus the amount of immobilized ligand on the surface. Furthermore, if the oxyamine group is introduced, any molecule can be coupled to the monolayer surface and therefore these electroactive nanoarrays can be applied for a variety of cell biological studies and biosensing applications.

Silicon AFM tips were first immersed in a 5 mM solution of hydroquinone-terminated alkanethiol in acetonitrile for 40 seconds and then dried. The AFM tip was subsequently used to print the hydroquinone alkanethiol on a gold-coated glass substrate in 500 nm spots. A 20 × 20 nanoarray with dimensions of 65 × 65 μm was generated by using nanolithography software. Figure 4-3 shows a lateral force microscopy (LFM) image of the hydroquinone-terminated alkanethiol nanoarray before backfilling the remaining bare gold region of the substrate with tetra(ethylene glycol)-terminated alkanethiol. The LFM profile shows that each spot in the array has similar features in terms of spot size and lateral force.

The hydroquinone groups presented in the nanoarrays were converted to the corresponding quinone by applying an oxidative potential (750 mV vs. Ag/AgCl, 15 seconds in 1 M $HClO_4$). An oxyamine-functionalized linear Arg-Gly-Asp (RGD) peptide was then immobilized to the quinone nanoarray (10 mM in phosphate-buffered saline (PBS), 5 hours). Cyclic voltammetry showed the monolayer presenting hydroquinone groups underwent a reversible oxidation at 580 mV and reduction at -30 mV in 1 M perchloric acid. Addition of soluble oxyamine-RGD resulted in new peaks corresponding to the oxidation (520 mV) and reduction (180 mV) of the oxime product (Figure 4-4). By integrating the peaks in the cyclic voltammogram and controlling the number and size of the DPN spots, we can calculate the approximate density of initial hydroquinone/quinone and the immobilized oxime conjugate ligands per spot. For 500 nm spots, we determined the number of molecules to be

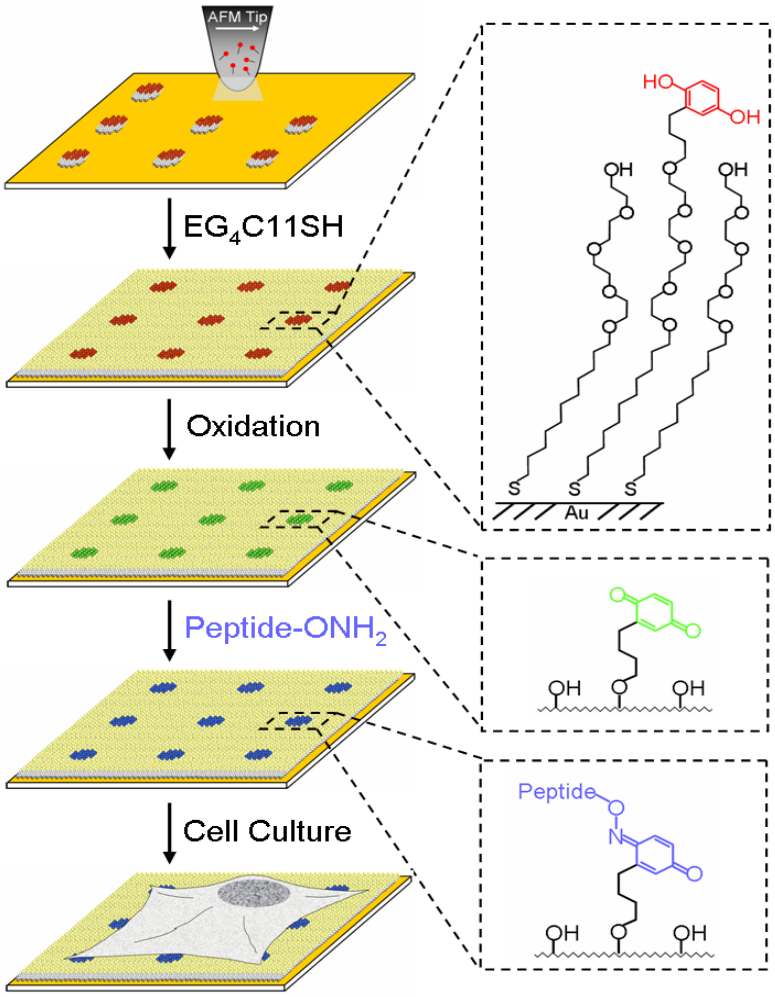

Figure 4-2. A schematic diagram for the preparation of electroactive nanoarrays by DPN. An AFM tip coated with hydroquinone terminated alkanethiol patterned the gold surface with nanometer-sized spots. The remaining bare gold region was backfilled with tetra(ethylene glycol) terminated alkanethiol. The electroactive nanoarrays were electrochemically oxidized to convert the hydroquinone groups to the corresponding quinone. An oxyamine terminated peptide was selectively immobilized onto the quinone monolayer *via* an oxime conjugate to promote cell adhesion on the electroactive nanoarray.

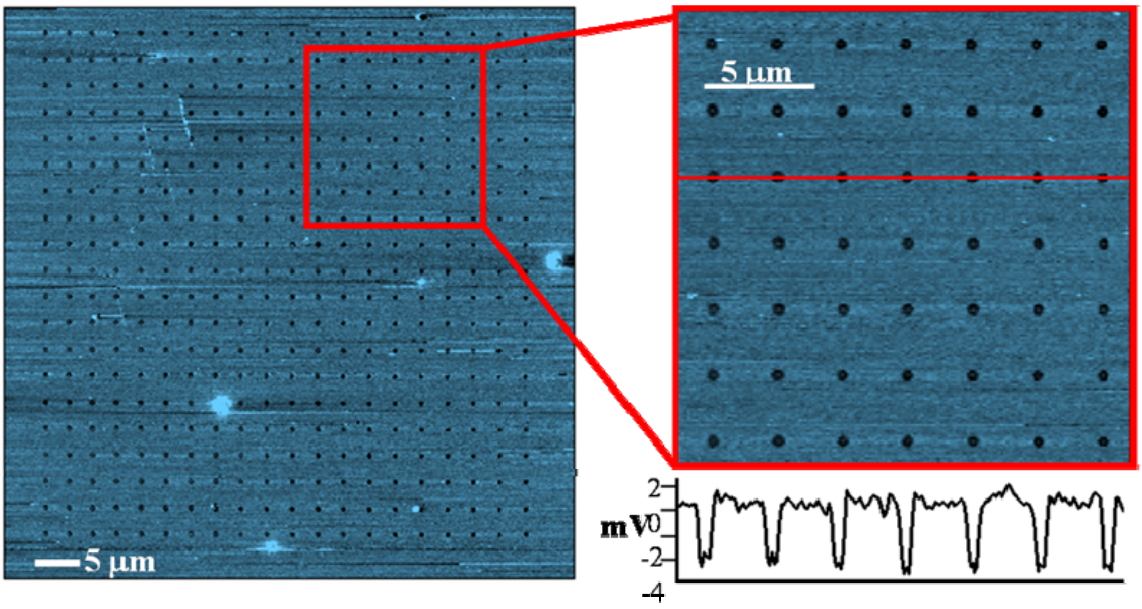

Figure 4-3. Lateral force microscopy (LFM) image of an electroactive nanoarray. The array was generated by DPN of hydroquinone terminated alkanethiol on gold. The array consists of 400 spots (20 × 20) with an average spot size of 500 nm in diameter. Also a lateral force profile for the line drawn across the image is shown.

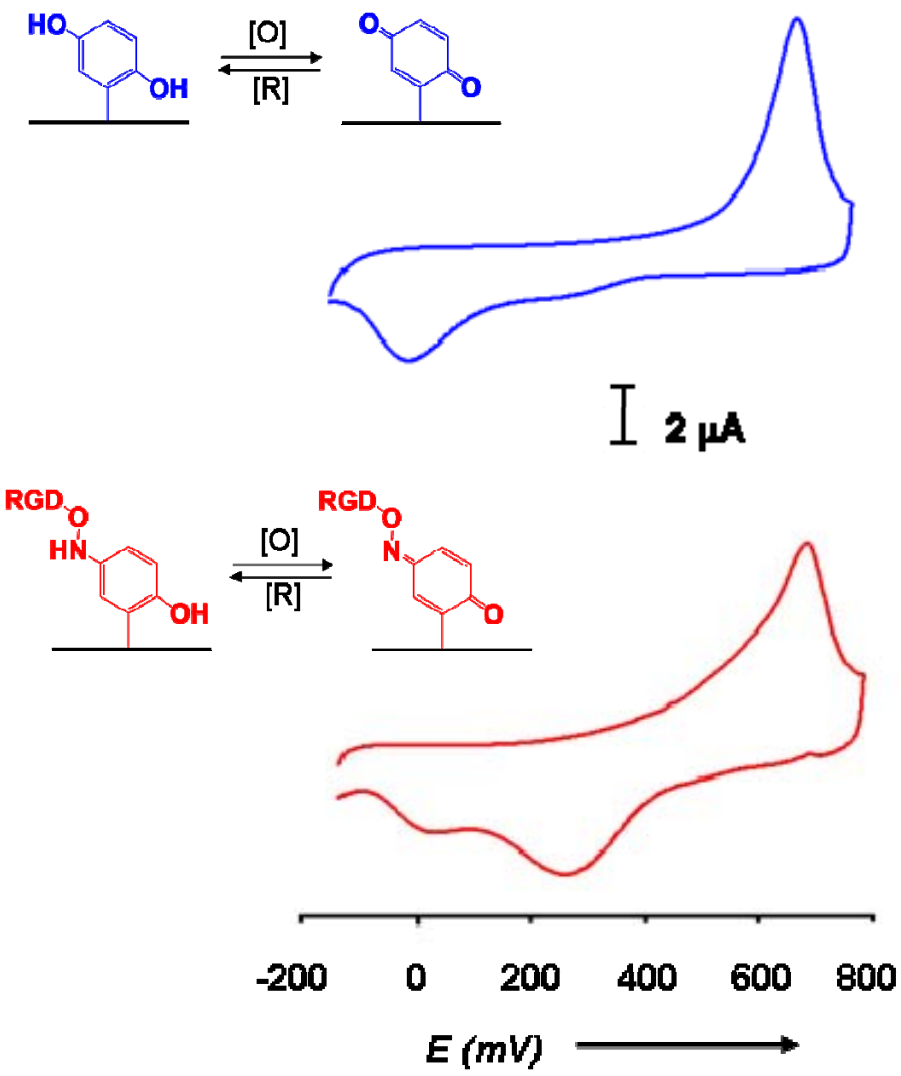

Figure 4-4. Cyclic voltammograms of the redox active reactant and product. The diagnostic oxidation and reduction peaks to characterize the extent of ligand immobilization on the electroactive nanoarray.

approximately 1.1×10^5 for hydroquinone/quinone; this is similar to full monolayer coverage for that size spot. By integrating the redox peaks for the oxime conjugate product after oxidation and ligand immobilization, we found the reaction to only proceed to approximately 85 % completion as characterized by cyclic voltammetry. This is probably due to the difficulty of reacting every quinone on a densely packed spot region. Therefore, this results in approximately 0.9×10^5 molecules per 500 nm spot of ligand-oxime conjugate on the nanoarray. By monitoring electrochemistry to regulate the duration of the reaction of the peptide-oxyamine with the quinone form of the surface it is possible to adjust the density of the peptide ligand on each spot. This is not possible with other nanoarray immobilization strategies. This exquisite control would prove critical in determining how ligand clustering influences cell adhesion and focal complex formation.

For the cell-adhesion studies on the electroactive nanoarrays, we immobilized two different forms of the RGD peptide to induce specific adhesion. The assembly and morphology of focal adhesions are critical in signal transduction during ligand-mediated cell-adhesion polarization and migration. The focal adhesion structures of adhered cells on the electroactive nanoarrays were analyzed by visualization with an anti-paxillin antibody. Paxillin is a protein found within focal adhesions as discussed in Chapter 2 [27].

In order to study the effect of ligand affinity on focal adhesion structures of adherent cells, we immobilized a linear and a cyclic RGD oxyamine (10 mM in PBS, 5 hours). The affinity of integrin receptors for cyclic RGD is known to be much stronger than that for linear RGD (K_d of 10^{-9} M versus 10^{-6} M, respectively). The difference in the binding affinity between the two peptides has been shown to result in dramatically different focal-adhesion patterns in adherent cells on model surfaces [28, 29]. Figure 4-5 shows a fluorescence

micrograph of 3T3 Swiss Albino fibroblasts on a 65 × 65 μm nanoarray composed of 500 nm diameter spots spaced 3 μm apart. The micrographs show a cell adhered to a cyclic RGD nanoarray that is identical in dimensions and numbers of spots to a linear RGD nanoarray. The adherent cell adapts a rectangular morphology, thus indicating that the cell is confined by the peptide nanoarray.

Interestingly, for the linear RGD nanoarrays, the focal adhesions stained by anti-paxillin antibodies are located primarily at the periphery of the cell. Image analysis of many single cells (n = 22) on the nanoarray shows the focal adhesions are approximately 6 μm in diameter and that there are higher concentrations at the edge of the cell. This suggests that the cells are in a more motile state on lower-affinity linear RGD peptides.

For the cyclic-RGD nanoarray we observed many more focal adhesions, and they are distributed throughout the cell body. Further analysis shows the focal adhesions are approximately 2 μm in diameter and that there are approximately 8 times the number of focal adhesions on the cyclic RGD nanoarray than on the linear one. As a control, a scrambled oxyamine-RDG peptide was immobilized to the nanoarray; no cells adhered to the surface. With the addition of soluble linear RGD peptide (50 μM, 30 minutes) cells adhered to the immobilized linear and cyclic RGD nanoarrays were detached, thus indicating the cells were attached biospecifically and only through the immobilized peptides. The addition of a fibroblast with focal adhesion kinase knockout cell line (FAK -/- cells) that is compromised in its ability to make focal adhesions on both the linear and cyclic nanoarray did not support attachment; this further showed the specificity of immobilized peptide and cell-surface integrin receptors required for biospecific adhesion. We also observed on nanoarrayed surfaces of linear and cyclic RGD peptides that the size of the focal adhesions are

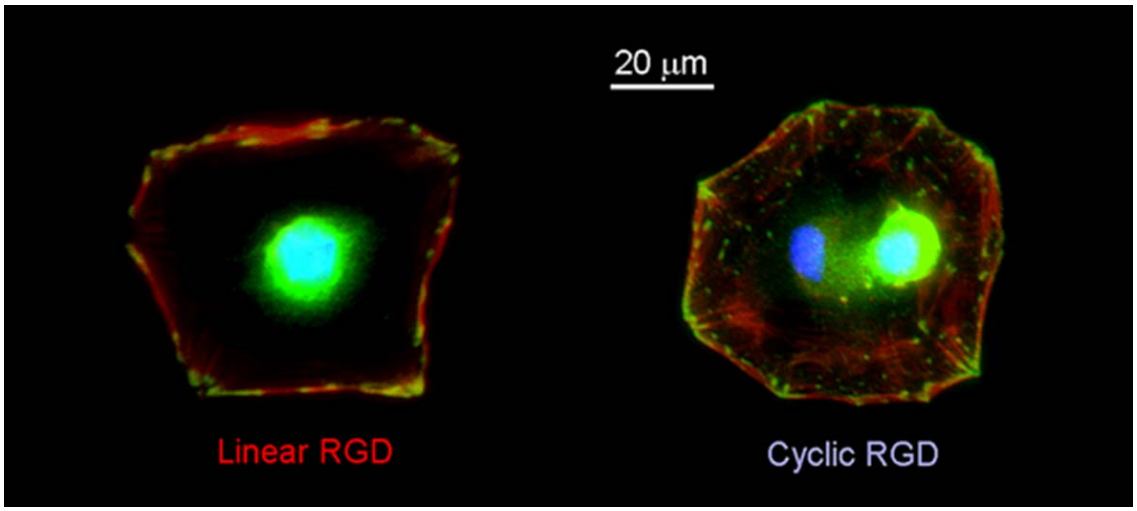

Figure 4-5. Representative fluorescent micrographs of cells on linear and cyclic RGD nanoarrays. Comparison of the focal adhesions (green dots) shows that the cell attached to linear RGD has focal adhesions distributed at the perimeter, while the cell adhered to cyclic RGD has focal adhesions distributed throughout the cell. Color: green, paxillin; red, actin; blue, nuclei.

approximately 2 - 6 μm and appear in the classical needle-like structures; this is consistent with focal adhesion size and structure determined for many different cell lines on fibronectin-coated substrates. Taken together, the nature of the ligand immobilized nanoarray directly influences the number and size of focal adhesions.

To determine the influence of spot size and separation and ligand affinity on cell adhesion, we next generated differently sized nanoarrays. We observed that a nanoarray of 500 nm spots with double the distance between spots (6 μm apart instead of 3 μm) did not support cell attachment on either ligand. Interestingly, nanopatterned surfaces with 200 nm spots spaced 3 μm apart supported cell attachment for cyclic RGD but not for linear RGD. This result shows lower ligand density is required for the higher-affinity cyclic RGD to support cell adhesion. This might support the role of ECM ligand clustering on modulating the adhesion and migration behavior of cells.

The overall dramatic differences in the distribution and size of focal adhesions between the linear and cyclic RGD nanoarrays suggest that the underlying nature of the ligands on the nanoarrays can influence the nanoarchitecture of adherent cells. Further careful investigation is required to precisely determine the subtle interplay between nanoarray spot size, ligand affinity and spacing for determining cell adhesion and migration.

In conclusion, we have demonstrated the use of DPN to generate an electroactive nanoarray that can immobilize a variety of peptide ligands for biospecific ligand-mediated cell adhesion. We have shown that the nanoarray and subsequent ligand immobilization can be characterized by electrochemistry. We have further shown that the affinity of immobilized ligands for integrin receptors can dramatically affect the focal adhesion structures of the adherent cells. The use of the immobilization strategy based on the chemoselective reaction

between quinone and oxyamine, coupled with the inert surface provides a general route for the preparation of nanoarray substrates presenting a variety of ligands.

TIRFM of Cell Adhesion on Patterned SAMs on Gold

A prism-based method of TIRFM was used to examine the cells adhered on patterned SAMs on gold-coated quartz surfaces. As shown in Figure 4-6, the prepared slide was placed in contact between a quartz prism and a 60 × water immersion objective, using immersion oil and water, respectively, to maintain a similar refractive index between each interface. TIR was established by adjusting the quartz prism, thus changing the angle of incidence (Θ) of a 532 nm green diode laser beam. The emitted fluorescence of fluorophores excited by the evanescent wave created was filtered and captured by a CCD camera.

Microcontact printing generated patterned SAMs of hexadecanethiol on gold-coated quartz (Figure 4-7A). To characterize the microcontact printed features scanning electron microscopy (SEM) was used as shown in Figure 4-7B. Following backfilling with tetra(ethylene glycol) alkanethiol (EG_4SH), the ECM protein fibronectin was adsorbed to the hydrophobic regions in order to support cell adhesion. 3T3 Swiss Albino mouse fibroblasts were allowed to adhere to the patterns, fixed, and stained with an antibody targeting paxillin followed by a fluorescently labeled secondary antibody. As can be seen in the TIRFM micrograph in Figure 4-7C, paxillin is distributed throughout the cells.

We produced electroactive nanoarrays on gold-coated quartz substrates by integrating the previously described chemoselective ligand immobilization strategy and DPN. An oxyamine-tethered ligand, linear RGD-ONH_2, was reacted following electrochemical activation of the nanopatterned surface (Figure 4-8). 3T3 Swiss Albino mouse fibroblasts

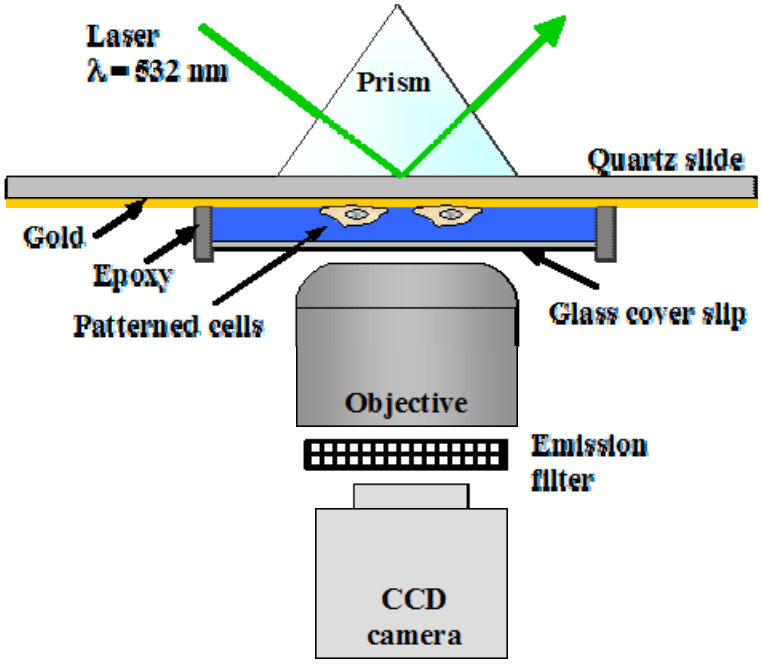

Figure 4-6. Schematic depiction of TIRFM experiment. The sample was placed between a water immersion 60 × objective and a quartz prism as shown (using water and immersion oil, respectively, for similar refractive indices). Fluorescence excited by TIR was collected through the objective, filtered, and captured on a CCD camera. (Complete optics path has been omitted for clarity.)

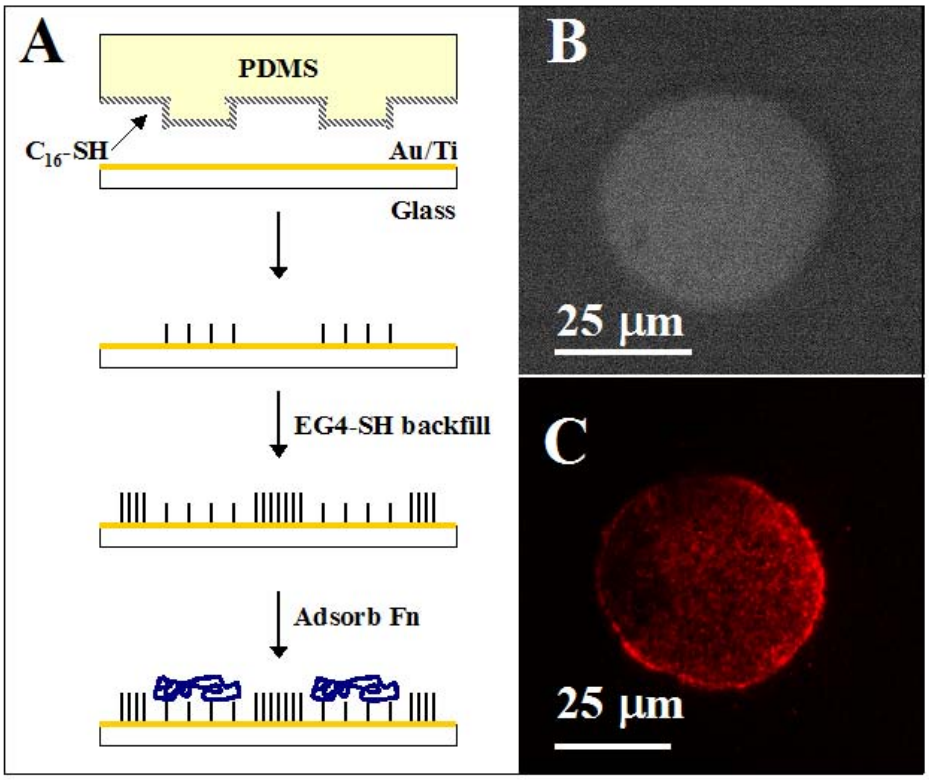

Figure 4-7. Patterning by microcontact printing. A. Microcontact printing was used to pattern 50 μm features of C_{16}-SH on gold substrates. The remaining bare gold regions were backfilled with EG_4-SH, and fibronectin (Fn) was adsorbed to the microcontact printed area. Cells were then seeded on the surfaces. B. SEM micrograph of microcontact printed monolayers of C_{16}-SH on gold. C. Representative micrograph of a fibroblast adhered to a 50 μm microcontact printed feature. The cells were stained with anti-paxillin antibodies and a TRITC secondary antibodies to visualize the focal adhesions in the cell. TIRFM signal from TRITC labeled secondary antibody is pseudocolored red.

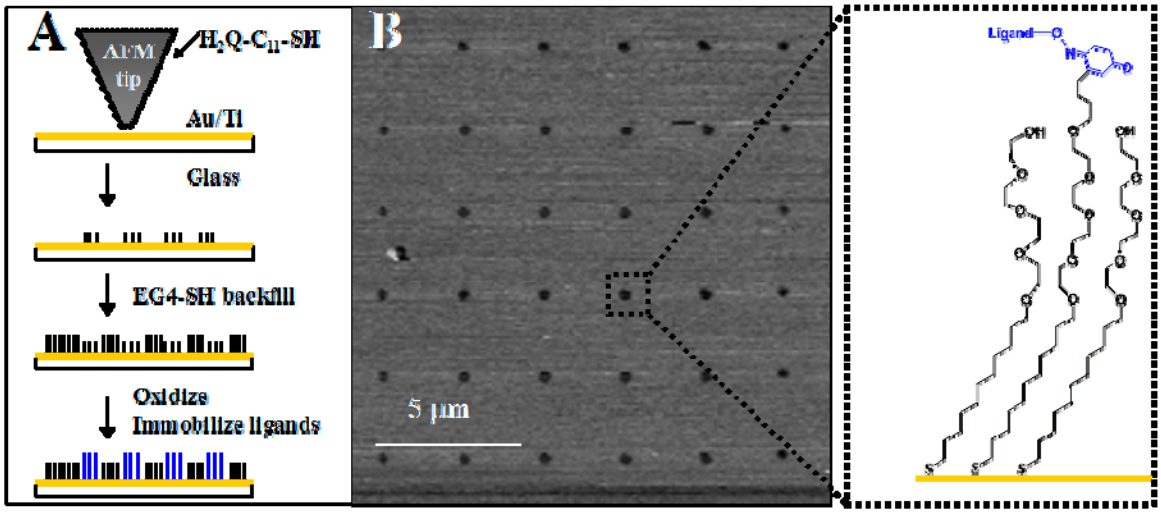

Figure 4-8. Preparation of electroactive nanoarray. A. DPN was used to produce electroactive nanoarrays of hydroquinone-terminated alkanethiol (H_2Q-C_{11}-SH). Following backfilling with EG_4-SH, the nanoarrays were electrochemically oxidized and an oxyamine-tethered ligand (linear RGD-ONH_2) was chemoselectively immobilized. B. Expanded lateral force microscopy image of an electroactive nanoarray on gold.

were then seeded to the substrates, fixed, and stained for nuclei, actin, and paxillin. As shown in Figure 4-9A, the paxillin-TRITC (tetramethylrhodamine B isothiocyanate) signal found in TIRFM is localized primarily to the perimeter of the cell. We then imaged the same substrates using conventional fluorescence microscopy. The representative fluorescent micrograph in Figure 4-9B was taken of a cell on a nanoarray of immobilized linear RGD using standard fluorescence microscopy following TIRFM imaging. Interestingly, there is not a significant amount of photobleaching of the TRITC secondary antibody following extended imaging using TIRFM.

In conclusion we have demonstrated that TIRFM can be used to visualize the internal structures of cells adhered to SAMs on gold surfaces. We have also shown that TIRFM imaging can be used in conjunction with more traditional methods of imaging, such as fluorescence microscopy, to study cells. Finally, we show the combination of TIRFM with surface patterning techniques (microcontact printing, DPN) and an electroactive immobilization strategy to tailor surfaces with ligands to study cell behavior.

In the future, TIRFM could be used to explore the intricacies of the cell nanoarchitecture on surfaces presenting various patterns of biospecific ligands. In particular, this technique could be used to study signaling dynamics in cell adhesion, polarization, and migration on well-defined surfaces presenting more complex surface chemistries such as gradients or by integration with patterned dynamic surfaces.

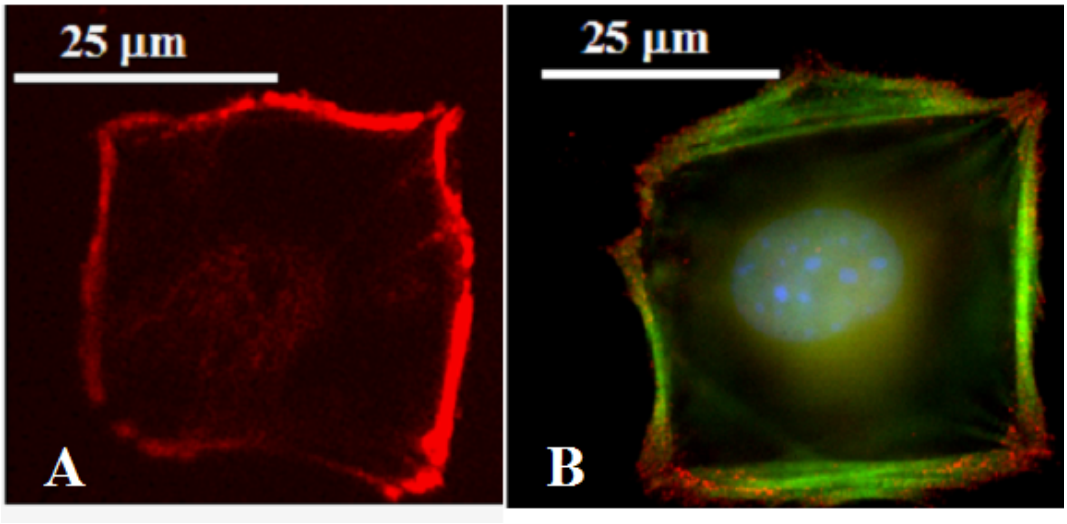

Figure 4-9. Images of a cell acquired by TIRFM. A. Representative TIRFM micrograph of a cell on a nanoarray. TIRFM signal from TRITC labeled secondary antibody is pseudocolored red. B. Representative micrograph of a 3T3 Swiss Albino fibroblast taken with fluorescence microscopy following imaging using TIRFM. Color: green, actin; red, paxillin; blue, nuclei.

Materials and Methods

Preparation of Electroactive Nanoarray Substrates

Glass cover slips were first cleaned with piranha solution (concentrated sulfuric acid/30 % H_2O_2 = 3/1, *v*/*v*). An adhesion layer of titanium (5 nm) and a transparent layer of gold (15 nm) were then thermally evaporated onto the surface. After preparation, the gold substrates were again cleaned with Piranha solution for approximately 1 minute, copiously rinsed with purified water (Millipore Direct-Q UV system, and either stored in water or dried with air and used directly. All DPN and LFM measurements were made with a MFP-3D Stand Alone atomic-force microscope (Asylum Research, Santa Barbara, CA). Silicon AFM tips (0.03-0.08 N m^{-1}, MikroMasch USA, Wilsonville, OR) were immersed in a solution of hydroquinone alkanethiol (H_2Q-C_{11}-SH, 5 mM in acetonitrile) for 40 seconds, then gently dried with a stream of air. Nanoarrays of dots approximately 500 nm in diameter were then produced by using Microangelo nanolithography software (Asylum Research). The nanoarrays were imaged directly following printing with the same tip at a scan rate of 4 Hz to produce the LFM image shown in Figure 4-3. The remaining exposed areas of gold were passivated by soaking the substrate in a solution of tetra(ethylene glycol) alkanethiol (EG_4-C_{11}-SH, 1 mM in ethanol) for 12 hours, followed by immersion in water for 1 hour.

Electrochemistry and Peptide Immobilization

All electrochemical measurements were conducted on a BAS 100B/W Electrochemical Analyzer (Bioanalytical Systems, Inc., West Lafayette, IN). All cyclic voltammograms were recorded at a scan rate of 50 mV/s in 1 M $HClO_4$ at room temperature. For cell-adhesion studies, the H_2Q-C_{11}-SH nanoarrays were first oxidized by applying a potential of 750 mV

(vs. Ag/AgCl) for 15 seconds in 1 M $HClO_4$. The resulting quinone was then treated with oxyamine-tethered peptide (10 mM in PBS) for 5 hours to install the peptide on the surface.

Cell Culture and Microscopy

3T3 Swiss Albino mouse fibroblasts were seeded on the patterned substrates, incubated overnight in Dulbecco's modified Eagle's medium (Sigma) with 10 % bovine calf serum and 1 % penicillin/streptomycin, and then fixed with 3.2 % formaldehyde in PBS. The cells were then permeated with PBS containing 0.1 % Triton X-100 and stained with three fluorescent dyes: DAPI (4', 6-diamidino-2-phenylindole dihydrochloride; Sigma), phalloidin-tetramethylrhodamine B isothiocyanate (Sigma), and anti-paxillin (BD Biosciences, San Jose, CA) with a secondary fluorescently labeled antibody (Cy-2 conjugated goat anti-mouse IgG, Jackson ImmunoResearch Laboratories, Inc., West Grove, PA). Fluorescence images were taken by using a Nikon Eclipse TE2000-E inverted microscope (Nikon USA, Inc., Melville, NY).

Substrate Patterning by Microcontact Printing

A gold-coated quartz slide was patterned by microcontact printing of hexadecanethiol ($C_{16}SH$, 1 mM in ethanol). The remaining bare gold region was then backfilled with tetra(ethylene glycol) alkanethiols. Bovine fibronectin (0.1 mg/mL in PBS, Fisher) was adsorbed onto the microcontact printed region for 1 hour.

Cell Visualization Using TIRF Microscopy and Fluorescence Microscopy

Following the cell staining procedure, patterned substrates were prepared for TIRFM analysis. A glass coverslip was flamed and placed over the area of patterned cells, trapping a layer of PBS between the glass and quartz. The edges of the coverslip were sealed using 90 s

curing epoxy (Araldite 2043, McMaster-Carr, Princeton, NJ). All TIRFM measurements were made using a prism-based method with an Olympus IX51 inverted microscope and Olympus UPLSAPO 60 × water immersion objective (NA = 1.2, Olympus America, Inc., Center Valley, PA), as shown in Figure 4-6. The excitation radiation was supplied by a green diode laser module (532 nm, 30 mW, GDLM-5030 L, Photop Technologies, Chatsworth, CA). The emitted radiation was sent through a green emission filter (585 nm/70 nm band pass, Chroma HQ585/70, Chroma Technology, Rockingham, VT) and captured by a CCD camera (Cascade II 512B, Photometrics, Tucson, AZ). Final image analysis was performed using MatLab R2007B (The Mathworks, Inc., Natick, MA). Fluorescence microscopy images were taken using an inverted Nikon Eclipse TE2000-E microscope (Nikon USA, Melville, NY).

REFERENCES

1. Piner, R.D., et al., *"Dip-Pen" Nanolithography.* Science, 1999. **283**(5402): p. 661-663.

2. Demers, L.M., et al., *Direct patterning of modified oligonucleotides on metals and insulators by dip-pen nanolithography.* Science, 2002. **296**(5574): p. 1836-1838.

3. Wilson, D.L., et al., *Surface organization and nanopatterning of collagen by dip-pen nanolithography.* Proc. Natl. Acad. Sci. U.S.A., 2001. **98**(24): p. 13660-13664.

4. Lee, K.-B., J.-H. Lim, and C.A. Mirkin, *Protein nanostructures formed via Direct-Write Dip-Pen nanolithography.* J. Am. Chem. Soc., 2003. **125**(19): p. 5588-5589.

5. Lee, S.W., et al., *Biologically active protein nanoarrays generated using parallel dip-pen nanolithography.* Adv. Mater., 2006. **18**(9): p. 1133-1136.

6. Lee, K.-B., et al., *Protein nanoarrays generated by dip-pen nanolithography.* Science, 2002. **295**(5560): p. 1702-1705.

7. Lehnert, D., et al., *Cell behaviour on micropatterned substrata: limits of extracellular matrix geometry for spreading and adhesion.* J. Cell Sci., 2004. **117**(1): p. 41-52.

8. Hoover, D.K., et al., *Electroactive nanoarrays for biospecific ligand mediated studies of cell adhesion.* ChemBioChem, 2007. **8**(16): p. 1920-1923.

9. Hodgson, L., et al., *Combining surface chemistry with a FRET-based biosensor to study the dynamics of RhoA GTPase activation in cells on patterned substrates.* J. Am. Chem. Soc., 2007. **129**(30): p. 9264-9265.

10. Navratil, M., G.A. Mabbott, and E.A. Arriaga, *Chemical microscopy applied to biological systems.* Anal. Chem., 2006. **78**(12): p. 4005-4020.

11. Axelrod, D., *Total internal reflection fluorescence microscopy in cell biology*, in *Methods Enzymol.* 2003, Academic Press. p. 1-33.

12. Steyer, J.A. and W. Almers, *A real-time view of life within 100 nm of the plasma membrane.* Nat. Rev. Mol. Cell Biol., 2001. **2**(4): p. 268-275.

13. Burmeister, J.S., et al., *Application of total internal reflection fluorescence microscopy to study cell adhesion to biomaterials.* Biomaterials, 1998. **19**(4-5): p. 307-325.

14. Groves, J.T., R. Parthasarathy, and M.B. Forstner, *Fluorescence imaging of membrane dynamics.* Annu. Rev. Biomed. Eng., 2008. **10**(1): p. 311.

15. Ravier, M.A., T. Tsuboi, and G.A. Rutter, *Imaging a target of Ca2+ signalling: dense core granule exocytosis viewed by total internal reflection fluorescence microscopy.* Methods, 2008. **46**(3): p. 233-238.

16. Kandere-Grzybowska, K., et al., *Molecular dynamics imaging in micropatterned living cells.* Nat. Meth., 2005. **2**(10): p. 739-741.

17. Kandere-Grzybowska, K., et al., *Cell motility on micropatterned treadmills and tracks.* Soft Matter, 2007. **3**(6): p. 672-679.

18. Chen, X.-W. and A.R. Saltiel, *TIRFing out studies on Glut4 trafficking.* Dev. Cell, 2007. **12**(1): p. 4-5.

19. Axelrod, D., *Cell-substrate contacts illuminated by total internal reflection fluorescence.* J. Cell Biol., 1981. **89**(1): p. 141-145.

20. Hanasaki, I., et al., *Single-molecule measurements and dynamical simulations of protein molecules near silicon substrates.* J. Phys. D: Appl. Phys., 2008. **41**: p. 95301-95309.

21. Zhang, Z., et al., *Regulated ATP release from astrocytes through lysosome exocytosis.* Nat. Cell Biol., 2007. **9**(8): p. 945-953.

22. Ohara-Imaizumi, M., et al., *Imaging analysis reveals mechanistic differences between first- and second-phase insulin exocytosis.* J. Cell Biol., 2007. **177**(4): p. 695-705.

23. Nechyporuk-Zloy, V., et al., *Dynamics of single potassium channel proteins in the plasma membrane of migrating cells.* Am. J. Physiol. Cell Physiol., 2008. **294**(4): p. C1096-1102.

24. Llobet, A., V. Beaumont, and L. Lagnado, *Real-time measurement of exocytosis and endocytosis using interference of light.* Neuron, 2003. **40**(6): p. 1075-1086.

25. Thompson, N.L. and B.L. Steele, *Total internal reflection with fluorescence correlation spectroscopy.* Nat. Protocols, 2007. **2**(4): p. 878-890.

26. Hoover, D.K., E.-J. Lee, and M.N. Yousaf, *Total internal reflection fluorescence microscopy of cell adhesion on patterned self-assembled monolayers on gold.* Langmuir, 2009. **25**(5): p. 2563-2566.

27. Turner, C.E., J.R. Glenney, and K. Burridge, *Paxillin: a new vinculin-binding protein present in focal adhesions.* J. Cell Biol., 1990. **111**: p. 1059-1068.

28. Kato, M. and M. Mrksich, *Using model substrates to study the dependence of focal adhesion formation on the affinity of integrin-ligand complexes.* Biochemistry, 2004. **43**(10): p. 2699-2707.

29. Massia, S.P. and J.A. Hubbell, *An RGD spacing of 440 nm is sufficient for integrin alpha V beta 3- mediated fibroblast spreading and 140 nm for focal contact and stress fiber formation.* J. Cell Biol., 1991. **114**(5): p. 1089-1100.